

NN 28701, 3/280

**MAGNETIC RESONANCE IMAGING OF PLANTS:
PLANT WATER STATUS AND DROUGHT STRESS RESPONSE**

LOUISE VAN DER WEERD-MEULENKAMP

Proefschrift

ter verkrijging van de graad van doctor
op gezag van de rector magnificus
van Wageningen Universiteit,
Prof. Dr. Ir. L. Speelman,
in het openbaar te verdedigen
op dinsdag 15 oktober 2002
des namiddags te 13.30 uur
in de aula van Wageningen Universiteit.

CENTRALE LANDBOUWCATALOGUS



0000 0913 6199

1002093

Promotor:

Prof. Dr. T.J. Schaafsma

emeritus hoogleraar in de biofysica

Wageningen Universiteit

Co-promotor:

Dr. H. Van As

universitair hoofddocent

Laboratorium voor Biofysica

Wageningen Universiteit

Promotiecommissie:

Prof. Dr. A.M.C. Emons, Laboratorium voor Plantencelbiologie, Wageningen Universiteit

Prof. Dr. A. Heerschap, Cluster Radiologie, Katholieke Universiteit Nijmegen

Dr. Ir. F.A. Hoekstra, Laboratorium voor Plantenfysiologie, Wageningen Universiteit

Prof. Dr. K. Nicolay, Sectie Biomedische NMR, Technische Universiteit Eindhoven

Prof. Dr. E. Steudle, Leerstoel Plantenecologie, Universiteit Bayreuth, Duitsland

**THE BEGINNING OF WISDOM IS: ACQUIRE WISDOM;
AND WITH ALL YOUR ACQUIRING, GET UNDERSTANDING.**

PROVERBS 4:7

The work presented in this thesis was performed at Wageningen University, Department of Agrotechnology and Food Science, Laboratory of Biophysics, The Netherlands.

Van der Weerd-Meulenkamp, Louise

Magnetic Resonance Imaging of Plants: Plant water status and drought stress response

Thesis, Wageningen University – Met een samenvatting in het Nederlands

ISBN: 90-5808-707-7

Subject headings:

compartment / data analysis / diffusion / exchange / membrane permeability / MRI / multi-exponential / NMR / relaxation / simulation / water transport

STELLINGEN

Het gebruik van absolute parameterwaarden voor het fitten van relaxatiecurves leidt bij lage signaal-ruis verhoudingen tot een te hoge waarde van de relaxatietijden en een verminderde contrastverhouding van de MRI-beelden.

Dit proefschrift, Hfdst 2.

De aanname dat de z.g.n. diffusion attenuation plot voor lange diffusietijden naar een basislijn nadert als gevolg van restrictie is in strijd met de gangbare diffusietheorieën.

W. Wycoff *et al.* (2000) The determination of the cell size in wood by nuclear magnetic resonance diffusion techniques. *Wood and Fiber Science* 32, 72-80. Dit proefschrift, Hfdst 4.

Het belangrijkste voordeel van niet-invasieve technieken, het verkrijgen van lineaire data voor hetzelfde object of individu, wordt grotendeels teniet gedaan als vervolgens alleen de gemiddelde waarden voor alle individuen worden gepresenteerd.

F.J. van Spronsen *et al.* (1993) Plasma phenylalanine and tyrosine responses to different nutritional conditions (fasting/prostprandial) in patients with phenylketonuria: effect of sample timing. *Pediatrics* 4, 570-573.

De hypothese dat cytoplasmatische stroming een belangrijke bijdrage levert aan de diffusiecoëfficiënt van water is op grond van de huidige kennis van de eigenschappen water in biologische systemen niet gerechtvaardigd.

D. Thomas *et al.* (2000) The measurement of diffusion and perfusion in biological systems using magnetic resonance imaging. *Physics in Medicine and Biology* 45, R97-R138.

Het goedkeuren van therapeutisch gebruik van foetale stamcellen op grond van de baten voor de patient is een typisch voorbeeld van 'het doel heiligt de middelen'.

R.M. Green. (2001) Four moral questions for human embryonic cell research. *Wound Repair and Regeneration* 9, 425-428.

Het bepalen van een arbeidsongeschiktheidspercentage van een persoon aan de hand van het verlies aan inkomen in een nieuwe passende functie betekent dat personen in een goedbetaalde functie vaker ziek geacht worden dan mensen met een laag salaris.

Stellingen behorend bij het proefschrift

Magnetic Resonance Imaging of Plants: Plant water status and drought stress response

Louise van der Weerd-Meulenkamp

Wageningen, 15 oktober 2002

CONTENTS

PREFACE	<i>vii</i>
1. INTRODUCTION	1
2. EVALUATION OF ALGORITHMS FOR THE ANALYSIS OF NMR RELAXATION DECAY CURVES	15
3. MODELLING OF SELF-DIFFUSION AND RELAXATION TIME NMR IN MULTI-COMPARTMENT SYSTEMS WITH CYLINDRICAL GEOMETRY	29
4. SIMULATION OF RELAXATION, DIFFUSION AND EXCHANGE IN MULTI-COMPARTMENT SYSTEMS	45
5. QUANTITATIVE NMR MICROSCOPY OF OSMOTIC STRESS RESPONSES IN MAIZE AND PEARL MILLET	65
6. NMR IMAGING OF MEMBRANE PERMEABILITY CHANGES IN PLANTS DURING OSMOTIC STRESS	83
7. NMR IMAGING OF THE WATER STATUS IN MAIZE AND PEARL MILLET DURING SEVERE OSMOTIC STRESS	101
8. GENERAL DISCUSSION	109
SUMMARY	115
SAMENVATTING	117
CURRICULUM VITAE	119
LIST OF PUBLICATIONS	120

VOORWOORD

Alleen mijn naam staat op de voorkant van dit proefschrift, maar zonder de hulp van collega's, vrienden en familie was dit boekje er nooit gekomen. Daarom wil ik graag een aantal mensen die een belangrijke bijdrage hebben geleverd bedanken. Henk, jij bent degene geweest die me kritisch en creatief heeft leren denken. Bedankt voor alle urenlange gesprekken die we hebben gevoerd, voor de deur die altijd open stond, zowel voor werk als voor persoonlijke aangelegenheden. Frank Vergeldt, jouw nuchtere kijk heeft me meer dan eens met beide benen op de grond gezet, het samenwerken met jou hoort zeker bij de hoogtepunten van de afgelopen jaren. De technische oplossingen van Adrie de Jager waren altijd innovatief, en daarnaast hebben we *en passant* over de jaren de hele wereld en omstreken onder de loep genomen. Tjeerd Schaafsma, bedankt voor alle vrijheid die je me gunde om te doen wat ik leuk vond en voor het optreden als mijn promotor.

Een van de leukste aspecten was het samenwerken met studenten. Tom Ruttink, Mireille Claessens, Lucas Herfst en Christie Efdé, jullie hebben allemaal je steentje bijgedragen. Tom S., Carel en Sander, jullie brachten het nodige leven in de brouwerij. Alle andere collega's, bedankt voor jullie hulp en de gezelligheid.

Een aantal mensen hebben letterlijk als mijn handen gefungeerd. Papa en mama, Martine, Gerda, Henrieke, Shirley, Ruth en tante Adrie, zonder jullie had dit nog veel langer geduurd. Ik hoop dat het niet al te saai was, maar jullie snappen nu tenminste wel waar dit proefschrift over gaat. Ton, jij moet speciaal vermeld worden. Alle doorwaakte nachten hebben hun vrucht afgeworpen: de opmaak van dit boekje ziet er prachtig uit.

Papa en mama, jullie hebben een veel grotere rol gespeeld in dit geheel dat jullie misschien zelf beseffen. Bedankt voor alle steun, en pap, ik ben blij dat je me meegeeslept hebt naar de open dag. Lieve Jaap, jij hebt zoveel gedaan, dat valt niet in woorden te vatten. Leven met jou is een heel bijzonder voorrecht.

1

INTRODUCTION

GENERAL INTRODUCTION

Water is of major importance to plant life. Herbaceous plants consist of water for up to 95% of their total weight. The distinct properties of water make it very suitable for numerous roles, ranging from being the most important solvent and a component in many reactions to maintaining the form in non-woody plants.^{1,2} The extremely strong cohesion forces permit high negative pressures along the water column without breaking it, thereby enabling the flow of water through the transport vessels. Thus, clearly water shortage affects almost any parameter one cares to look at.¹

Lack of water affects large parts of the world, and water shortage becomes a larger problem for food production every year.^{3,4} Of the water that is available for use, about 70% is already used for agriculture. Water systems are under severe strain in many parts of the world. Many rivers no longer flow all the way to the sea and 50% of the world's wetlands have disappeared. Many major groundwater aquifers are being mined unsustainably, with water tables in parts of Mexico, India, China, and North Africa declining by as much as one meter per year.⁵ In addition, increasing soil salinity poses similar problems to agriculture, *e.g.* in Israel and Australia, but even in the nearby Westland (The Netherlands). Long-term growth and crop yield are considerably reduced compared to the maximum attainable yield due to water stress, which is turning into an enormous social and environmental problem. Therefore, insight into plant responses and tolerance to drought stress is an extremely important issue.

This Thesis focuses on the effects of water stress on water relations in whole plants, such as uptake rates and growth rates, in combination with the water balance in the plant stem. To trace the cell water balance and the movement of water within the cells and over membranes, we used Nuclear Magnetic Resonance, in an attempt to unravel differences in (cell) water balance in drought susceptible and drought tolerant plants.

Nuclear Magnetic Resonance Imaging (NMR imaging or MRI) is a non-invasive technique and therefore particularly useful for *in vivo* studies of plants. In addition to anatomical information, NMR images contain information about the physical status and the spatial distribution of water in tissues. Since the discovery of NMR, several experiments and theories have been developed to extract important physiological information, such as cell size and the exchange velocity of water over membranes. Most commonly, this information is obtained from relaxation and diffusion measurements, which are discussed later in this Chapter.

PLANTS

PLANT WATER STATUS

Plant water relations are commonly described using a thermodynamical approach.⁶⁻⁸ This approach is based upon the description of water in terms of energy, with the water potential as the measuring unit. The water potential of the liquid phase (Ψ_w) consists of three different components: the osmotic pressure (Ψ_π), the hydrostatic pressure (Ψ_p) and the gravitational pressure (Ψ_g):

$$\Psi_w = \Psi_\pi + \Psi_p + \Psi_g \quad [1.1]$$

The unit for all pressures is the Pascal (Pa).

The first term in Eqn. 1.1, the osmotic potential, represents the effect of solutes in an aqueous solution on the water potential. Assuming ideal conditions, the Van 't Hoff relation can be used to describe the relation between the solute concentration and the osmotic pressure:

$$\Psi_\pi = -RT \sum C_i \quad [1.2]$$

in which $\sum C_i$ is the total solute concentration (mol m^{-3}), R is the gas constant ($8.3143 \text{ J mol}^{-1} \text{ K}^{-1}$) and T is the absolute temperature (K).

The hydrostatic pressure is the effect of pulling or compression forces on the water molecules, and can be both positive (cell turgor) and negative (xylem tension). Gravitation also influences the water potential, but for small plants this component is negligible.

According to this thermodynamical approach, the flow is driven by a potential difference. Equivalent to current in electrical circuits, water always flows from high to low water potential and the flow rate is determined by the resistance of the system, analogous to Ohm's Law:

$$J_v = (\Delta\Psi_w) / R_{hydr} \quad [1.3]$$

in which J_v is the net flow of water ($\text{m}^3 \text{ s}^{-1}$), $\Delta\Psi_w$ is the water potential gradient, and R_{hydr} is the hydraulic resistance ($\text{m}^{-3} \text{ s Pa}$).

The potential difference over an entire plant is determined by the water potential differences between soil and air. The latter depends primarily on the relative humidity (rh) of the air:

$$\Psi_w^{vap} = (RT/V_w) \ln(rh) \quad [1.4]$$

in which Ψ_w^{vap} is the water potential in the vapour phase, and V_w is the partial molal volume of water (Fig. 1.1).

The hydraulic resistance varies enormously between plant tissues. It is smallest within the conducting system, i.e. the xylem and phloem vessels, due to the absence of cellular barriers. Outside the conducting tissues, the hydraulic resistance is much higher because water has to move either via the apoplast pathway (extracellular) or via the symplastic pathway, which is subdivided in the transmembrane route and the plasmodesmatal route (Fig. 1.2). Although the relative importance of both pathways is not yet clearly established, water transport via the symplastic route seems to account for a significant part of the transcellular transport. The main transitions occur at the soil-root interface and at the leaf-air interface.

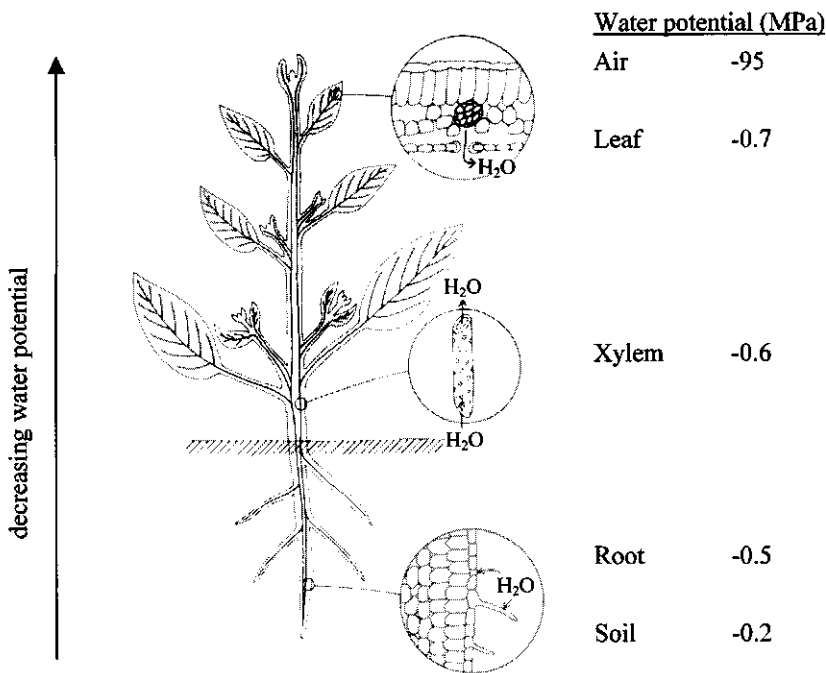


Figure 1.1. A negative water potential gradient in the plant body. When the water potential of the roots is less than that of the soil, water flows into the epidermal cells of the root and passes into the xylem tissue. Via the xylem vessels water flows through the stem and leaves and exits from the leaves as water vapor.

According to the Lockhart theory, the rate of cell expansion is determined by both the above mentioned potential difference and the tissue resistance.⁹⁻¹¹ Furthermore, the Lockhart equation suggests that the rate of cell expansion is limited by the extension properties of the expanding cell walls, the so-called cell wall extensibility:

$$\partial V/\partial t = m(\Psi_p - P^*) \quad [1.5]$$

in which $\partial V/\partial t$ is the cell volume change in time, and m is the cell wall extensibility. P^* is the threshold pressure potential, or yield turgor, which is the minimum pressure required to initiate cell growth.^{9,12}

The most important cause for water transport in a plant is transpiration. More than 90% of the water uptake passes through the plant directly into the atmosphere. The rest of the water is used for expansion growth. Furthermore, changes in the relative water content of tissues, *i.e.* de- or rehydration, also contribute to the total water transport. All these contributions can be combined into the water balance equation:

$$U = E + G + H \quad [1.6]$$

Here U is the water uptake rate, E is the transpiration rate, G is the water use for growth, and H is the water flow due to de- or rehydration, all in $\text{m}^3 \text{s}^{-1}$.¹⁰

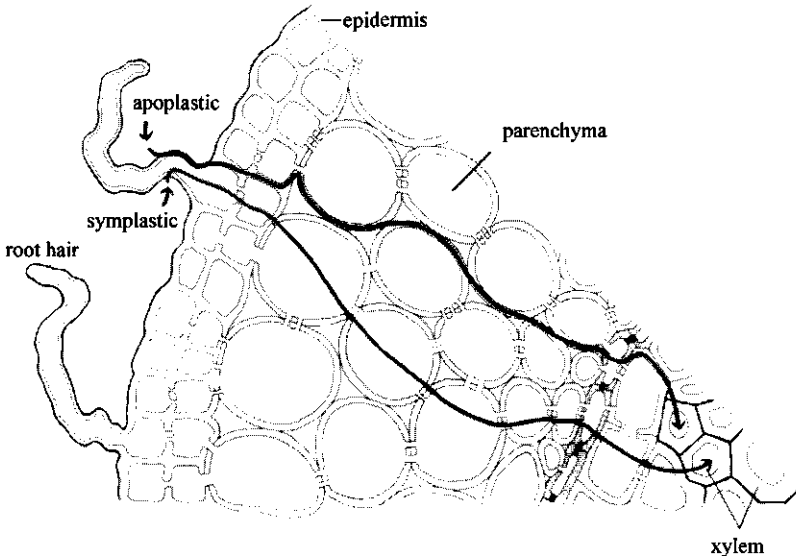


Figure 1.2. Principal pathways for the movement of water from the soil, across the epidermis and parenchyma, into the conducting root vessels. Water can follow several routes, either via the extracellular space (apoplastic pathway) or through the cells via the plasmodesmata and tonoplast and plasmalemma (symplastic pathway).

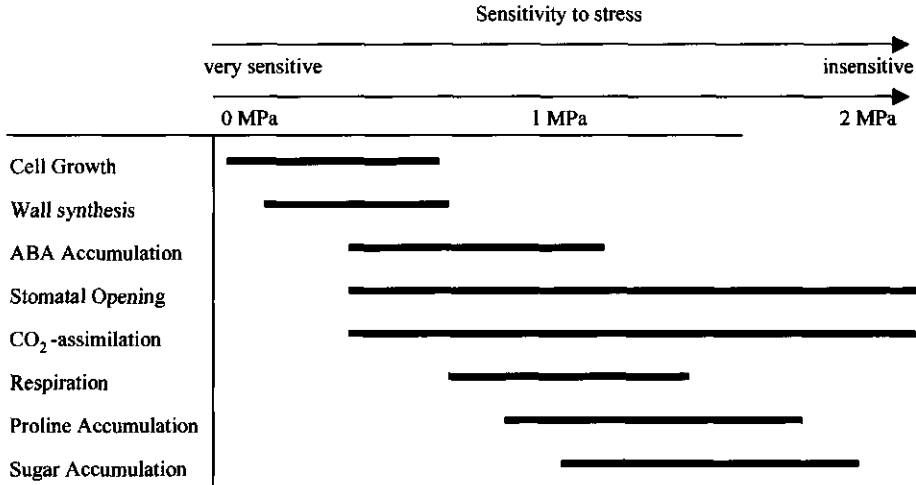


Table 1.1. Generalised sensitivity to water stress of plant processes.

WATER STRESS IN PLANTS

In nature short-term water deficits occur during midday, due to the high temperature and light level. Mostly, the water losses can be compensated at night, and over an entire day no net water losses occur. If however the uptake at night is not high enough to compensate for the water losses during the day, long-term water deficits develop, firstly resulting in decreasing growth rate and eventually in dehydration of all tissues. Apart from the changes in water status, the physiological functioning of the plants is affected at all organisational levels (Table 1.1).^{2,6,13,14} Here we concentrate only on the changes in water potential, though of course a range of biochemical and hormonal changes occur as well.^{15,16}

The uptake rate of water by the roots is closely coupled to transpiration. Usually, evaporation from the leaves is the main factor causing low pressure potentials in the root xylem. Closing the stomata and reducing the leaf area, *e.g.* by wilting or leaf rolling can reduce water loss due to evaporation. Stomatal closure is one of the first responses to water stress and occurs as a result of turgor loss in the guard cells surrounding the stomata. The resulting increase in stomatal resistance leads to an efficient decrease of the transpiration, which in turn results in a lower water uptake rate.^{6,17}

Another effect of drought is an almost immediate reduction of cell expansion. In many species cell expansion is the most sensitive to drought of all processes in the plant. The first response to stress is caused by a decrease in the cell turgor so that the yield turgor can not be overcome. Later on also metabolic changes and cell wall hardening can play a role in the

growth reduction. Some plants can maintain growth by increasing the osmotic potential or cell wall extensibility.¹⁸⁻²⁰

In some experiments, when water becomes available after a short period of stress, compensatory growth occurs so that the net crop yield is not reduced.²¹ When the water stress is prolonged, cell division can also be inhibited, thereby even further reducing the total growth and eventually also the crop yield.¹

When water stress causes a decrease in cell turgor, often compensatory mechanisms like osmotic adjustment occur. Usually a decrease in starch content and an increase in sugar and ion concentrations are found. Also the distribution of the assimilation products of photosynthesis over the various organs of the plant may change, which determines the survival chance of specific parts of the plant.^{6,15,21}

Changes in the hydraulic tissue conductance may occur during stress to regulate the water flow between different tissues. Membrane permeability for water regulates the water transport via the symplastic pathway (Fig. 1.2). Currently, there are two opposite views on the role of membrane permeability during stress. The first is that the membranes become less permeable for water to preserve as much water as possible within the cells.^{22,23} The second is exactly the opposite, *i.e.* the membrane permeability is increased to facilitate water movement towards growing cells or critical tissues.^{24,25}

Currently, much attention is focussed on the role of aquaporins, or membrane water channels, in the regulation of membrane permeability.²⁶ Recent reports show that aquaporin gene expression can be either upregulated or downregulated during stress, in agreement with the two above-mentioned views, depending on the plant tissue or stress involved.²⁷ These findings indeed suggest that the membrane permeability could play a role in the hydraulic conductance, thereby influencing all above mentioned processes; however, very little is known about the actual functioning of these proteins *in vivo* during stress. One of the goals of our research was therefore to find a relation between the membrane permeability and NMR parameters such as T_2 and D_{app} , in order to observe tissue hydraulics *in vivo* during stress.

NUCLEAR MAGNETIC RESONANCE IMAGING

Some important principles are discussed here to provide a background for the rest of this Thesis. For a more detailed introduction to NMR imaging we refer to various excellent textbooks.^{28,29}

RELAXATION

Protons have a nuclear magnetic moment denoted "spin", which is characterised by the spin quantum number I ($1/2$ for protons). In the absence of an external magnetic field these magnetic moments are randomly distributed in every direction. In the presence of such a magnetic field, a new thermal equilibrium is achieved between the spins oriented parallel and antiparallel to the magnetic field. This results in a net macroscopic magnetic moment, the magnetisation (M_0), in the direction of the external field (z-axis). The individual spins are precessing around the z-axis with the so-called Larmor frequency (ω , rad s^{-1}), which is proportional to the external magnetic field (B_0 , T) :

$$\omega = \gamma B_0 \quad [1.7]$$

where γ is the gyromagnetic ratio (4.2576×10^7 rad $T^{-1} s^{-1}$ for protons).

For NMR imaging, magnetic field gradients are applied in addition to the static magnetic field B_0 . Thus the actual magnetic field strength at the proton under observation depends on its position (r), and the Larmor frequency varies with the location of the spins in the sample:

$$\omega(r) = \gamma B(r) = \gamma(B_0 + Gr) \quad [1.8]$$

This results in a time dependent NMR signal $S(t)$:

$$S(t) \sim \int M_0(r) \exp(i\omega(r)t) \partial r \quad [1.9]$$

Fourier transformation of $S(t)$ yields the different frequencies present, and thereby the spatial localisation of local magnetisation $M_0(r)$ in the sample. By applying three different gradients in all three directions, each position in the sample is uniquely encoded.

M_0 is proportional to the total amount of protons present in the sample. To be able to detect the magnetisation M_0 , the magnetisation is rotated by 90° into the transverse plane (xy). Immediately following this 90° pulse, the initial magnetisation level can be detected. In time, the thermal equilibrium is restored, and the magnetisation vector returns to the z-axis. The

characteristic time involved in this process is called the spin relaxation time. It can be separated into two different components, the longitudinal relaxation time T_1 for the restoration of the M_0 vector along the z-axis, and the transverse relaxation time T_2 for the decay of this vector in the xy-plane (Fig. 1.3).

The protons in water molecules experience an intramolecular dipolar interaction between both protons within the one and the same molecule, as well as an intermolecular interaction with protons of neighbouring water molecules. Both interactions fluctuate when the molecules rotate or translate. When the rotation correlation time of the molecules is short, as is the case for free water molecules ($\tau_c \sim 10^{-12}$ s), T_1 and T_2 are approximately equal and relatively long (~ 2 sec). Water close to macromolecules or to solid surfaces generally has slower tumbling rates ($\tau_c \sim 10^{-12} - 10^{-10}$ s), which leads to a reduction in both relaxation times. For very slow motion ($\tau_c > 10^{-10}$ s), the transverse relaxation time T_2 continues to decrease while the longitudinal relaxation time T_1 increases again. Exchange of protons between water and other molecules such as sugars and proteins also influences the relaxation times. In biological tissue these principles determine the bulk relaxation times within compartments with different properties, such as the vacuole, the protoplasm and the cell wall. At low magnetic field strengths, the influence of chemical exchange is usually small as compared to the effect of rotational correlation times.

In addition to these bulk processes, the transverse magnetisation is perturbed by small local magnetic field differences, due to inhomogeneities in the main magnetic field, or due to the presence of (paramagnetic) molecules that cause a local disturbance of the magnetic field. This results in a different (local) Larmor precession frequency of the spins under observation and thus in a loss of phase coherence of the individual spins. In turn, this results in a faster decay of the M_0 vector in the xy-plane. The corresponding apparent relaxation time is called T_2^* to distinguish it from the real relaxation time T_2 . The loss of phase coherence can be reversed by the application of a 180° pulse following the initial 90° radiofrequency pulse. The restoration of the sample magnetisation is called an echo. The amplitude of this echo is only attenuated by the intrinsic transverse relaxation process.

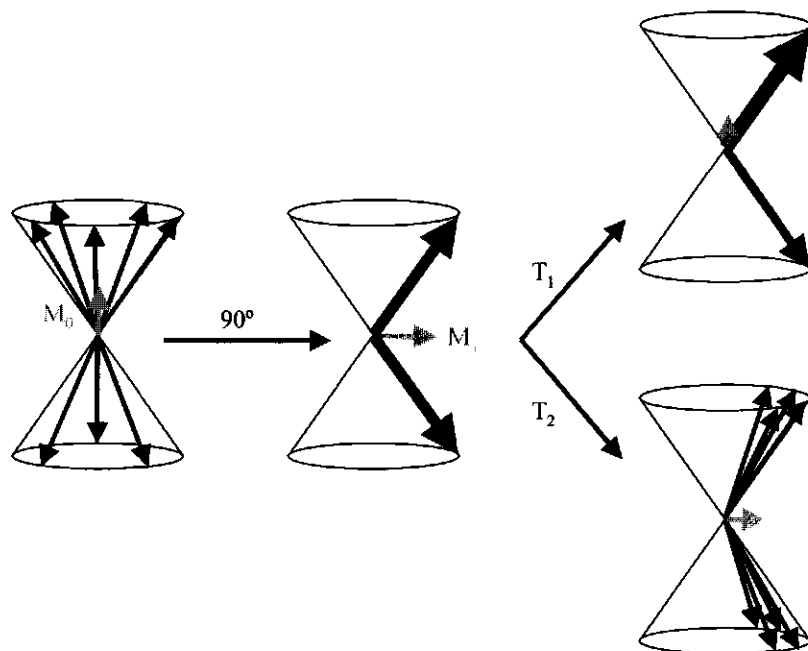


Figure 1.3. Schematic representation of the nuclear resonance principle. The sample magnetisation M_0 arises from the uneven distribution of the spins (the small arrows) between two different states, either parallel or anti-parallel to the main magnetic field B_0 . The spins precess around the main magnetic field direction with the Larmor frequency ω . After the application of a 90° pulse, the original distribution is shifted into the horizontal plane and phase coherence is established (the spins are all aligned along the same axis). The result is a sample magnetisation M_1 . The spins return to the original distribution through T_1 relaxation. The loss of phase coherence is called T_2 relaxation. Both processes occur simultaneously but are depicted separately in the picture.

DIFFUSION

Up to now, the individual molecules were considered as stationary molecules. However, all molecules in a fluid are subject to Brownian motion. The extent of this motion depends on the temperature and the viscosity of the fluid. When an ensemble of molecules is followed in time, the mean displacement (x, m) shows a \sqrt{t} dependence:

$$x = \sqrt{2dDt} \quad [1.10]$$

where D is the bulk diffusion coefficient of the fluid ($\text{m}^2 \text{s}^{-1}$), t is the displacement time (s) and d (= 1, 2, or 3) is the dimensionality of the diffusion displacement. The displacement distribution of all spins shows a Gaussian behaviour. The mean displacement distance increases with increasing displacement times as long as no boundaries are encountered. If water experiences a barrier to diffusion, for example a cell membrane, the cell dimensions determine the maximum displacement.

These boundary restrictions imply that the displacement distribution may no longer be Gaussian and is going to depend on the diffusion time. Consequently the experiments result in an apparent diffusion coefficient (D_{app}), which is smaller than the intrinsic D .

D_{app} can be measured using a so-called pulsed field gradient (PFG) experiment. In this experiment a sequence of two pulsed magnetic field gradients of equal magnitude but opposite sign, separated by an interval Δ temporarily change the resonance frequency of the observed spins as a function of the position of the spins (Eqn. 1.8). If the spins remain at exactly the same position during this interval Δ , the effects of the gradient pulses compensate each other. However, as soon as translational motion occurs, the gradients do not exactly compensate each other anymore and a phase shift occurs. Because diffusion is random in all directions, no net phase shift results but the phase coherence is partially lost, resulting in attenuation of the echo amplitude. The amount of this attenuation is determined by the length and amplitude of the gradient pulses, and by the mean translational distance travelled during the interval Δ . The distance travelled depends on the bulk diffusion coefficient of the fluid in the compartment and its dimensions.

NMR IMAGING OF HETEROGENEOUS SYSTEMS

In addition to the bulk properties mentioned in the previous paragraphs, exchange of molecules between different compartments may take place, which affects all relaxation rates and apparent diffusion coefficients. The mean time it takes for a proton to diffuse to the next compartment is determined by the molecular diffusion rate and by the size of the compartment. Exchange can be labelled as slow when this diffusion time is slow compared to the relaxation rate in that compartment and fast if the opposite is true. In the first case, the total magnetisation decay is multi-exponential and consists of the sum of the decay curves for the individual compartments. In the latter case, a common single relaxation curve is observed for the whole system. In the intermediate case, some form of multi-exponential behaviour is found, but the different components reflect both the properties of the original compartments and the exchange between them.^{28,30-34} The water exchange rate is determined by the permeability of the membranes separating the compartments. This Thesis treats the relation between the properties of the individual compartments and the resulting NMR parameters.

MAIN RESEARCH QUESTIONS

1. How can we obtain correct parameters from the NMR data?

Chapter 2 of this Thesis describes several fitting procedures for relaxation decays. Subsequently, in Chapters 5-7, the transverse relaxation times (T_2) are used to extract quantitative information about cell dimensions and membrane permeabilities. Therefore, correct data fitting is crucial. The effect of absolute data fitting is discussed and systematic errors are evaluated for different S/N ratios. In addition, some more elaborate routines such as the use of squared data and phase correction schemes are discussed and recommendations are made for optimal processing of the imaging data.

2. What is the theoretical relation between the properties of the individual compartments in a multi-compartment system and the NMR results for the system as a whole?

In Chapter 3 a numerical model is introduced with which both relaxation and diffusion can be modelled for cylindrical geometries. Several cases are presented, using this model, demonstrating how the combination of relaxation and diffusion enhances the separation of different fractions and enables a better understanding of the simulated system.

Chapter 4 is an extension of Chapter 3. Here the same cylindrical model is used to evaluate the effect of exchange between compartments in a model plant cell with several cell compartments on the observed T_2 and D_{app} . Different systems with increasing complexity are investigated to verify whether the original properties of the system, such as radius, bulk diffusivity and membrane permeability, can be retrieved. Finally, this Chapter discusses the optimal strategy to obtain useful physiological information from real heterogeneous systems.

3. Is it possible to interpret NMR studies of drought stress in plants in terms of the properties of (sub-)cellular compartments, in particular the membrane permeability and cell size?

In Chapter 5 the effect of moderate drought stress on the stem growth and on the water uptake is discussed. Furthermore, a linear relation between the relaxation rate and cell dimensions is presented and verified experimentally. The proportionality coefficient is related to the membrane permeability.

Chapter 6 further elaborates on the causes of the changes in relaxation rates during drought stress in pearl millet. Additional techniques, such as Scanning Electron Microscopy, are used to conclude that changes in relaxation rates are caused by an increase of the membrane permeability during stress.

Chapter 7 reports the results of MRI experiments of maize and pearl millet plants during severe drought stress. T_2 measurements are used to interpret the stress response in terms of cell size and water re-allocation between tissues.

Finally, in Chapter 8 the results from the previous Chapters are combined and general discussion points and conclusions are given.

REFERENCES

1. Hsiao T. (1973) Plant responses to water stress. *Annual Review on Plant Physiology* **24**, 519-570.
2. Baker D.A. (1985) Water relations. In: *Advanced plant physiology* (ed. Wilkins W.M.), 295-318. London, Longman
3. Boyer J.S. (1982) Plant productivity and environment. *Science* **218**, 443-448.
4. Turner (1997) Further progress in crop water relations. *Advances in Agronomy* **58**, 293-338.
5. Somerville C. & Briscoe J. (2001) Genetic engineering and water. *Science* **292**, 2217.
6. Kramer P.J. (1983) *Water relations of plants*. New York, Academic Press.
7. Passioura J.B. (1988) Water transport in and to roots. *Annual Review on Plant Physiology and Plant Molecular Biology* **39**, 245-265.
8. Slatyer R.O. (1967) *Plant-water relationships*. New York, Academic Press.
9. Lockhart J.A. (1965) An analysis of irreversible plant cell elongation. *Journal of Theoretical Biology* **8**, 264-275.
10. Boyer J.S. (1985) Water transport. *Annual Review on Plant Physiology* **36**, 473-516.
11. Cosgrove D.J. (1985) Cell wall yield properties of growing tissue. Evaluation by in vivo stress relaxation. *Plant Physiology* **78**, 347-356.
12. Neumann P.M. (1995) The role of cell wall adjustment in plant resistance to water deficits. *Crop Science* **35**, 1258-1266.
13. Taiz L. & Zeiger E. (1991) *Plant physiology*. Redwood City, California, The Benjamin/Cummings Publishing Company.
14. Hsiao T.C. (1973) Plant responses to water stress. *Annual Review of Plant Physiology* **24**, 519-570.
15. Ingram J. & Bartels D. (1996) The molecular basis of dehydration tolerance in plants. *Annual Review on Plant Physiology and Plant Molecular Biology* **47**, 377-403.
16. Yordanov I., Velikova V. & Tsonev A. (2000) Plant responses to drought, acclimation, and stress tolerance. *Photosynthetica* **38**, 171-186.
17. Premachandra G.S., Saneoka H., Fujita K. & Ogata S. (1992) Osmotic adjustment and stomatal response to water deficits in maize. *Journal of Experimental Botany* **43**, 1451-1456.
18. Neumann P.M., Azaizeh H. & Leon D. (1994) Hardening of root cell walls: A growth inhibitory response to salinity stress. *Plant, Cell and Environment* **17**, 303-309.
19. Cosgrove D.J. (1998) Cell wall loosening by expansins. *Plant Physiology* **118**, 333-339.
20. Kutschera U. & Schopfer P. (1986) Effect of auxin and abscisic acid on cell wall extensibility in maize coleoptiles. *Planta* **167**, 527-535.

21. Nonami H., Wu Y. & Boyer J.S. (1997) Decreased growth-induced water potential. *Plant Physiology* **114**, 501-509.
22. Johansson I., Karlsson M., Shukla V.K., Chrispeels M.J., Larsson C. & Kjellbom P. (1998) Water transport activity of the plasma membrane aquaporin PM28a is regulated by phosphorylation. *Plant Cell* **10**, 451-459.
23. Smart L.B., Moskal W.A., Cameron K.D. & Bennett A.B. (2001) MIP genes are down-regulated under drought stress in *Nicotiana glauca*. *Plant and Cell Physiology* **42**, 686-693.
24. Barrieu F., Marty M.D., Thomas D., Chaumont F., Charbonnier M. & Marty F. (1999) Desiccation and osmotic stress increase the abundance of mRNA of the tonoplast aquaporin BobTIP26-1 in cauliflower cells. *Planta* **209**, 77-86.
25. Yamada S., Komori T., Myers P.N., Kuwata S., Kubo T. & Imaseki H. (1997) Expression of plasma membrane water channel genes under water stress in *Nicotiana excelsior*. *Plant and Cell Physiology* **38**, 1226-1231.
26. Maurel C. (1997) Aquaporins and water permeability of plant membranes. *Annual Review of Plant Physiology and Plant Molecular Biology* **48**, 399-429.
27. Sarda X., Tusch D., Ferrare K., Legrand E., Dupuis J.M., CasseDelbart F. & Lamaze T. (1997) Two TIP-like genes encoding aquaporins are expressed in sunflower guard cells. *Plant Journal* **12**, 1103-1111.
28. Callaghan P.T. (1993) Principles of nuclear magnetic resonance microscopy. Oxford, Clarendon Press.
29. Gillies R. (1994) NMR in physiology and biomedicine. San Diego, Academic Press.
30. Snaar J.E.M. & Van As H. (1993) NMR self-diffusion measurements in a bounded system with loss of magnetization at the walls. *Journal of Magnetic Resonance A* **102**, 318-326.
31. Hills B.P. & Duce S.L. (1990) The influence of chemical and diffusive exchange on water proton transverse relaxation in plant tissues. *Magnetic Resonance Imaging* **8**, 321-332.
32. Hills B.P. & Quantin V.M. (1993) Water proton relaxation in dilute and unsaturated suspensions of nonporous particles. *Molecular Physics* **79**, 77-93.
33. Barsky D., Putz B. & Schulten K. (1997) Theory of heterogeneous relaxation in compartmentalized tissues. *Magnetic Resonance in Medicine* **37**, 666-675.
34. Novikov E.G., Van Dusschoten D. & Van As H. (1998) Modelling of self-diffusion and relaxation time NMR in multi-compartment systems. *Journal of Magnetic Resonance* **135**, 522-528.

2

EVALUATION OF ALGORITHMS FOR THE ANALYSIS OF NMR RELAXATION DECAY CURVES

Quantitative processing of NMR relaxation images depends on the characteristics of the used fitting algorithm. Therefore several common fitting algorithms are compared for decay curves with low signal-to-noise ratios. The use of magnitude data yields a non-zero base line, and is shown to result in an overestimation of the decay time. A simple base line correction is no solution since this yields an equally large underestimation due to overcorrection of the first part of the curve. The use of squared data does yield reliable results, but only in the case of monoexponential decays. The best fitting algorithm under all experimentally occurring conditions turns out to be using real data after phase correction. A phase correction scheme is proposed, which applies to all imaging experiments for which the phase of the pixels is constant over the echo train. This scheme is validated for a phantom and for a tulip bulb.

INTRODUCTION

Most biological tissues exhibit multiple T_2 components in the range from 1 to over 1000 milliseconds, which can be measured in a single T_2 imaging experiment.^{1,2} Depending on the relaxation time within a pixel, the sampling of the decay curve will vary considerably, and will not be optimal in all cases. The actual contrast in the image can be severely reduced due to the data processing routine, especially in the case of low signal-to-noise (S/N) ratios, which occur often in NMR imaging experiments. Moreover, the need for quantitative T_2 values increases now that quantitative relaxation times have been used in plant science^{3,4} as well as in medical applications, e.g. to measure the degree of myelination in nerves,⁵ to calculate the effective dose in radiotherapy⁶ or to monitor the progression of muscular dystrophy.⁷

Raw NMR relaxation data, obtained by quadrature detection, consist of a real and an imaginary part, which are corrupted by uncorrelated Gaussian distributed noise. After Fourier transformation, the complex data still have a Gaussian noise component because of the orthogonality of the Fourier transform. However, in MRI commonly the magnitude image is calculated from the real and imaginary part, resulting in a noise distribution that is no longer Gaussian, but Rician.⁸ As a result, the type of data processing routine influences the results of decay curve fits from the echo intensities obtained in a T_2 measurement.

This paper compares a number of published data processing routines using the magnitude of the echoes, only the real part of the data,² or methods to reduce the bias caused by Rician

noise, e.g. baseline correction,⁹ or power analysis.^{10,11} Maximum likelihood methods are not taken into account in this paper, but similar problems with low signal-to-noise echoes have been reported for these algorithms.^{12,13}

Using real data for the analysis, the image has to be phase-corrected first to transfer the signal to the real channel. A simple linear phase correction is not always satisfying; therefore we introduce a new approach, *i.e.* pixel-by-pixel phase correction of the echoes.

The various methods are used to fit artificially generated decay curves as well as experimental NMR imaging data. A comparison is made between the methods for various decay times and S/N ratios, both for single exponential and multiexponential behaviour. The importance of using a correct algorithm is demonstrated for T_2 images of a phantom and for a tulip bulb.

THEORY

For NMR imaging relaxation time measurements, a data set is acquired which consists of a complex, decaying signal for every pixel in the image. The number of echoes that can be acquired determines the number of data points in the decay curve. The true signal is corrupted by noise, causing a variation around both the real and the imaginary parts of the decay curves. According to Henkelman¹⁴ and Miller and Joseph,¹⁰ in the ideal case of Gaussian noise in both the real and imaginary channel, the complex signal after Fourier transformation can be described by

$$S = [(A_r + \varepsilon_r(0, \sigma)) + i(A_i + \varepsilon_i(0, \sigma))], \quad [2.1]$$

where S is the total signal, A_r and A_i are the real and imaginary components of the true signal respectively, and $\varepsilon_{r,i}(0, \sigma)$ is the Gaussian distributed noise with zero mean and standard deviation σ .¹⁴

In the case of phase-coherent measurements of the echo train,² it is possible to adjust the phase variation over the image mathematically by applying zero- and first-order phase corrections over the image for even and odd echoes separately, thus storing the true signal intensity and noise in the real channel, leaving only noise in the imaginary channel. Then the signal in the real and imaginary channel, respectively, can be written as

$$S_r = A + \varepsilon(0, \sigma) \quad \text{and} \quad S_i = \varepsilon(0, \sigma). \quad [2.2]$$

In this case, the average signal over a region of interest is given by

$$\langle S_r \rangle = A \quad \text{and} \quad \langle S_i \rangle = 0, \quad [2.3]$$

implying that the imaginary component can be discarded in the decay analysis.

However, it is common practice to use the magnitude signal to analyse the decay curves, because of severe phase distortions, or non-coherent phase variation in the echo train, or simply out of convenience. By doing so, the phase information is discarded and a Rician noise level is introduced with a non-zero average.

The magnitude signal $|S|$ can be described as

$$\begin{aligned} |S| &= [(A_r + \varepsilon_r(0, \sigma))^2 + (A_i + \varepsilon_i(0, \sigma))^2]^{1/2} \\ &= [A^2 + 2A_r \varepsilon_r(0, \sigma) + 2A_i \varepsilon_i(0, \sigma) + 2\varepsilon_{r,i}(0, \sigma)^2]^{1/2} \end{aligned} \quad [2.4]$$

and the corresponding average magnitude signal is

$$\langle |S| \rangle = [A^2 + 2\langle \varepsilon(0, \sigma)^2 \rangle]^{1/2} \quad [2.5]$$

When no true signal is present (A is zero), the noise distribution tends to a Rayleigh distribution with an average value of $[2\langle \varepsilon(0, \sigma)^2 \rangle]^{1/2}$ that is linearly related to the noise standard deviation by $\sigma\sqrt{\pi/2} \approx 1.253\sigma$,¹⁰ resulting in a non-zero base line in the decay curve. Though the noise is Rician distributed, Gudbjartsson and Patz⁶ showed that the distribution of noise is nearly Gaussian for S/N ratios larger than 2.

Sometimes a simple baseline subtraction of 1.253σ is used to compensate for this bias.⁹ Because of the non-linear magnitude calculation, however, (see Eqn. 2.5), this subtraction causes an overcompensation of the noise for high S/N levels.

Another method to overcome biases due to a non-zero base line, *i.e.* the use of power data, was suggested by Miller and Joseph¹⁰ and McGibney and Smith¹¹ independently. According to Eqn. 2.5, the average power signal is

$$\langle |S|^2 \rangle = A^2 + 2\langle \varepsilon(0, \sigma)^2 \rangle \quad [2.6]$$

Now the noise is simply additive to the power signal and can be corrected by a subtraction of the average noise level.

The signal for every echo point in the T_2 decay can be described as a function of the echo time by

$$S(t) = S_0 \exp(-t/T_2), \quad [2.7]$$

where t is $n \cdot TE$, n is the echo number and TE is the inter-echo time. When using power data the signal becomes

$$S^2(t) = S_0^2 \exp(-2t/T_2), \quad [2.8]$$

implying that the fitted T_2 value for power data is half the input T_2 value and the fitted amplitude is the power of the true value.

However, this power routine is only valid for monoexponential relaxation. Most biological samples are heterogeneous even within a single pixel, implying multi-exponential or non-exponential behaviour of the decay. In this case the resulting decay can be considered to consist of a number of decays with different relaxation times $T_{2,n}$:

$$S_{tot}(t) = \sum_0^n S_{0,n} \exp(-t/T_{2,n}). \quad [2.9]$$

The results for real data and magnitude data (Eqn. 2.3 and 2.5) apply to multiexponential decays as well. When using squared data however, the fitted T_2 values can deviate considerably due to the non-linear power operation, yielding an $S_{tot}(t)$ that consists not only of the n squared input exponentials but also of a number of cross terms, thus introducing $n!/2$ new exponentials.

The theory above already showed that using only the real part of the signal yields the most correct input data for fitting in the case of heterogeneous samples. However, in practice a simple linear phase correction of the echo images is not always possible. Therefore, we developed a new processing algorithm for experiments where the phase over the echoes is severely distorted. In this case, zero and first order phase corrections do not suffice to correct the phase deviations over the image plane. Because these phase problems are often caused by systematic errors as susceptibility artefacts or gradient and/or RF inhomogeneities, the phase deviations are constant over the entire echo train, although they may be different for odd and even echoes. Therefore, our algorithm is based on calculation of the phase of every pixel for the first and second echo images. These phase surfaces are used to correct all the following odd and even echoes in the echo train as follows:

$$\begin{aligned} \alpha_{corr}(2n) &= \text{atan}[(A_r(2n) + \varepsilon_r(0, \sigma)) / (A_r(2n) + \varepsilon_r(0, \sigma))] \\ &\quad - \text{atan}[(A_r(0) + \varepsilon_r(0, \sigma)) / (A_r(0) + \varepsilon_r(0, \sigma))] \\ &= (\alpha(2n) + \varepsilon_\alpha(0, \sigma)) - (\alpha(0) + \varepsilon_\alpha(0, \sigma)), \end{aligned} \quad [2.10a]$$

and

$$\begin{aligned} \alpha_{corr}(2n+1) &= \text{atan}[(A_r(2n+1) + \varepsilon_r(0,\sigma)) / (A_r(2n+1) + \varepsilon_r(0,\sigma))] \\ &\quad - \text{atan}[(A_r(1) + \varepsilon_r(0,\sigma)) / (A_r(1) + \varepsilon_r(0,\sigma))] \\ &= (\alpha(2n+1) + \varepsilon_\alpha(0,\sigma)) - (\alpha(1) + \varepsilon_\alpha(0,\sigma)), \end{aligned} \quad [2.10b]$$

where $\alpha_{corr}(n)$ is the corrected phase of a pixel in the n^{th} echo image and $\alpha(0)$ that of the same pixel in the first echo image. $\varepsilon_\alpha(0,\sigma)$ is the Gaussian distributed noise over the phase angle.

The complex signal for every echo in the echo train can then be calculated per pixel by

$$S_{corr}(n) = [(\cos(\alpha_{corr}(n)) \cdot |S|) + i(\sin(\alpha_{corr}(n)) \cdot |S|)] \quad [2.11]$$

By using this pixel-by-pixel phase correction, the first and second echo are in fact magnitude images, but the rest of the echoes show a normal Gaussian noise distribution, with zero mean. To improve the phase correction for low S/N pixels in the image, a Gaussian smoothing can be applied to the calculated phase image to eliminate phase variance due to noise.

METHODS

To evaluate the performance of the processing algorithms, complex data sets were generated consisting of decay curves of 128 points with 1 ms echo spacing in the real channel, with 16 different decay times varying from 3.3 ms to 1 s, resulting in a series of decays with varying amounts of baseline sampled (Fig. 2.1).

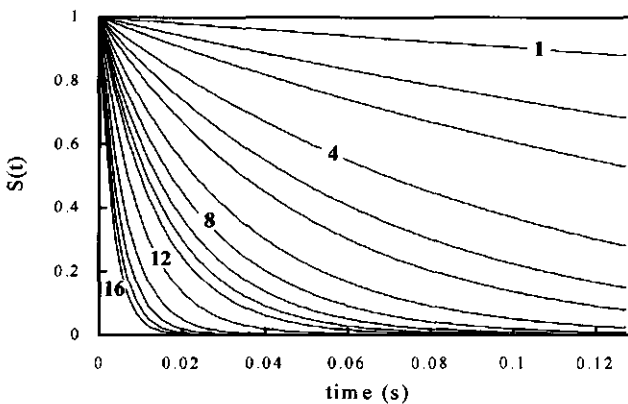


Figure 2.1. The simulated decay curves that were used for fitting.

To both the real and the imaginary components of each decay curve random Gaussian noise with 16 different amplitudes was added, resulting in a series of complex decay curves with a root mean square (RMS) noise level of 0 to 7.5% of S_0 , the signal intensity at $t = 0$, in both channels. For all conditions a Monte Carlo simulation was performed with 64 trials, from which the average and the standard deviation of the fit results for S_0 and T_2 were determined.

For the T_2 fit a least square fit routine without weighting factors was performed using Interactive Data Language (RSI, Boulder, Colorado, USA), based on the Marquardt-Levenberg algorithm.¹⁵ The magnitude and power data were computed in accordance with the theory described above. The baseline correction was done by calculating the standard deviation σ for the last part of the shortest decay for every noise level and using this value for all decay curves of the corresponding noise level. For our pixel-by-pixel phase correction scheme first a linear phase correction was done in the frequency domain in order to get most of the signal in the real channel. Next a broad ($10 \times$ signal width) Gaussian convolution was done in the time domain to smooth the phase data to obtain a correct phase adjustment for low S/N pixels as well. After Fourier transformation back into the frequency domain, the phase per pixel was calculated for phase correction of the entire echo train.

The chi-square for each individual curve was determined from

$$\chi^2 = \frac{\sum_{i=1}^{i=128} ((S_{f,i} - S_i) / \sigma_i)^2}{128} \quad [2.12]$$

where $S_{f,i}$ is the fit result for point i , S_i is the input data point and σ_i is the standard deviation for that point.

To simulate a biological system, curves were generated which consisted of the sum of three exponential components. The values for the exponentials were chosen in accordance with earlier results for multi-exponential relaxation in apple tissue that yielded 3 relaxation times of 330, 100 and 20 ms, which could be assigned to water in the vacuole, the cytoplasm and the cell wall / extra cellular space respectively.⁴ The relative amplitudes of these three fractions were 0.75, 0.18 and 0.07.

A phantom and a tulip bulb were used to demonstrate the effect of the procedures on a real experiment. For all measurements a 0.5 T S.M.I.S. imaging system (S.M.I.S., Guildford, UK) was used with a Doty probe (Doty Scientific Inc., Columbia, South Carolina, USA). A modified CPMG experiment was used to obtain the data.² The phantom consisted of six tubes filled with different $MnCl_2$ solutions, which varied in $1/T_2$ values from 185 s^{-1} to less than 0.62 s^{-1} . The data were acquired with $TR = 1500 \text{ ms}$ and $TE = 4.6 \text{ ms}$. A 128×128 image matrix was obtained with a 55 mm field of view and a slice thickness of 3 mm. For every

pixel 46 echoes were acquired. To compare images with different S/N ratios, a noisy image of the phantom was obtained by decreasing the slice thickness to 0.75 mm, yielding an average noise level over the image of approximately 20%, compared to about 5% noise for the S/N image of a 3 mm slice. For the tulip bulb the average noise level was 10% noise for the first echo.

RESULTS AND DISCUSSION

First the monoexponential decay curves were analysed using the four algorithms described previously. To visualise the accuracy of the algorithms, the results are presented as the fitted values for the amplitude and $1/T_2$ divided by the input values A_{in} and $1/T_{2,in}$.

As can be seen in Figs. 2.2A and 2.3A, using the real data yields no bias for either the amplitude or the $1/T_2$ of the decay curves. As an additional treat, the signal in the imaginary channel can be discarded. Thus, the S/N ratio of the data points near the noise level is significantly improved compared to the magnitude data, resulting in more accurate fits.

For the magnitude data a consistent error is made for input decay curves that are sampled until the base line (Figs. 2.2B and 2.3B). The lower the S/N ratio and the more base line is sampled, the larger the bias is. For the two longest $1/T_2$ decay curves, which have only a few data points containing signal, the fit results show very large deviations because the base line is fitted for the lower S/N ratios. For completely sampled decay curves with a reasonable amount of signal-containing data points, a rule of the thumb is that the negative bias of the fitted $1/T_2$ value is about 3% per percent noise for the first echo (Fig. 2.3B, curves 7-14).

Using a simple base line correction does not solve the problem. As can be seen in Fig. 2.2C, the underestimation of the amplitude is almost linear with the noise level and independent of the relaxation time, a deviation that is caused by the subtraction of the base line of the initial part of the decay curve. In this case the fitted $1/T_2$ is too high (Fig. 2.3C), and the curves without base line also deviate from the true values. The maximum error in $1/T_2$ for completely relaxed decays with 7.5% noise is 25%. In general, the bias made using this algorithm is just as large as for the magnitude data, only in this case the $1/T_2$ values are overestimated.

In contrast to the previous two algorithms, the power algorithm yields unbiased results for both the $1/T_2$ and the amplitude (Figs. 2.2D and 2.3D).

The average chi-square values for both the real and the power fit were 1.0 for all curves and all noise levels (Fig. 2.4), indicating a perfect fit. Both the magnitude fit and the base-line corrected magnitude fit show an increased chi-square value, though the deviations for the first are far worse because in this case the curve is no longer mono-exponential due to the base line. For all fit procedures, the standard deviation over the 64 curves per noise level increased with increasing noise level.

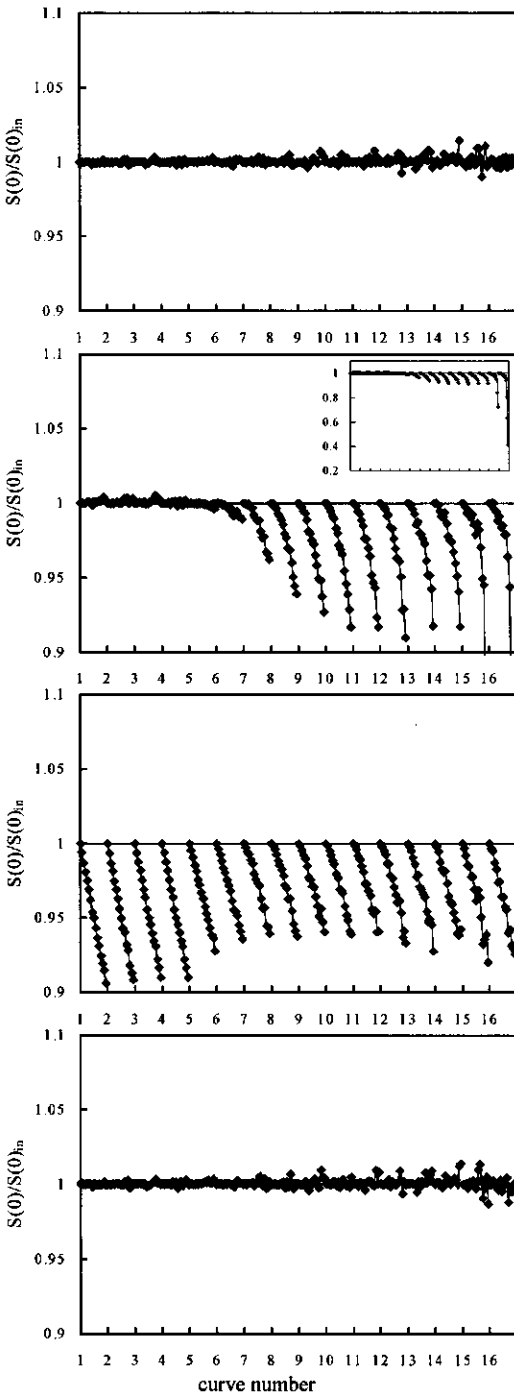


Figure 2.2. Amplitude fits for different algorithms. The numbers along the horizontal axis indicate the 16 decay curves that were used, with increasing $1/T_2$ values from left to right. The 16 data points shown for each decay curve are the different noise levels, increasing from left to right from 0 to 7.5% RMS noise for the first echo of the decay. Every data point is the mean of 64 fits. A. real data; B. magnitude data; C. magnitude data with base line correction; D. power data.

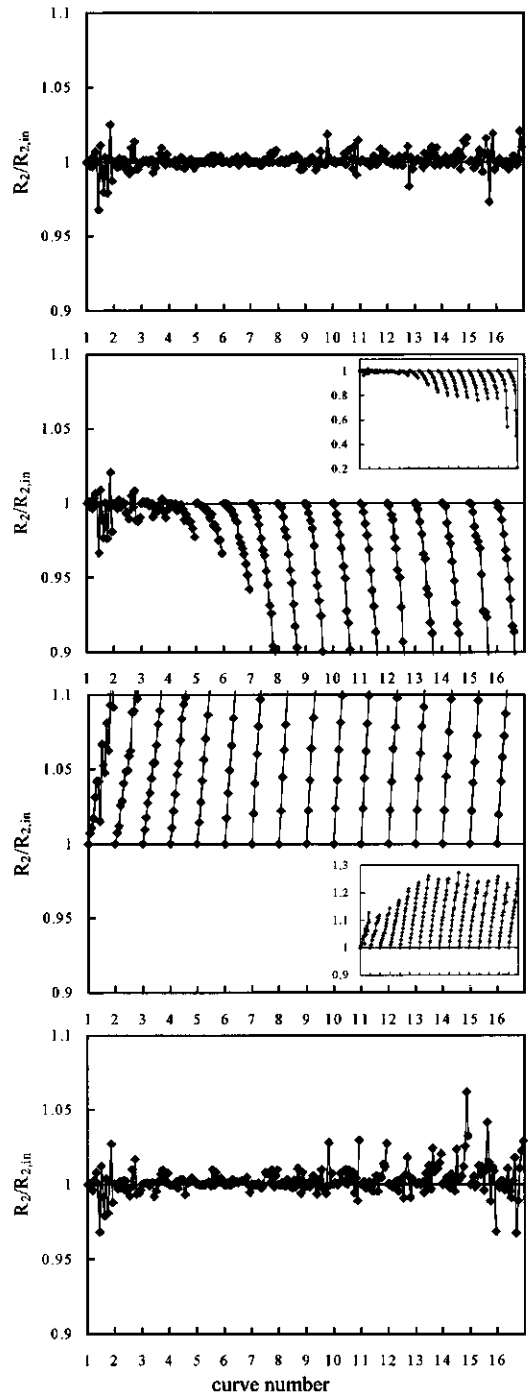


Figure 2.3. $1/T_2$ fits for different algorithms. The numbers along the horizontal axis indicate the 16 decay curves that were used, with increasing $1/T_2$ values from left to right. The 16 data points shown for each decay curve are the different noise levels, increasing from left to right from 0 to 7.5% RMS noise for the first echo of the decay. Every data point is the mean of 64 fits. A. real data; B. magnitude data; C. magnitude data with base line correction; D. power data.

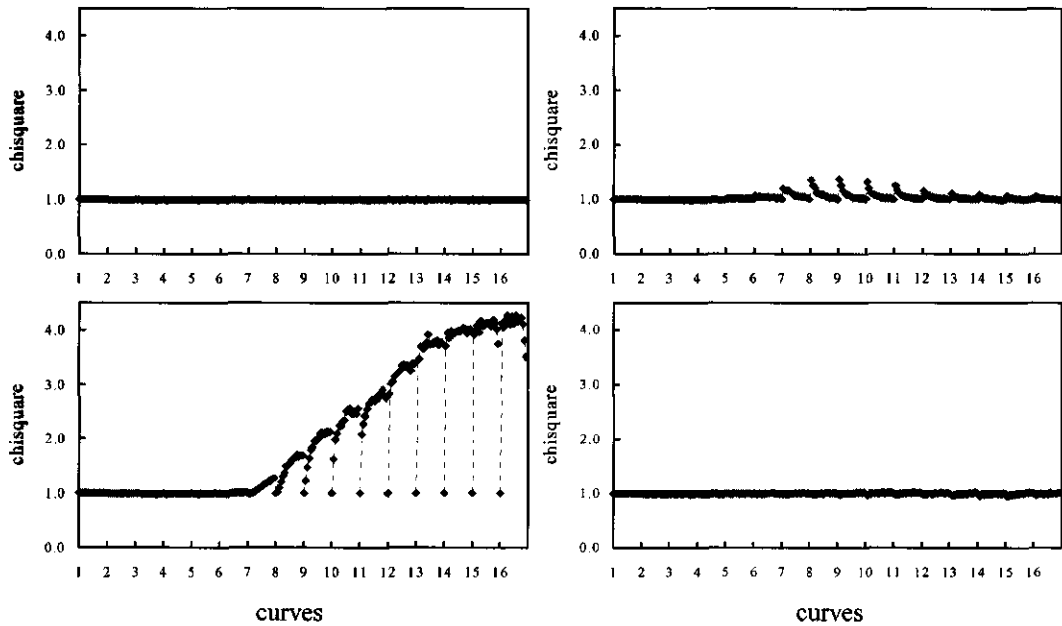


Figure 2.4. The average chi-square values for the $1/T_2$ fits in Fig. 2.3. The numbers along the horizontal axis indicate the 16 decay curves that were used, with increasing $1/T_2$ values from left to right. The 16 data points shown for each decay curve are the different noise levels, increasing from left to right from 0 to 7.5% RMS noise for the first echo of the decay. Every data point is the mean of 64 curves. A. real data; B. magnitude data; C. magnitude data with base line correction; D. power data.

Between the fit procedures, however, the standard deviation for the same dataset did not differ more than 10%, again indicating that the biases are systematic. In general, the standard deviation for the real fits of completely sampled curves was slightly ($< 10\%$) lower, due to the improved S/N ratio for data point close to the noise level.

Of course the use of monoexponential decays is a rather academic approach. In the case of multiexponential behaviour additional problems arise with respect to fitting the decay curve. This paper deals with the case of T_2 decays with a S/N ratio too poor to get meaningful results from a multiexponential fit. This implies that a monoexponential non-linear least square fit yields a T_2 value which has no physical meaning and which is dependent on the part of the decay curve used for the analysis. It is obvious that the calculated decay time becomes smaller when only the first part of the curve is used for analysis. When the signal used is completely relaxed at the end of the curve, the fit results remain constant. This indicates that a comparison of fit results is only valid when all decay curves used are measured completely, *i.e.* until the signal intensity becomes comparable to the noise level. The question whether a monoexponential analysis is the best procedure to evaluate these signals is beyond the scope of this paper.

Fig. 2.5 shows that the real, the magnitude and the base line corrected magnitude data analysis yield similar results as for monoexponential decays. The power algorithm, however, yields much higher $1/T_2$ values, even in the ideal case when no noise is present. As mentioned in the theory, this deviation is due to the cross-terms that are generated by squaring multiple exponents, resulting in extra decay terms with a much shorter T_2 value that cause a decrease of the calculated relaxation time. This bias increases when the different exponentials of which the decay is composed contribute more equally to the signal.

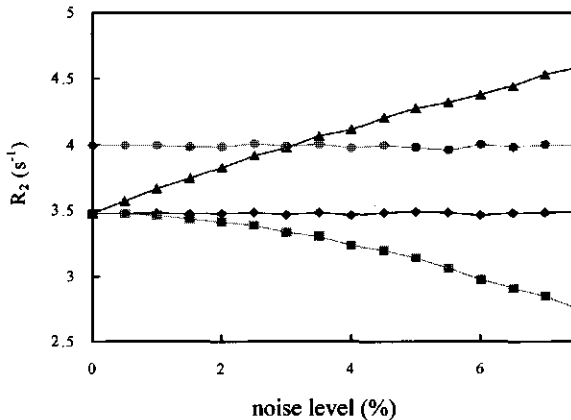


Figure 2.5. The $1/T_2$ fit of a multi-exponential decay as a function of the RMS noise level. Every data point is the mean of 64 fits. \blacklozenge real data; \blacksquare magnitude data; \blacktriangle magnitude data with base line correction; \bullet power data.

	magnitude		phased	
	5% RMS	20% RMS	5% RMS	20% RMS
Tube 1	174.9	3.041	185.5	194.1
Tube 2	99.77	14.47	124.0	107.3
Tube 3	33.17	26.19	34.12	33.85
Tube 4	16.41	15.30	16.68	16.74
Tube 5	8.169	8.042	8.411	8.398
Tube 6	0.6154	0.6416	0.6270	0.6960

Table 2.1. The $1/T_2$ results for magnitude and pixel-by-pixel phase corrected data of a phantom, for two different S/N ratios.

As a demonstration of the errors that can occur, images of six phantom tubes containing different MnCl_2 solutions were obtained with both high and low S/N ratios. The data were analysed using either the magnitude data or the pixel-by-pixel phase-corrected data. As expected, for the long $1/T_2$ values the magnitude fit was systematically lower for the 5% noise data, and yielded completely erroneous results when the noise level increased to 20% (Table 2.1). The decays of the tubes 5 and 6 were not sampled into the baseline, which explains the correct values for the magnitude fit in these cases.

As a final test the echo images of a tulip bulb were used. As can be seen in Fig. 2.6, the phase of the first echo image varies strongly over the image, showing the largest deviations in the pit and at the outer skirt of the bulb. For the data analysis three algorithms were used: the magnitude images, the real data after a linear phase correction and the real images obtained by our pixel-by-pixel phase correction scheme. Using the magnitude data yield pit $1/T_2$ values that are 23% smaller than those obtained for the pixel-by-pixel phase-corrected data (Fig. 2.7A). The outer skirts show a less severe deviation (12%) due to the smaller $1/T_2$ values in the skirts. Using a linear phase correction does not cause significant $1/T_2$ errors, because a consistent phase deviation over the echo train does not alter the decay shape. The signal amplitude, however, is decreased, because part of the signal intensity remains in the imaginary channel. In this example, this effect can be observed most clearly in the top left corner of the amplitude image (see arrow in Fig. 2.7B).



Figure 2.6. Phase image of a tulip bulb. The image is the first echo out of a CPMG echo train of 46 echoes.

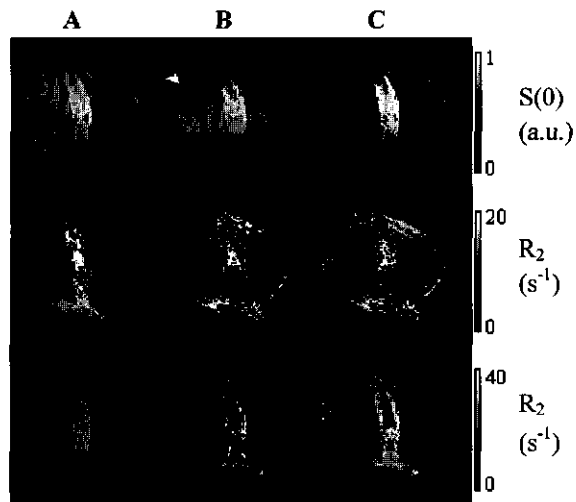


Figure 2.7. Fitted signal amplitudes and $1/T_2$ values for a tulip bulb. A. magnitude data; B. linear phase correction; C. pixel-by-pixel phase correction.

CONCLUSIONS

The use of magnitude data yields an overestimation of decay times, especially for low S/N ratios, because of the non-zero noise level. The bias increases with decreasing S/N ratio and can be as large as three times the relative noise level. A simple linear base line correction is no solution, for this algorithm results in too low T_2 values and amplitudes with comparable errors as the magnitude algorithm. To avoid biases for magnitude data, it is suggested to chop off the decay curve when the S/N ratio becomes less than 2.¹² However, by doing this the accuracy of the fit is decreased as well, as less data points are used for fitting. Moreover, for multiexponential decays other errors are introduced because the decay curve is not completely sampled. The use of power data can be a solution to the noise problem, but this method is only valid for monoexponential relaxation curves.

Since the magnitude and base line corrected magnitude algorithms are S/N ratio dependent, these algorithms should be interpreted with special care. A theoretical illustration of the implications of this fact is a biological sample where a calculated change in decay times can be caused either by physiological changes or by changes in the S/N ratio, e.g. due to a probe tuning drift in time. Another example is the use of amplitude and T_2 images to select homogeneous regions for further analysis. In the case of varying S/N ratios between regions, the amplitudes and T_2 values per pixel will show a different bias when magnitude data are used, resulting in imperfect selections.

Whenever possible it is recommended to use real data for decay analysis, for this method yields the best T_2 values independent of the noise level and the number of exponentials of which the decay is composed. Even when the phase correction is not perfect, the fitted relaxation times will be correct, although in this case the signal amplitudes are underestimated. When comparing data from literature one should be aware of the algorithm used. Therefore, it is necessary to mention the analysis algorithm and the S/N ratio in every paper. Once the analysis algorithm, the S/N ratio and the curve sampling are known, at least an estimation of the bias can be made from the simulations presented here.

ACKNOWLEDGEMENTS

This Chapter has been published as:

Van der Weerd L., Vergeldt F.J., De Jager P.A. & Van As H. (2000) Evaluation of algorithms for analysis of NMR relaxation decay curves. *Magnetic Resonance Imaging* **18**, 1151-1157.

We thank T.J. Schaafsma for useful comments. This work is a part of the Metabolism and Adaptation program of the graduate school Experimental Plant Sciences.

REFERENCES

1. Graham S.J., Stanchev P.L. & Bronskill M.J. (1996) Criteria for analysis of multicomponent tissue T_2 relaxation data. *Magnetic Resonance in Medicine* **35**, 370-378.
2. Edzes H.T., Van Dusschoten D. & Van As H. (1998) Quantitative T_2 imaging of plant tissues by means of multi-echo MRI microscopy. *Magnetic Resonance Imaging* **16**, 185-196.
3. Snaar J.E.M. & Van As H. (1992) Probing water compartments and membrane permeability in plant cells by ^1H NMR relaxation measurements. *Biophysical Journal* **63**, 1654-1658.
4. Donker H.C.W., Van As H., Snijder H.J. & Edzes H.T. (1997) Quantitative ^1H -NMR imaging of water in white button mushroom (*Agaricus bisporus*). *Magnetic Resonance Imaging* **15**, 113-121.
5. Beaulieu C., Fenrich F.R. & Allen P.S. Multicomponent water proton transverse relaxation and T_2 -discriminated water diffusion in myelinated and nonmyelinated nerve. *Magnetic Resonance Imaging* **16**, 1201-1210.
6. De Deene Y., De Wagter C., Van Duyse B., Derycke S., Mersseman B., De Gerssem W., Voet T., Achten E. & De Neve W. (2000) Validation of MR-based polymer gel dosimetry as a preclinical three-dimensional verification tool in conformal radiotherapy. *Magnetic Resonance in Medicine* **43**, 116-125.
7. Dunn J.F. & Zaim-Wadghiri Y. (1999) Quantitative magnetic resonance imaging of the mdx mouse model of Duchenne muscular dystrophy. *Muscle & Nerve* **22**, 1367-1371.
8. Gudbjartsson H. & Patz S. (1995) The Rician distribution of noisy MRI data. *Magnetic Resonance in Medicine* **34**, 910-914.
9. Yousem D.M., Ihmeida I., Quencer R. & Atlas S.W. (1991) Paradoxically decreased signal intensity on post contrast short-TR MR images. *Annual Journal of Nuclear Resonance* **12**, 875-880.
10. Miller A.J. & Joseph P.M. (1993) The use of power images to perform quantitative analysis on low SNR MR images. *Magnetic Resonance Imaging* **11**, 1051-1056.
11. McGibney G. & Smith M.R. (1993) An unbiased signal-to-noise-ratio measure for magnetic resonance images. *Medical Physics* **20**, 1077-1078.
12. Bonny J.M., Zanca M., Boire J.Y. & Veyre A. (1996) T_2 maximum likelihood estimation from multiple spin-echo magnitude images. *Magnetic Resonance in Medicine* **36**, 287-293.
13. Sijbers J., Den Dekker A.J., Scheunders P. & Van Dyck D. (1998) Maximum-likelihood estimation of Rician distribution parameters. *IEEE Transactions on Medical Imaging* **17**, 357-361.
14. Henkelman R.M. (1985). Measurement of signal intensities in the presence of noise in MR images. *Medical Physics* **12**, 232-233. Erratum in (1986) *Medical Physics* **13**, 544.

3

MODELLING OF SELF-DIFFUSION AND RELAXATION TIME NMR IN MULTI-COMPARTMENT SYSTEMS WITH CYLINDRICAL GEOMETRY

A numerical model of restricted diffusion and magnetisation relaxation behaviour in PFG-CPMG NMR experiments, based on Fick's second law of diffusion, has been extended for two-dimensional diffusion in systems with concentric cylindrical compartments separated by permeable walls. This model is applicable to a wide range of (cellular) systems and allows the exploration of temporal and spatial behaviour of the magnetisation with and without the influence of gradient pulses. Numerical experiments have been performed to show the correspondence between the obtained results and previously reported studies and to investigate the behaviour of the apparent diffusion coefficients for the multi-compartment systems with planar and cylindrical geometry. The results clearly demonstrate the importance of modelling two-dimensional diffusion in relation to the effect of restrictions, permeability of the membranes and the bulk relaxation within the compartments.

INTRODUCTION

Both pulsed field gradient NMR and relaxation time measurements are widely used to probe the molecular displacements of liquid molecules and the geometry of the microstructures containing them in porous and biological media.¹⁻⁴ In such systems the measured displacements and observed relaxation times contain information about the diffusivity within the compartments, the dimensions of the compartments, and the exchange between these compartments through semi-permeable membranes.⁵⁻¹⁴ If diffusion takes place in compartments separated by permeable membranes, as is the situation for most biological cells, the membrane permeability and differences in (bulk) relaxation times within the compartments strongly affect the shape of the signal attenuation plot (SAP) or the q-space spectrum and thus the apparent diffusion coefficient D^* . Especially the effect of differences in bulk relaxation on D^* has hardly been taken into consideration in literature, but clearly cannot be ignored.^{2,9,11,14}

Combining diffusion and relaxation time measurements and analysis, also called Diffusion Analysis by Relaxation Time Separation (DARTS),^{5,13} yields more detailed insight in the behaviour of the different liquid ensembles and the microstructure.^{10,12,15-18} However, for further improvement of the experimental set-up and analysis, and for a better understanding of

the complex molecular behaviour, we require adequate mathematical models to evaluate the effect of diffusion and relaxation on the observed NMR signal.

Among the broad spectrum of the reported modelling approaches, three ways are clearly distinguishable. The first approach is an analytical solution of the given partial differential equation for a certain combination of the initial and boundary conditions.^{11,19} Despite the fact that in this way solutions in a closed form are obtained, the number of analytically treated configurations is limited. Another approach consists of the detailed reproduction of every molecular movement and transformation using simulation methods.^{20,21} The position and orientation of every spin should be calculated for every time step, thus allowing the most extraordinary system configurations, but software implementation of such procedures may be very time-consuming even for simple configurations on powerful workstations. The compromise way of action is based on the numerical solution of the partial differential equation with respect to spin magnetisation.^{6,9,14} This approach ensures, on the one hand, reasonable speed of calculations and, on the other hand, the possibility to investigate rather complicated configurations. These models are generally based on the different evaluations of Fick's second law of diffusion.²² In this way, a variety of systems with complicated configurations can be modelled by simply defining appropriate initial and boundary conditions, combined with a proper description of the shape of the pulsed magnetic field gradients.^{11,19}

Previously, we reported a numerical model to simulate the combined diffusion and magnetisation relaxation behaviour in NMR experiments for planar geometries.⁹ However, more realistic models should, of course, take into account the (concentric) cylindrical symmetry of many biological objects. In this paper, an attempt to expand that model to incorporate two-dimensional diffusion is undertaken. Doing so, the effect of restricted diffusion and the possibility to circumvent a diffusion barrier by two-dimensional diffusion can be investigated. The approach is based on the numerical solution of Fick's diffusion equation in cylindrical coordinates. We also demonstrate the agreement of the obtained results with results that were reported previously for cylindrical geometries.

THEORY

A two-dimensional system is considered that consists of a set of concentric cylindrical compartments, each surrounded by a membrane (Fig. 3.1). The i -th compartment is characterised by an intrinsic relaxation time T_i and diffusion constant D_i , as well as by a radius R_i and permeabilities ρ_{i-1} and ρ_i for the inner and outer membrane, except for the innermost compartment where only an outer membrane is present.

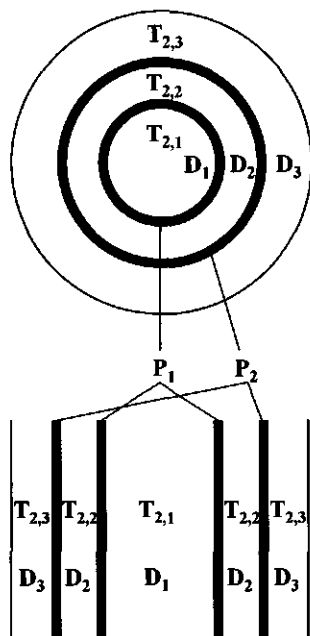


Figure 3.1. Structure of multicompartment systems with cylindrical and planar geometries.

The two-dimensional spin magnetisation density $S(r, \varphi, t)$ can be described in cylindrical coordinates by the following differential equation based on Fick's second law of diffusion, including the effect of relaxation:²²

$$\frac{\partial S(r, \varphi, t)}{\partial t} = \frac{\partial}{\partial r} \left\{ r D(r, \varphi) \frac{\partial S(r, \varphi, t)}{\partial r} \right\} + \frac{\partial}{\partial \varphi} \left\{ D(r, \varphi) \frac{\partial S(r, \varphi, t)}{\partial \varphi} \right\} - \frac{S(r, \varphi, t)}{T(r, \varphi)} \quad [3.1]$$

where $D(r, \varphi)$ and $T(r, \varphi)$ are the diffusion coefficient and relaxation time, respectively, as a function of the radius and angle. Diffusion and relaxation are assumed to be constant within a particular compartment, but may differ for different compartments. Eqn. 3.1 should be supplemented by a proper set of initial and boundary conditions. Magnetisation at time $t = 0$ takes the form:

$$S(r, \varphi, t)_{t=0} = f(r, \varphi) \quad [3.2]$$

where $f(r, \varphi)$ is the spin magnetisation density at time $t = 0$. The permeability ρ of the membranes is accounted for by boundary conditions in two dimensions and is formulated analogously to the one-dimensional case.⁹ For the internal and external membranes of the j -th compartment, one can then write:

$$\begin{aligned} \rho_{j-1} [S_j(R_{j-1}, \varphi, t) - S_{j-1}(R_{j-1}, \varphi, t)] &= D(R_{j-1}, \varphi) \frac{\partial S_j(R_{j-1}, \varphi, t)}{\partial r}, \\ \rho_j [S_{j+1}(R_j, \varphi, t) - S_j(R_j, \varphi, t)] &= D(R_j, \varphi) \frac{\partial S_j(R_j, \varphi, t)}{\partial r} \end{aligned} \quad [3.3]$$

where $S_j(r, \varphi, t) = S(r, \varphi, t)$, when $r \in [R_{j-1}, R_j]$, $j=1, \dots, n$, $R_0=0$ and n is the number of compartments. The outer border of the system is characterised by:

$$S_{n+1}(R_n, \varphi, t) = F(t) \quad [3.4]$$

where $F(t)$ is the outer spin magnetisation at time-step t .

The numerical solution of Eqn. 3.1 with the initial condition Eqn. 3.2 and boundary conditions Eqn. 3.3 is based on the transformation of Eqn. 3.1 to an equation in finite differences according to an implicit scheme:²³

$$\begin{aligned} S_{p,q}^{m+\frac{1}{2}} &= S_{p,q}^m + \frac{\Delta t}{2} (\phi_r^2 S_{p,q}^{m+\frac{1}{2}} + \phi_\varphi^2 S_{p,q}^m) - \frac{\Delta t S_{p,q}^{m+\frac{1}{2}}}{2T_{p,q}}, \\ S_{p,q}^{m+1} &= S_{p,q}^{m+\frac{1}{2}} + \frac{\Delta t}{2} (\phi_r^2 S_{p,q}^{m+\frac{1}{2}} + \phi_\varphi^2 S_{p,q}^{m+1}) - \frac{\Delta t S_{p,q}^{m+1}}{2T_{p,q}} \end{aligned} \quad [3.5]$$

where $S_{p,q}^m = S(r_p, \varphi_q, t_m)$, and the indexes m , p and q denote time step, radius step and angle step, respectively; ϕ_r^2 and ϕ_φ^2 are the finite differences of the second order with respect to radius and angle, respectively. The finite difference scheme of Eqn. 3.5 shows how spin magnetisation density at the next time step $S_{p,q}^{m+1} = S(r_p, \varphi_q, t_m + \Delta t)$ is calculated from the spin magnetisation density at the previous time step $S_{p,q}^m = S(r_p, \varphi_q, t_m)$ via spin magnetisation density at the half of the next time step $S_{p,q}^{m+\frac{1}{2}} = S(r_p, \varphi_q, t_m + \Delta t/2)$.

Assuming that the diffusion coefficient is independent on the angle ($D(r, \varphi) = D(r)$), the radial finite difference $\phi_r^2 S_{p,q}^m$ can be expressed as:

$$\phi_r^2 S_{p,q}^m = \frac{1}{\Delta r^2} \left\{ D_{p+\frac{1}{2}} \left(1 + \frac{\Delta r}{2r_p} \right) (S_{p+1,q}^m - S_{p,q}^m) + D_{p-\frac{1}{2}} \left(1 - \frac{\Delta r}{2r_p} \right) (S_{p-1,q}^m - S_{p,q}^m) \right\} \quad [3.6]$$

and for the angle finite difference $\phi_\varphi^2 S_{p,q}^m$, one obtains:

$$\phi_\varphi^2 S_{p,q}^m = \frac{D_p S_{p,q+1}^m - 2D_p S_{p,q}^m + D_p S_{p,q-1}^m}{r_p^2 \Delta \varphi^2} \quad [3.7]$$

where $D_p = D(r_p)$, and Δr and $\Delta \varphi$ are the radius and angle steps, respectively. The relaxation time $T(r, \varphi)$ is assumed to be independent of the angle φ : $T(r, \varphi) = T(r)$, $T_p = T(r_p)$.

Substituting Eqns. 3.6 and 3.7 in Eqn. 3.1 according to the numerical scheme of Eqn. 3.5 yields after some transformations two sets of tridiagonal linear algebraic equations:

$$\begin{aligned} \frac{\Delta t D_{p-\frac{1}{2}}}{2\Delta r^2} \left(1 - \frac{\Delta r}{2r_p}\right) S_{p-1,q}^{m+\frac{1}{2}} - \left\{ \frac{\Delta t D_{p+\frac{1}{2}}}{2\Delta r^2} \left(1 + \frac{\Delta r}{2r_p}\right) + \frac{\Delta t D_{p-\frac{1}{2}}}{2\Delta r^2} \left(1 - \frac{\Delta r}{2r_p}\right) + 1 + \frac{\Delta t}{2T_p} \right\} S_{p,q}^{m+\frac{1}{2}} + \frac{\Delta t D_{p+\frac{1}{2}}}{2\Delta r^2} \left(1 + \frac{\Delta r}{2r_p}\right) S_{p+1,q}^{m+\frac{1}{2}} = \\ - \frac{\Delta t D_p}{2r_r^2 \Delta \varphi^2} S_{p,q-1}^m + \left(\frac{\Delta t D_p}{r_r^2 \Delta \varphi^2} - 1 \right) S_{p,q}^m - \frac{\Delta t D_p}{2r_r^2 \Delta \varphi^2} S_{p,q+1}^m \end{aligned} \quad [3.8]$$

and:

$$\begin{aligned} \frac{\Delta t D_{p-\frac{1}{2}}}{2\Delta r^2} \left(1 - \frac{\Delta r}{2r_p}\right) S_{p-1,q}^{m+\frac{1}{2}} - \left\{ \frac{\Delta t D_{p+\frac{1}{2}}}{2\Delta r^2} \left(1 + \frac{\Delta r}{2r_p}\right) + \frac{\Delta t D_{p-\frac{1}{2}}}{2\Delta r^2} \left(1 - \frac{\Delta r}{2r_p}\right) - 1 \right\} S_{p,q}^{m+\frac{1}{2}} + \frac{\Delta t D_{p+\frac{1}{2}}}{2\Delta r^2} \left(1 + \frac{\Delta r}{2r_p}\right) S_{p+1,q}^{m+\frac{1}{2}} = \\ - \frac{\Delta t D_p}{2r_r^2 \Delta \varphi^2} S_{p,q-1}^{m+1} + \left(\frac{\Delta t D_p}{r_r^2 \Delta \varphi^2} + 1 + \frac{\Delta t}{2T_p} \right) S_{p,q}^{m+1} - \frac{\Delta t D_p}{2r_r^2 \Delta \varphi^2} S_{p,q+1}^{m+1} \end{aligned} \quad [3.9]$$

The solutions of the tridiagonal sets 3.8 and 3.9 can be obtained by the Gauss elimination method.²³ Normally, it is supposed that the diffusion coefficient D_p and the intrinsic relaxation time T_p is constant within one compartment $D_{p-\frac{1}{2}} = D_{p+\frac{1}{2}} = D_p = D(r_p) = D_j$, $T_p = T(r_p) = T_j$ when $r \in [R_{j-1}, R_j]$, $j=1, \dots, n$, and each membrane is treated as additional compartment of the length Δr with the diffusion coefficient $\rho_j \Delta r$.¹⁴

To account for the influence of magnetic field gradient pulses as used in PFG measurements, differential equation 3.1 takes the form:²⁴

$$\begin{aligned} \frac{\partial S(r, \varphi, t)}{\partial t} = \frac{\partial}{r \partial t} \left\{ r D(r, \varphi) \frac{\partial S(r, \varphi, t)}{\partial r} \right\} + \frac{\partial}{r^2 \partial \varphi} \left\{ D(r, \varphi) \frac{\partial S(r, \varphi, t)}{\partial r} \right\} + \\ \left(i\gamma g(t) r \cos(\varphi) - \frac{1}{T(r, \varphi)} \right) S(r, \varphi, t) \end{aligned} \quad [3.10]$$

where $g(t)$ describes the sequence of magnetic field gradient pulses as a function of time, and γ is the gyromagnetic ratio. In our case, $g(t)$ is a pair of magnetic field gradient pulses with the identical amplitude G , duration δ and opposite polarity; the distance between the leading edges of the gradient pulses is Δ . The gradient pulses are applied along the polar axis direction (*i.e.*, across a diameter).

The finite difference scheme can be directly applied for the numerical solution of the differential equation.²³ However, when the strength of the gradient pulses is high, the phase difference between adjacent positions can be very large and in that case it is impossible to get sufficient accuracy with reasonable values for the time and space steps. In this case it is practicable to solve linear sets 3.8 and 3.9, assuming that there are no gradient pulses, and then perform the correction for the influence of the gradient pulses, multiplying the obtained solution $S^*(r_p, \varphi_q, t_m)$ by a factor, characterising the influence of the gradient pulses:¹⁴

$$S(r_p, \varphi_q, t_m) = S^*(r_p, \varphi_q, t_m) \exp(i\gamma g(t_m) r_p \cos(\varphi_q)) \quad [3.11]$$

SOFTWARE IMPLEMENTATION

The presented two-dimensional numerical model was implemented in C++ as an extension of the one-dimensional model⁹ and inherits all advantages of that model. The time of modelling for particular two-dimensional configurations as given in Results are based on calculations on a Pentium III 550 MHz. The simulations typically yield an array of magnetisation spin density as it develops in time and space for a given value of the pulsed field gradient amplitude. Several of these arrays can be compressed into a two-dimensional data set, containing the PFG and relaxation development of the entire system. Random noise was generated during the simulations to avoid fitting problems, so that in all simulations a S/N of 10,000 was reached.

RESULTS AND DISCUSSION

COMPARISON WITH OTHER MODELS

Several computations have been performed to show the correspondence between the presented numerical model and a number of analytically solved models that were published earlier. Although spatial information is available as output of the model, all results shown here are based on the overall decay curves.

We started with a simulation of multi-exponential relaxation behaviour in the well-known Brownstein-Tarr model²⁵ for a planar and a cylindrical system, without gradient pulses. According to their theory, multi-exponential relaxation arises as a consequence of an eigenvalue problem associated with the size and shape of a cell with biologically relevant dimensions; the intensity and decay times of these exponentials can be calculated from the analytical equations. To model the Brownstein-Tarr system, we simulated a single planar or cylindrical compartment with a radius $R_1=25 \mu\text{m}$, a diffusion coefficient $D_1=2 \times 10^{-9} \text{m}^2 \text{s}^{-1}$ and an intrinsic relaxation time of 2 s. The relative permeability $M = \rho_1 R_1 / D_1$ of the boundaries was varied between $M = 0.001$ and $M = 1000$. The data were fitted with SPLMOD,²⁶ using five discrete exponentials, of which the largest three are plotted in Figure 3.2 (symbols). Modelling using 3000 time steps, 500 space steps and 90 angle steps took approximately 12 minutes. The results show an excellent agreement between the Brownstein-Tarr theory (lines) and our first exponential (I_0, T_0). The second and third components correspond well to the theory for higher intensities. For very low intensities of these components ($M < 0.5$), the relaxation times show some deviations due to fitting errors.

The results of the PFG part of the simulations were verified by comparing them with the Callaghan model,¹⁹ which describes spin behaviour within a confined compartment with closed or permeable boundaries. This model uses a narrow pulse approximation, which was

approached by using a very short gradient pulse ($\delta = 0.1$ ms) with a high gradient strength. The simulated system was again a single compartment with a closed or partially permeable boundary ($D_1 = 2 \times 10^{-9} \text{ m}^2 \text{ s}^{-1}$, $R_1 = 20 \text{ }\mu\text{m}$ and $\rho_l = 0$ or $\rho_l = 2R_1/D_1$). Relaxation was eliminated by defining infinitely large intrinsic T_2 values. Echo attenuation plots obtained by the Callaghan model (solid line) and the present one (symbols) are shown in Fig. 3.3, for planar (A, B) and cylindrical geometries (C, D) and open (A, C) or closed boundaries (B, D). The echo attenuation is plotted as a function of $(2\pi)^{-1}\gamma g \delta \cdot R_1$. Expressed in multiples of R_1^2/D_1 , the observation time Δ is respectively 0.2, 0.5, 1.0 or 2.0. The results clearly show that our model corresponds excellently to the Callaghan model. Calculation time was 9 minutes when using 64 gradient steps, 400 space steps and 36 angle steps.

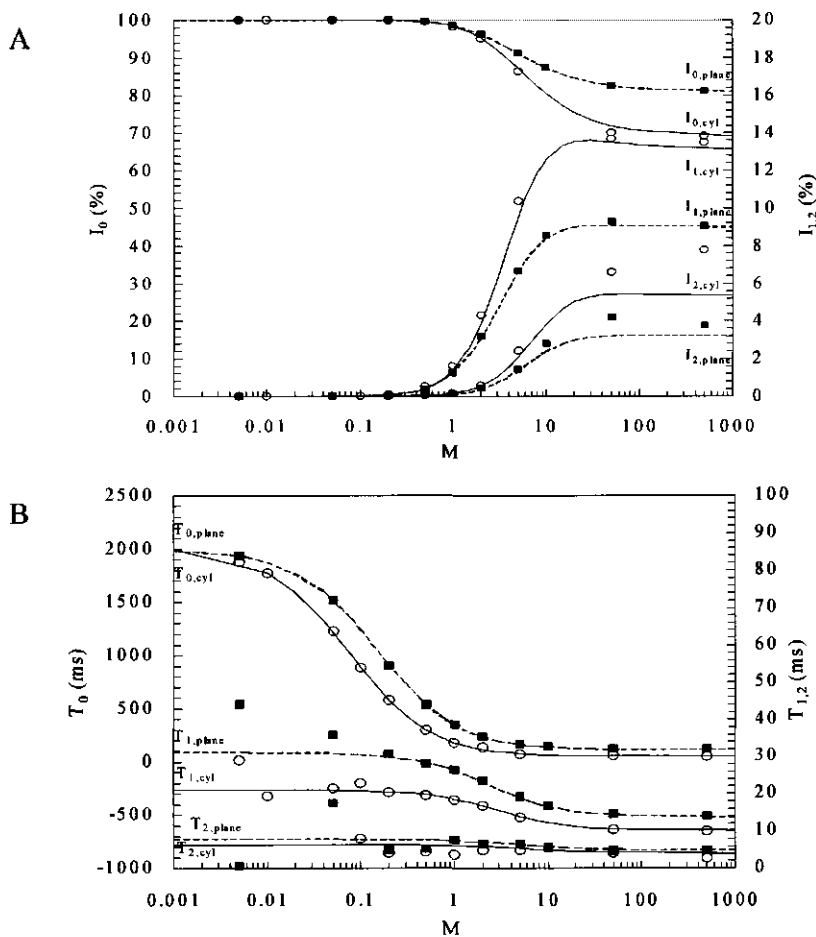


Figure 3.2. A. Relative intensity of the first three modes of relaxation as a function of the relative membrane permeability $M = \rho_l R_1 / D_1$. The Brownstein-Tarr results are depicted as lines (striped for the planar and solid for the cylindrical geometry), whereas our results are plotted with square symbols for the planar geometry, and open circles for the cylindrical geometry. Note the change of scale for the I_1 and I_2 curves. B. Decay time of the first three modes of relaxation.

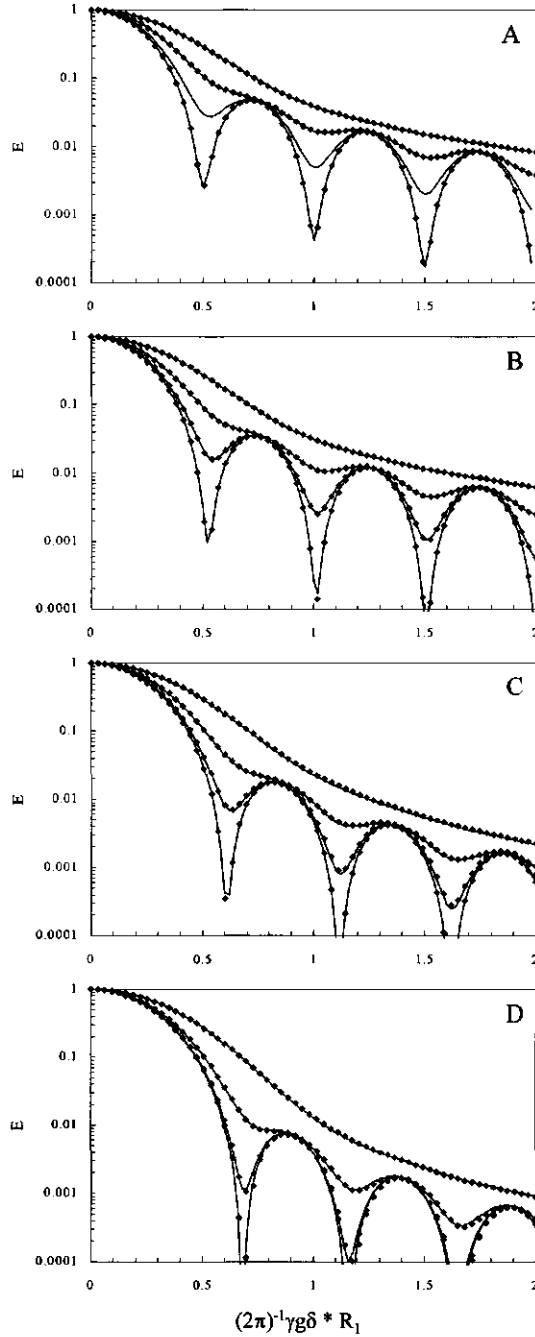


Figure 3.3. Signal attenuation plots of the Callaghan model (lines) and the present model (symbols) for a one-compartment system Expressed in multiples of R_1^2/D_1 , the observation time Δ is respectively 0.2, 0.5, 1.0 or 2.0 from bottom to top. A. Planar geometry and fully reflective membranes. B. Planar geometry and partially permeable membranes ($\rho_1 R_1 / D_1 = 2$). C. Cylindrical geometry and fully reflective membranes. D. Cylindrical geometry and partially permeable membranes ($\rho_1 R_1 / D_1 = 2$).

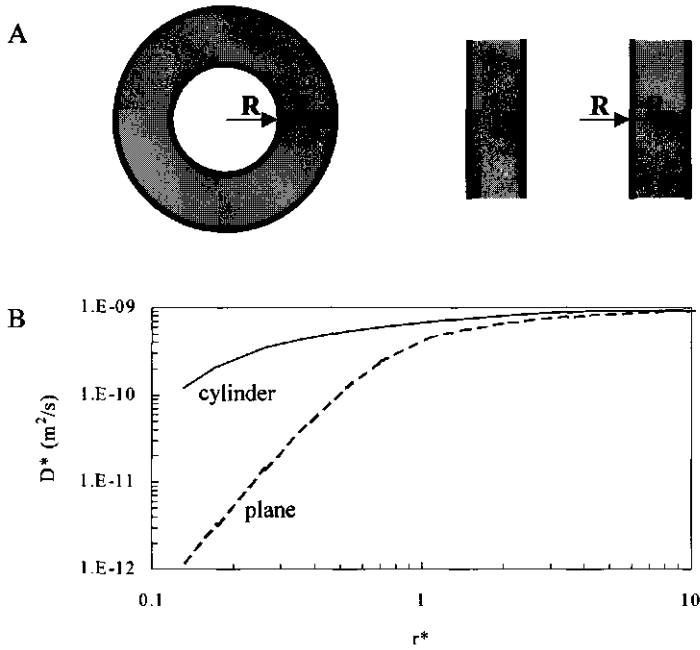


Figure 3.4. A. Cylindrical and planar geometries of the examined system. B. Apparent diffusion coefficient D^* as a function of the relative length of the outer compartment r^* for cylindrical (solid line) and planar (dashed line) geometries (membranes are fully reflecting).

EFFECT OF CYLINDRICAL GEOMETRY

Molecular motion within multi-compartment systems (Fig. 3.4A) as (plant) cells or porous media will not only depend on the radius of these compartments, but in the cylindrical case also on the probability to circumvent a diffusion barrier by two-dimensional diffusion. Hence, it is useful to have an understanding of the impact of the geometry on the diffusion and relaxation properties of the system. Therefore, restricted diffusion in a two-dimensional model consisting of concentric cylinders is compared with a one-dimensional system consisting of plan parallel barriers. The simulation of the echo attenuation was done in 16 PFG steps, a typical number for an experimental experiment.

First, we compared two systems with cylindrical and planar geometries as shown in Fig. 3.4A. Both of them consist of two compartments with fully reflective walls. The inner compartment contains no initial magnetisation. The diffusion coefficient of the outer compartment is $D_2 = 1 \times 10^{-9} \text{ m}^2 \text{ s}^{-1}$ and its width $R_1 = R_2$, where R_1 is the radius of the inner compartment. For the moment it was assumed that no relaxation occurred in either compartment. The resulting data set was fitted with a single exponential. The dependence of the apparent diffusion coefficient D^* in the planar and cylindrical configurations on the

relative length of the outer compartment $r^* = R_2 / (2\sqrt{2D_2(\Delta - \delta/3)})$ is presented in Fig. 3.4B for $\Delta = 18$ ms and $\delta = 5$ ms. It is clear that especially for small values of r^* , the cylindrical configuration provides a less restricted geometry for diffusion than the planar one. The reason for this is that spin-bearing molecules can freely move along the angle axis, and the maximum displacement is only determined by the outer wall at an effective radius $2R_2$. When the relative length r^* increases and diffusion in planar compartment becomes less restricted, the difference between the apparent diffusion coefficients for both geometries gradually disappears and D^* approaches the intrinsic diffusion coefficient.

When the internal membranes of these two-compartment systems become semi-permeable, the properties of the 'empty' compartment start to play a role as well. We simulated the configurations where either the inner compartment (Fig. 3.5A(I)) or the outer compartment (Fig. 3.5A(II)) contains magnetisation. For both configurations the ratio r^* equals 1.05, with $R_1 = R_2 = 12$ μm . The diffusion coefficients are for the inner compartment $D_1 = 2 \times 10^{-9}$ $\text{m}^2 \text{s}^{-1}$, and for the outer compartment $D_2 = 1 \times 10^{-9}$ $\text{m}^2 \text{s}^{-1}$. All these values are reasonable for a plant cell. In Figure 3.5B, the dependencies of the apparent diffusion coefficient D^* on the relative membrane permeability M are shown, for the planar (dashed line) and cylindrical (solid line) geometry. When the outer compartment contains magnetisation, an increase in relative permeability causes an increase of both apparent diffusion coefficients, though for the planar case this phenomenon is more pronounced. This is because the restriction effects are stronger in the planar system when M is small, as was already shown in Figure 3.4B. When the inner membrane becomes more permeable, the differences between the two systems almost disappear.

For the second configuration (Fig. 3.5A(II)), the parameters remain the same, only now the inner compartment contains magnetisation. In this case the apparent diffusion coefficient D^* increases for both cylindrical and planar geometries (Fig. 3.5B), but the plateau value for high M is lower for the cylindrical geometry. In this case complete exchange between the two compartments occurs, resulting in a lower D^* for the cylinder due to the larger volume of the outer compartment.

In experimental multi-compartment geometries, as for example plant cells, usually all spins are excited, so all compartments contain magnetisation. Such a system is the superposition of the two configurations examined above (Fig. 3.6A). Now clearly the resulting diffusion attenuation decay shows multi-exponential behaviour. Hence, a bi-exponential fit was used to analyse the data.¹³ It should be mentioned that a comparison of cylindrical and planar geometries for such a system is not absolutely correct, because the contribution of the magnetisation from each compartment to the whole magnetisation is not identical for different geometries, *i.e.* the ratio of the contributions from the outer and inner compartments equals 1 in the planar case and 3 in the cylindrical case.

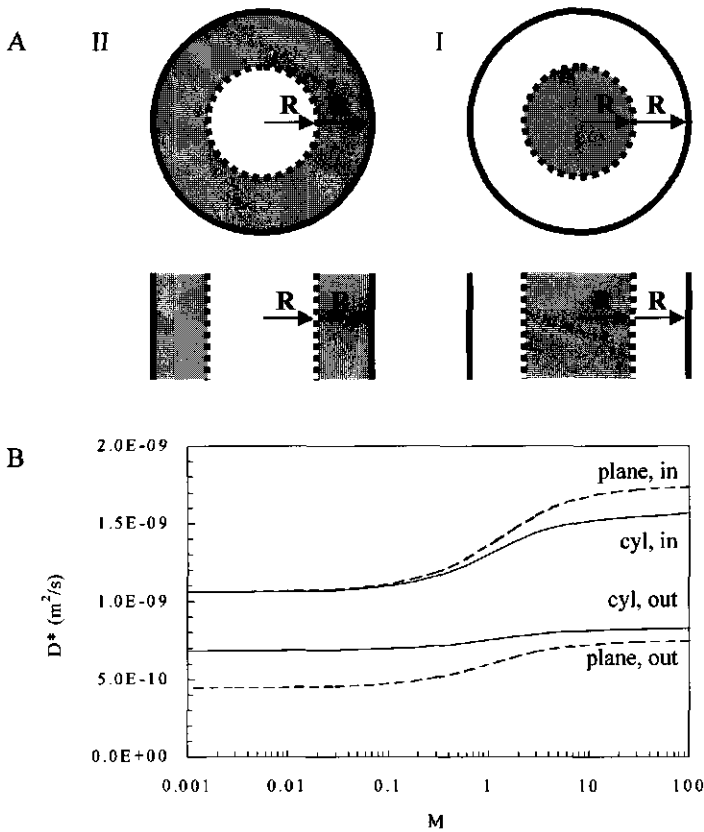


Figure 3.5. A. Cylindrical and planar geometries of two examined systems B. Apparent diffusion coefficient D^* as a function of the relative membrane permeability M for cylindrical (solid line) and planar (dashed line) geometries. The subscripts 'in' and 'out' are used to distinguish the inner and outer compartment respectively.

For a closed membrane ($M=0$) the two fitted components for the combined system should correspond to the separate apparent diffusion coefficients in Fig. 3.5B. As one can see from Figs. 3.6B and 3.6C, neither the diffusion coefficients nor the amplitude of these components agree to what is expected from Fig. 3.5B. The reason is that the diffusion attenuation is not strictly bi-exponential, but multi-exponential, as the diffusion behaviour of the spins is not the same for all positions within the compartments. Therefore, the results in Fig. 3.6 correspond to the best fit of the diffusion attenuation, but the values no longer correspond to the true intensities and apparent diffusion coefficients in the system. The consequence for experimental data is that multi-exponential analysis of diffusion behaviour can not freely be related to the geometrical parameters of the system.

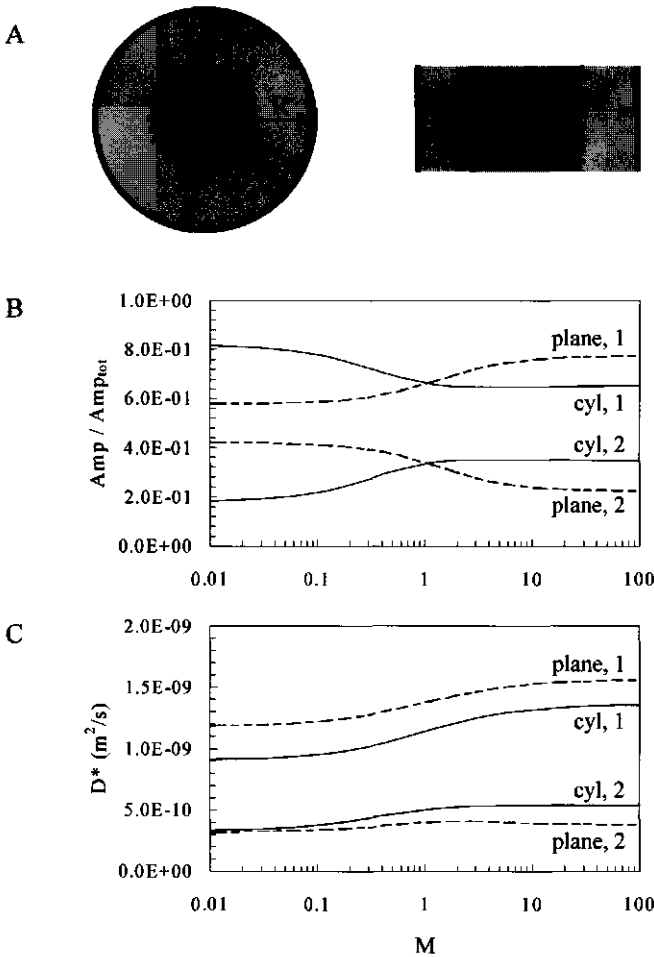


Figure 3.6. A. Cylindrical and planar geometries of the examined system B. Amplitude of the fractions divided by the input value as a function of the relative membrane permeability M for cylindrical (solid line) and planar (dashed line). C. Apparent diffusion coefficient D^* as a function of the relative membrane permeability M for cylindrical (solid line) and planar (dashed line) geometries.

Experimentally, additional parameters as T_2 can be used to provide extra contrast to extract physiologically relevant parameters.¹³ This was simulated for these two-compartment systems by introducing an intrinsic relaxation time of 2 s for the inner compartment, and 0.2 s for the outer one, which are reasonable values for a plant cell.² The parameters for these simulations were chosen as in an experimental PFG-CPMG experiment (DARTS),¹³ i.e. a PFG part of 16 gradient steps, combined with an echo train of 1000 echoes with an inter-echo time of 5 ms. Calculations took 15 minutes for 120 space steps, 36 angle steps, 16 gradient steps and 1000 time steps. The resulting two-dimensional data sets were fitted with a coupled fitting routine; first a bi-exponential fit was done on the relaxation part with SPLMOD, and next the fitted intensities were used to fit the corresponding diffusion fractions.

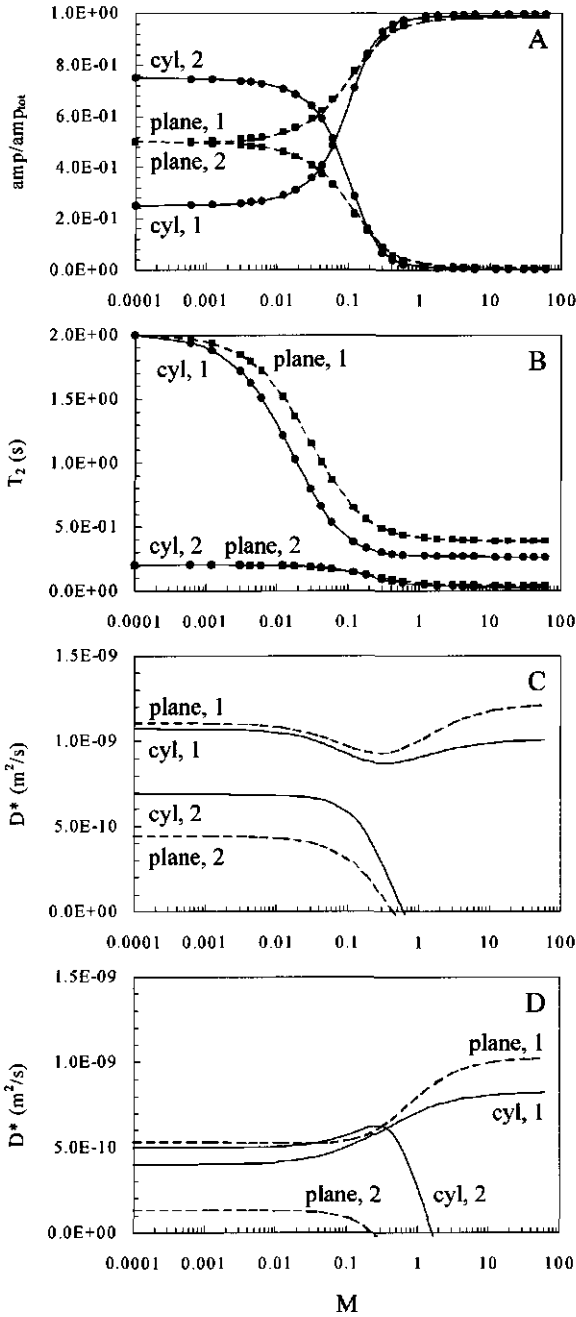


Figure 3.7. The same system was used as in Figure 3.6, but with relaxation behaviour. **A.** Amplitude of the fractions divided by the input value as a function of the relative membrane permeability M for cylindrical (solid line) and planar (dashed line) for simulations with an diffusion observation time $\Delta = 18$ ms. The results for the simulations with $\Delta = 90$ ms are overplotted with symbols (squares for the planar geometry, and circles for the cylindrical geometry). **B.** Relaxation time of the fractions. Linestyles and symbols correspond to those in Fig. 3.7A. **C.** Apparent diffusion coefficient D^* for an observation time Δ of 18 ms. **D.** Apparent diffusion coefficient D^* for an observation time Δ of 90 ms.

For very small M values, the fractions of the two components and the corresponding T_2 are equal to the input parameters ($T_2 = 2$ s and 0.2 s; amplitude = 1:1 for the planar and 1:3 for the cylindrical case) and D^* corresponds to the diffusion coefficients for the separated systems in Fig. 3.5 (lines in Figs. 3.7A, B, C), in contrast to those in Fig. 3.6. This clearly shows that the use of T_2 information is advantageous for discriminating different fractions in a multi-compartment system. When the membrane permeability increased, the relaxation behaviour evolved to an almost mono-exponential decay, due to complete averaging of the two compartments. The corresponding diffusion coefficients first decrease due to averaging of the two fractions, but start to increase as soon as the relaxation decay becomes mono-exponential, and, as expected, the increase is more pronounced for planar geometries. It should be noted that though a multi-parameter approach is useful to discriminate compartments separated by a membrane, the fitted parameters amplitude, T_2 and D^* , are no longer uniquely reflecting the properties of the different compartments when the membrane becomes reasonably permeable ($M > 0.01$). For instance the value of the longest T_2 component, originating from the central compartment of the model, becomes strongly dependent on those of the second compartment and the actual membrane permeability.

Fig. 3.7D shows the effect of a longer observation time Δ (90 ms). The amplitude and T_2 yield exactly the same results as those for $\Delta = 18$ ms (symbols in Figs. 3.7A,B). The restriction effects on D^* on the contrary, become much more pronounced. For small M , all values are decreased, though only slightly in the cylindrical outer compartment (solid line). This is a prominent illustration of the effect of circumventional motion to overcome diffusion restriction, and for $M < 1$ such data sets with varying observation time Δ can be very useful for discrimination between planar and cylindrical geometries.

CONCLUSIONS

A numerical model for diffusion and magnetisation relaxation behaviour in PFG-CPMG NMR experiments has been extended to a two-dimensional system with concentric cylindrical geometry. The results of this model show excellent agreement with published analytical results. As an example of the relevance of a two-dimensional model, the behaviour of the apparent diffusion coefficients and relaxation times in a multi-compartment system with the properties of a plant cell has been modelled for both a planar and a cylindrical geometry. When the difference in diffusion coefficients is relatively small, supplementary contrast parameters as T_2 are needed to unravel the different fractions present. The difference between the obtained values of the apparent diffusion coefficients and the true ones can be explained by the influence of non- or semi-permeable membranes (restricted diffusion). This restriction effect is more pronounced for planar systems than for cylindrical ones. Furthermore, the

differences in diffusion coefficients between the two geometries become larger for longer observation times. Together, this clearly demonstrates the need for a two-dimensional system to be able to understand experimental results in term of geometry.

ACKNOWLEDGEMENTS

This Chapter has been published as:

Van der Weerd L., Melnikov S.M., Vergeldt F.J., Novikov E.G. & Van As H. (2001) Modelling of self-diffusion and relaxation time NMR in multi-compartment systems with cylindrical geometry. *Journal of Magnetic Resonance* **156**, 213-221.

REFERENCES

1. Fenrich F.R.E., Beaulieu C. & Allen P.S. (2001) Relaxation times and microstructures. *NMR in Biomedicine* **14**, 133-139.
2. Snaar J.E.M. & Van As H. (1992) Probing water compartment and membrane permeability in plant cells by proton NMR relaxation measurements. *Biophysical Journal* **63**, 1654-1658.
3. Song Y.Q., Ryu S. & Sen P.N. (2000) Determining multiple length scales in rocks. *Nature* **406**, 178-181.
4. Van As H. & Van Dusschoten D. (1997) NMR methods for imaging of transport processes in micro-porous systems. *Geoderma* **80**, 389-403.
5. Van Dusschoten D., Moonen C.T., De Jager P.A. & Van As H. (1996) Unraveling diffusion constants in biological tissue by combining Carr-Purcell-Meiboom-Gill imaging and pulsed field gradient NMR. *Magnetic Resonance in Medicine* **36**, 907-913.
6. Hills B.P. & Snaar J.E.M. (1992) Dynamic q space microscopy of cellular tissue. *Molecular Physics* **76**, 979-994.
7. Kuchel P.W. & Durrant C.J. (1999) Permeability coefficients from NMR q-space data: Models with unevenly spaced semi-permeable parallel membranes. *Journal of Magnetic Resonance* **139**, 258-272.
8. Mitra P.P. & Sen P.N. (1992) Effects of microgeometry and surface relaxation on NMR pulsed-field-gradient experiments: simple pore geometries. *Physical Review B* **45**, 143-156.
9. Novikov E.G., van Dusschoten D. & Van As H. (1998) Modeling of self-diffusion and relaxation time NMR in multi-compartment systems. *Journal of Magnetic Resonance* **135**, 522-528.
10. Pfeuffer J., Flögel U., Dreher W. & Leibfritz D. (1998) Restricted diffusion and exchange of intracellular water: theoretical modelling and diffusion time dependence of H-1 NMR measurements on perfused glial cells. *NMR In Biomedicine* **11**, 19-31.
11. Snaar J.E.M. & Van As H. (1993) NMR self-diffusion measurements in a bounded system with loss of magnetization at the walls. *Journal of Magnetic Resonance A* **102**, 318-326.

12. Stanisz G.J., Li J.G., Wright G.A. & Henkelman R.M. (1998) Water dynamics in human blood via combined measurements of T-2 relaxation and diffusion in the presence of gadolinium. *Magnetic Resonance in Medicine* **39**, 223-233.
13. Van Dusschoten D., De Jager P.A. & Van As H. (1995) Extracting diffusion constants from echo-time-dependent PFG NMR data using relaxation-time information. *Journal of Magnetic Resonance A* **116**, 22-28.
14. Zawodzinski T.A., Springer T.E., Neeman M. & Sillerud L.O. (1992) Diffusion barriers in pulsed-gradient spin-echo NMR microscopy. *Israel Journal of Chemistry* **32**, 281-289.
15. Stanisz G.J. & Henkelman R.M. (1998) Diffusional anisotropy of T-2 components in bovine optic nerve. *Magnetic Resonance Medicine* **40**.
16. Traore A., Foucat L. & Renou J.P. (2000) H-1-NMR study of water dynamics in hydrated collagen: Transverse relaxation-time and diffusion analysis. *Biopolymers* **53**, 476-483.
17. Schoberth S.M., Bar N.K., Kramer R. & Karger J. (2000) Pulsed high-field gradient in vivo NMR spectroscopy to measure diffusional water permeability in *Corynebacterium glutamicum*. *Analytical Biochemistry* **279**, 100-105.
18. Does M.D. & Gore J.C. (2000) Compartmental study of diffusion and relaxation measured in vivo in normal and ischemic rat brain and trigeminal nerve. *Magnetic Resonance in Medicine* **43**, 837-844.
19. Callaghan P.T. (1995) Pulsed-gradient spin-echo NMR for planar, cylindrical, and spherical pores under conditions of wall relaxation. *Journal of Magnetic Resonance A* **113**, 53-59.
20. Gudbjartsson H. & Patz S. (1995) NMR diffusion simulation based on conditional random walk. *IEEE Transactions on Medical Imaging* **14**, 636-642.
21. Linse P. & Söderman O. (1995) The validity of the short-gradient-pulse approximation in NMR studies of restricted diffusion. Simulations of molecules diffusing between planes, in cylinders and spheres. *Journal of Magnetic Resonance A* **116**, 77-86.
22. Crank J. (1975) *The mathematics of diffusion*. Oxford, Oxford University Press.
23. Meis T. & Marcowitz U. (1981) *Numerical solutions of partial differential equations*. New York, Springer Verlag.
24. Callaghan P.T. (1993) *Principles of nuclear magnetic resonance microscopy*. Oxford, Clarendon Press.
25. Brownstein K.R. & Tarr C.E. (1979) Importance of classical diffusion in NMR studies of water in biological cells. *Physical Review A* **19**, 2446-2453.
26. Provencher S.W. & Vogel R.H. (1983) Regularization techniques for inverse problems in molecular biology. In: *Numerical treatment of inverse problems in differential and integral equations* (eds. Deuffhard P. & Hairer E.), 304-319. Birkhauser, Boston.

4

SIMULATION OF RELAXATION, DIFFUSION AND EXCHANGE IN MULTI-COMPARTMENT SYSTEMS

A finite difference model has been applied to investigate the effects of diffusive exchange on the transverse spin relaxation times, apparent diffusion coefficients and the NMR signal amplitudes of water in multi-compartment systems, in particular biological cells. For different multi-compartment model systems a PFG-CPMG experiment was simulated, and intrinsic physiological parameters such as the bulk diffusion constant, the cell radius and the membrane permeability were afterwards extracted using common theoretical models. The true membrane permeability values are compared with those calculated using the relaxation models of Conlon-Outhred and Brownstein-Tarr. Generally, the Brownstein-Tarr formalism turns out to predict the true permeability more reliably.

The effect of the bulk spin relaxation and the diffusion properties of water in the different compartments on the observed T_2 and D_{app} is discussed for several systems that do not completely satisfy the requirements of the ideal relaxation models, as is the case for most biological systems. Furthermore, the effect of these unfulfilled conditions on the calculated intrinsic parameters as the membrane permeability and the cell radius are evaluated.

Finally, the effect of cell-to-cell transport on the long-term diffusion behaviour is assessed.

INTRODUCTION

^1H NMR relaxometry and diffusometry are commonly used to investigate the physical properties of water in biological tissues.¹⁻⁴ Most of these studies attempt to assign the experimentally observed diffusion or relaxation components to different (sub-)cellular compartments within such tissue. From these parameters one can extract valuable information on the diffusion constant in the compartments, the (relative) water fractions, the compartment dimensions, and the water membrane permeability of the membranes separating the compartments.

Chemical exchange of protons between water and macromolecules may significantly contribute to the longitudinal relaxation time (T_1) and the transversal relaxation time (T_2) of bulk water in the cells. This results in different relaxation times for the various compartments, which we call the intrinsic or bulk relaxation times.^{5,6} In addition, water or protons may exchange through semi-permeable membranes between compartments with different intrinsic relaxation times. This process results in averaging of the relaxation times and water fractions,⁵ which hampers a direct assignment of relaxation times and fractions to particular compart-

ments. The extent of the averaging depends on the difference between the intrinsic relaxation rates of the compartments and on the exchange rates between them. The latter are determined by the permeabilities of the membranes separating the compartments, and by the diffusion path length of water to the membrane. This path length depends on the dimensions of the compartments and the diffusion coefficient of the fluid. By accounting for all the above mentioned effects, relaxometry of biological systems with a rather simple geometry can provide valuable physiological information such as the membrane permeabilities and the cell dimensions.⁶⁻¹⁰

Diffusion measurements of biological tissue can also reflect multiple subcompartments, each with a characteristic diffusion coefficient and relaxation time.¹¹⁻¹³ At very short diffusion times, separate fractions can often be discriminated based on the different bulk diffusion coefficients. For longer diffusion times, however, restriction of diffusion by inter-compartmental membranes is going to dominate the diffusion attenuation, which will then reflect the compartment dimensions. For a better understanding of the cellular physiology, both the diffusion coefficient of the cellular water and the compartment dimensions yield very valuable information.¹⁴ In addition to the cell dimensions, diffusive exchange and differences in relaxation in the compartments will also influence the apparent diffusion coefficients (D_{app}).^{13,15,16}

In general, the differences in T_2 relaxation times between the compartments are larger than those in diffusion coefficients. Experimentally, Diffusion Analysis by Relaxation Time Separation, DARTS,^{11,17} has been proven to result in a better parameter determination compared to separate diffusion and relaxation experiments.¹⁸⁻²² Taking nerve tissue as an example, measurements limited to either diffusion- or spin relaxation result in completely different interpretations of the subcompartments present in the tissue. Generally, diffusion measurements yield mono-exponential decay curves that yield no information on the number or nature of the sub-compartments.²³ Sometimes, under conditions of high diffusion weighting, large deviations from mono-exponential behaviour occur due to restricted diffusion. However, a multi-exponential fit of the NMR diffusion attenuation plot does not reflect the sub-compartments.^{13,24} Relaxation decays of the same tissue yield three different components, which are attributed to inter-axonal, axonal and myelin domains. Using these T_2 components, the diffusion attenuation can be resolved yielding the apparent diffusion coefficients (D_{app}) for the different compartments.^{11,25}

Clearly, exchange of water between these compartments and/or diffusive restriction within these structures may easily complicate such assignment. Therefore, a model that combines diffusion and relaxation behaviour in combination with membrane permeabilities could be of great help to interpret the experimental results. Numerous theories and models have been developed to interpret the NMR results for heterogeneous biological tissues such as occur in blood, nerves, brain, and plants. Usually, these models explain the results in terms of internal

and external water fractions and cell size^{4,26-29} and the exchange of water between compartments.^{1,2,22,30} Most of the models for the interpretation of diffusometry do not include the effect of (differences in) relaxation behaviour in the compartments, although this effect can not be ignored.^{15,31}

Clearly, an unambiguous interpretation of experimental non-exponential decay curves in terms of water fractions for every compartment and exchange rates between them is far from straightforward. Therefore the effects of diffusive exchange on the observed relaxation times, diffusion coefficients and fractional amplitudes have been modelled numerically using a two-dimensional finite difference solution of Fick's second law of diffusion.³¹ We used simple models of (i) an isolated cylindrical compartment with a perfect extracellular sink and (ii) the same isolated cylindrical compartment, with a partial extracellular sink. Next (iii) an isolated plant cell was modelled, consisting of three concentric cylindrical compartments, *i.e.* the vacuole, the cytoplasm and the cell wall / extracellular space, separated by permeable membranes. Furthermore, a simple one-dimensional model of parallel planes¹⁵ was used to simulate the effect of cell-to-cell transport (iv). We used a broad range of membrane permeabilities (P) to evaluate their effect on the relaxation time and diffusion behaviour. All chosen input parameters for the different compartments complied with experimentally realistic values.

For all model systems, we extracted the physiological parameters of interest, *i.e.* the membrane permeability, the compartment size and the bulk diffusion coefficients by an analysis based on common theoretical models, and we compared these parameters with the input values of the model. Thus we evaluated whether these theories are useful for such complicated biological systems, even when these systems do not meet all conditions of the theories.

THEORY

RELAXATION THEORY

The origin of multi-exponential relaxation is generally accepted to be mainly due to a spatial compartmentation of water in spaces with different relaxation and diffusion properties. Exchange between these compartments causes a change in the relaxation properties of the observed magnetization in these spaces. In some specific cases these changes can be used to calculate the membrane permeability for water (P , m s^{-1}).^{6-8,32} However, the results depend on the used NMR method. The NMR technique to measure P was introduced for the first time already three decades ago by Conlon and Outhred.⁷

This C-O technique is valid when the spin relaxation outside the cell compartment under consideration is much faster than the exchange over the membrane, so that back flux of magnetisation to the cell can be ignored. Experimentally this condition is fulfilled by doping

the extracellular space with paramagnetic ions such as manganese. The observed intracellular relaxation rate $1/T_{2,obs}$ is then given by

$$1/T_{2,obs} = 1/T_{2,bulk} + 1/\tau \quad [4.1]$$

where τ^{-1} is the exchange rate of intracellular water across the membrane; $T_{2,bulk}$ is the intrinsic T_2 of the cell. The (effective) exchange rate across the membrane depends on the surface-to-volume ratio of the compartment and on the effectiveness of magnetisation loss due to exchange with the external volume sink (H_{CO}).

$$1/\tau = (SH_{CO})/V \quad [4.2]$$

where V and S are the volume and surface of the cell respectively. For a cylindrical cell with radius r , $H_{CO} = r/2\tau$. If the extracellular magnetisation sink is perfect and the membrane permeability determines the exchange rate, H_{CO} equals the true membrane permeability P .

Brownstein and Tarr developed a more advanced model to calculate the surface sink strength from the diffusivity and relaxation time of bulk water by incorporating the geometry of the compartments.⁸ Similar to the C-O model, back flux of magnetisation to the cell should be negligible to fit the assumptions of the Brownstein-Tarr (B-T) model. Brownstein and Tarr assume that all relaxation is due to magnetisation sinks within an active surface, which is reached by diffusion. The net rate of magnetisation loss at the boundary is then defined by a sink strength parameter, denoted H_{BT} ($m\ s^{-1}$), to be distinguished from H_{CO} as calculated by Conlon and Outhred. In many biological systems, it is assumed that the membrane itself does not act as the most important relaxation sink, but that magnetisation loss occurs primarily due to a volume sink outside the compartment that can be reached by exchange over the membrane. For a plant cell, for example, the cytoplasm acts as a magnetisation sink for the vacuole due to its much shorter relaxation time, and the exchange rate between vacuole and cytoplasm is determined by the membrane permeability. The overall sink strength is then determined by a combination of the membrane permeability and the effectiveness of the volume sink.

In addition to the relaxation at the boundary, there is also relaxation due to the active volume itself, the intrinsic relaxation of the bulk solution. For a cylindrical cell, surrounded by a membrane with a constant sink strength over the entire surface, the B-T model results in a multiexponential relaxation decay, composed of a number of decay times $T_{2,m}$ ^{8,33} given by:

$$1/T_{2,m} = \eta_m^2 D_{vac} / r_{vac}^2 + 1/T_{2,vac} \quad [4.3]$$

with relative intensities

$$I_m = 4J_1^2(\eta_m) / \eta_m^2 [J_0^2(\eta_m) + J_1^2(\eta_m)] \quad [4.4]$$

H_{BT} is determined by the positive root η_m ($m = 0, 1, 2, \dots$) of $\eta_m J_1(\eta_m)/J_0(\eta_m) = H_{BT}/D_{vac}$ and J_0 and J_1 are Bessel functions of the zero and first order, respectively. All relaxation components η_m , and the corresponding intensities I_m can be determined from Eqns. 4.3 and 4.4. When the membrane permeability P is the rate-limiting step ($rP/D < 1$), the intensity of the higher relaxation modes can be neglected (Eqn. 4.4) and the relaxation decay becomes mono-exponential. Since $\eta^2 = 2rH_{BT}/D$ for $\eta \ll 1$ and $1/\tau = D\eta^2/r^2$, H_{BT} becomes $r/2\tau$ and thus equals P . The condition $rH_{BT}/D < 1$ implies $\eta < 0.4\pi$ and $\tau_a > r^2/1.58D$. H_{BT} becomes smaller than P as soon as the surface relaxation is no longer the rate-limiting step, or the membrane permeability no longer controls the water-exchange time.

DIFFUSION THEORY

Biological tissues are characterised by multiple barriers between compartments that can hinder Brownian motion. For a cylindrical cell, the motion of water molecules in a closed cylindrical cell is restricted by the membrane, and therefore the maximum displacement depends on the cell dimensions.^{13,24,34} With increasing diffusion time, the apparent diffusion coefficient (D_{app}) decreases due to the restricted displacement. On a time scale long compared to the time necessary to diffuse a distance r ($\Delta \gg r^2/2D_0$), the diffusion attenuation $E(\Delta)$ remains constant despite of an increasing diffusion time.^{13,19,34,35}

$$E(\Delta) = \exp\left[-(2\pi q)^2 \Delta D_{app}\right] \quad [4.5]$$

where $D_{app} \approx r^2/4\Delta$. The wave vector $q = \gamma g \delta / 2\pi$ in Eqn. 4.5 is a function of the gradient amplitude g , the pulse duration δ and the gyromagnetic ratio γ . This implies that from a diffusion measurement at long time scale, the compartment radius can be calculated. D_{app} should be determined from the initial slope of the diffusion attenuation plot, since at long diffusion times the diffusion profile is no longer Gaussian due to restriction effects.^{33,36}

If the cell is not closed, but has a (partially) permeable membrane, the effective diffusion distance is going to deviate from the cell radius, but to which extent depends on the extracellular parameters.

On a short diffusion time scale ($\Delta \ll r^2/2D_0$), only spins within a diffusion length $\sqrt{2D_0\Delta}$ from the wall sense the presence of the compartment boundary. Therefore the apparent diffusion coefficient D_{app} shows a dependence on $\sqrt{\Delta}$.³⁷⁻³⁹ For a single cylindrical compartment this relation can approximately be described by:

$$D_{app}(\Delta) = D_{bulk} \left[1 - (4/3r) \sqrt{D_{bulk} \Delta / \pi} \right] \quad [4.6]$$

By extrapolation to $\Delta = 0$, the bulk diffusion coefficient D_{bulk} can be determined.

METHODS

A numerical model of multi-compartment systems with cylindrical geometry was used that was based on a numerical finite difference solution of Fick's second law of diffusion.³¹ Using this model, the NMR signal amplitude and phase can be calculated for any combination of intrinsic compartment parameters at any given time during the gradient pulses and diffusion time and during the decay time following the PFG part of a PFG-CPMG experiment. Random noise (S/N 10000) was generated to avoid fitting problems. The statistical error of the parameters was determined by generating several data sets with synthetic noise and applying statistics on the fit results (Monte Carlo simulation).

For all presented cases, a typical PFG-CPMG experiment was simulated, with 16 gradient steps and 500-2000 echoes at a 5 ms interecho time. The resulting two-dimensional data sets were analysed according the DARTS method.^{11,17} A coupled fitting routine was used, first a multi-exponential fit was done on the relaxation part with SPLMOD,^{11,17,40} and next the fitted intensities were used to fit the corresponding diffusion fractions. The overall value of D_{app} was calculated from the initial slope of the diffusion attenuation plot.³³

RESULTS AND DISCUSSION

A series of geometries with increasing complexity was modelled to evaluate the discussed theoretical approaches to extract intrinsic parameters for a biological cell system. The model was inspired by plant cells, but the conclusions apply to any biological, multi-compartment system.

SINGLE COMPARTMENT WITH A PERFECT EXTRACELLULAR VOLUME SINK (i)

To compare the B-T and C-O models, a single cylindrical compartment was simulated, with a radius of 20 μm and a bulk relaxation time of 2 s. The extracellular space was assumed to have an infinitely short relaxation decay time, as would be the case for a Mn-doped extracellular solution. The bulk diffusion constant for both compartments was $2 \times 10^{-9} \text{ m}^2 \text{ s}^{-1}$, close to that of free water. The membrane permeability was varied between 0 and $2 \times 10^{-2} \text{ m s}^{-1}$, to cover the entire range from the fast ($rP/D \ll 1$) to the slow diffusion regime ($rP/D \gg 1$).

The obtained relaxation curves were fitted either mono- or bi-exponentially (Fig. 4.1A). The resulting T_2 values were used to calculate H_{CO} and H_{BT} from Eqns. 4.1 and 4.3 respectively (Fig. 4.1B). For a bi-exponential fit, the longest T_2 component corresponds to the zero order relaxation time $T_{2,0}$. Though a multi-exponential fit is the most correct approach for the B-T model, the contribution of the higher order decays is usually so small that an extremely high S/N ratio is needed to distinguish them. Therefore, a mono-exponential fit was evaluated as well. For the fast diffusion regime ($rP/D < 1$), both models yielded a sink strength equal to the membrane permeability P . In the intermediate and the slow diffusion regime however, H_{CO} is

significantly lower than P . For $rP/D > 10$, the H_{CO} sink strength even becomes independent of the actual input permeability and levels off to a value $\pi^2 D/2r$ while now $1/\tau_a$ is given by $\pi^2 D/r^2$. For these regimes, the B-T model offers a more reliable approach. The B-T model predicts multi-exponential behaviour for the slow diffusion regime, which is why the obtained H_{BT} is most accurate using a bi-exponential fit.

However, in experimental situations there will be some practical problems with the B-T approach. Firstly, for these large values of rP/D the solutions for the Bessel functions in Eqn. 4.4 are very sensitive for the input relaxation time; comparison of Fig. 4.1A and 4.1B shows that though the difference in the mono-exponential T_2 and the longest T_2 component of the bi-exponential fit is only about 2%, the difference in the calculated H_{BT} is as large as 85%. Therefore, the obtained sink strengths for $rP/D > 10$ will be very inaccurate in an experimental situation where the error of the experiments can easily be above 1%. Secondly, the B-T model requires values for both the compartment radius and the bulk diffusion coefficient, whereas the C-O model only requires the radius. Therefore, additional diffusion measurements for both short and long diffusion time scales are needed to determine these parameters.

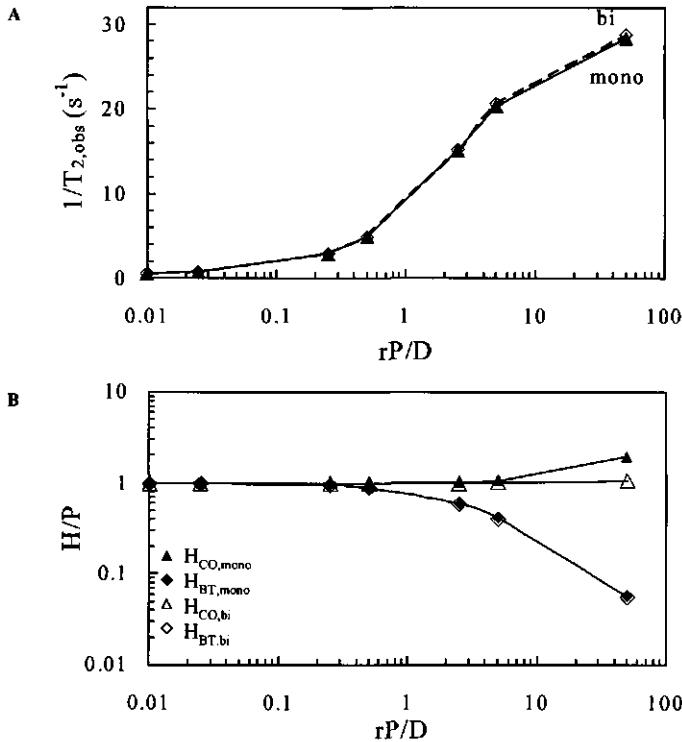


Figure 4.1. A. $1/T_2$ values for a single compartment with a perfect external sink vs. the membrane permeability H . The data were fitted either mono- or bi-exponentially and the largest $1/T_2$ value was displayed in the figure. The parameter rP/D contains the vacuolar radius r , the diffusion coefficient D and the tonoplast permeability P . The standard deviation of the simulations was less than 0.01% for the mono-exponential fits, and less than 0.1% for the bi-exponential fits. B. Calculated membrane permeability using the C-O (P , Eqn. 4.1) or B-T model (H , Eqn. 4.3) for either the mono- or the bi-exponential fit value of $1/T_2$.

Fig. 4.2A shows the short-time diffusion behaviour for different values of rP/D . According to Eqn. 4.6, there should be a linear relationship between D_{app} and $\sqrt{\Delta}$, and this is indeed approximately true for $rP/D \leq 1$. D_{bulk} can then be determined by extrapolation to $\Delta = 0$. For $rP/D = 10$, this relationship is no longer linear, and the obtained D_{bulk} will be about 10% too high. The long-term diffusion behaviour is solely determined by restriction due to the finite compartment size. Fig. 4.2B shows the compartment radius as calculated from Eqn. 4.5. As long as the membrane is closed, the compartment radius reflects the true compartment size. When the membrane becomes fairly permeable ($rP/D > 5$), the calculated radius decreases because molecules that cross the membrane hardly contribute to the signal, and only the remaining molecules from the 'inner' part of the compartment, which do not reach the membrane, give rise to the observed diffusion effect.

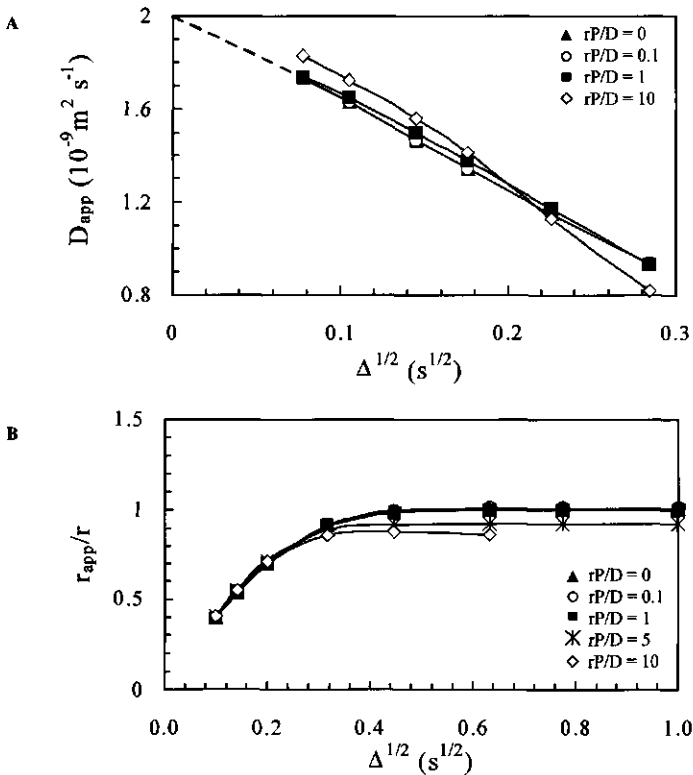


Figure 4.2. A. The apparent diffusion coefficient (D_{app}) for a single compartment with infinite external sink as a function of observation time for different membrane permeabilities. B. The apparent compartment radius (r_{app}) calculated from D_{app} . The standard deviation of the simulations was less than 0.1%.

SINGLE COMPARTMENT WITH A PARTIAL EXTRACELLULAR VOLUME SINK (ii)

Since we already found that the B-T theory is wider applicable, this method will be used to extract the sink strength parameter H for all other model systems treated in this paper. In most

biological systems, the extracellular magnetisation sink is not perfect. For a vacuolised plant cell, the main compartment (vacuole) is surrounded by a thin cytoplasmatic layer; the intrinsic relaxation rate of this layer is about ten times higher than that of the vacuole. To mimic the effect of such a partially relaxing sink, the same compartment as before was simulated, but now the extracellular space had a T_2 value of 0.2 s. The B-T theory does not account for this situation, however we used these formulas from this model to determine how far H deviates from P because of the presence of a partial sink. The relaxation curves were fitted mono-exponentially, which is reasonable because the ratio of vacuole volume to that of the cytoplasm/cell wall is about 20 to 1. From the resulting T_2 values H_{CO} and H_{BT} were calculated using Eqns. 4.1 and 4.3.

Fig. 4.3 shows the resulting sink strength parameters vs. rP/D . At a given input permeability the observed relaxation time $T_{2,obs}$ is larger than for a perfect extracellular volume sink, with the result that the true membrane permeability is underestimated. For a perfect sink, every molecule that crosses the membrane to the extracellular space instantaneously loses its magnetisation. For a partial sink however, the magnetisation contributes to the signal during the lifetime of the molecules in the extracellular space, resulting in a slower signal decay.

Fig. 4.4 shows the short-term (A) and long-term diffusion behaviour (B). For a perfect sink (Fig. 4.2), and $rP/D < 1$, i.e. the fast diffusion regime, D_{app} was independent of the membrane permeability. Therefore, the short-term diffusion coefficients for the present model should be comparable to those in Fig. 4.2, as is found indeed. When the membrane becomes more permeable, molecules close to the boundary will not always be reflected, but sometimes cross the membrane. This causes the effective diffusion length to increase, resulting in a higher apparent diffusion coefficient ($rP/D = 1$). For the long-term diffusion behaviour, a radius will be calculated that is larger than the actual compartment size (Fig. 4.4B). The extent of this deviation depends on both the membrane permeability and the effectiveness of the extracellular volume relaxation sink.

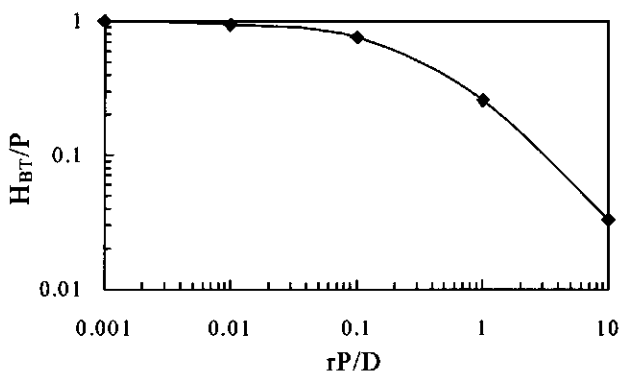


Figure 4.3. The calculated membrane permeability using the C-O (P , Eqn. 4.1) or B-T model (H_{BT} , Eqn. 4.3) for a single compartment with a finite external magnetisation sink ($T_{2,ext} = 0.2$ s), using a mono-exponential fit. The parameter rP/D contains the vacuolar radius r , the diffusion coefficient D and the tonoplast permeability P . The standard deviation of the simulations was less than 0.01%.

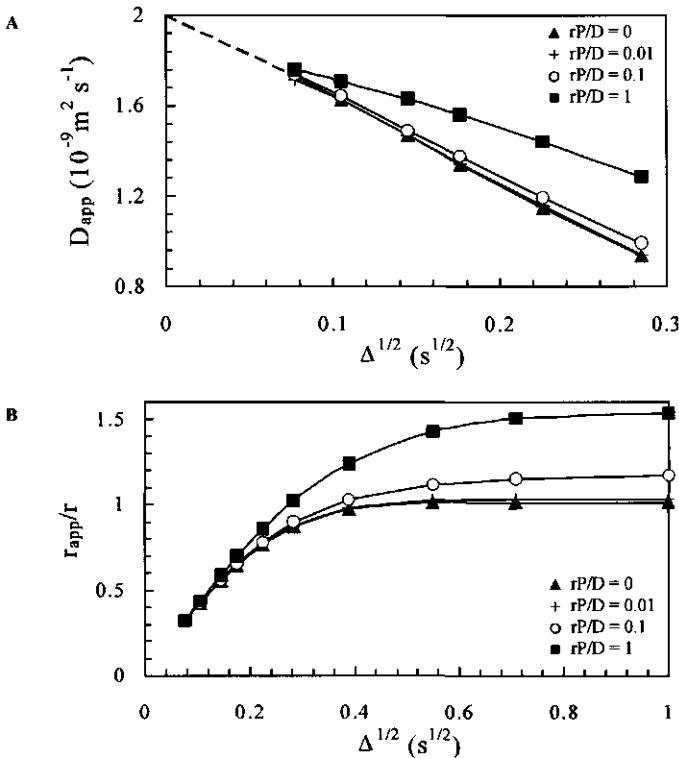


Figure 4.4. A. The apparent diffusion coefficient (D_{app}) for a single compartment with finite external sink ($T_{2,out} = 0.2$ s) vs. the observation time for different membrane permeabilities. B. The apparent compartment radius (r_{app}) calculated from D_{app} . The standard deviation of the simulations was less than 0.1%.

MULTI-COMPARTMENT SYSTEM (iii)

As a next step, a more realistic model of a plant cell was simulated. The cell is considered to be a system consisting of three concentric spherical compartments corresponding to the vacuole, cytoplasm, and the cell wall/extracellular space, respectively (Fig. 4.5A). The vacuole and the cytoplasm are separated by a semi-permeable membrane, the tonoplast, with a permeability coefficient P_{ton} . The plasmalemma, with a permeability coefficient P_{pl} , is located between the cytoplasm and the cell wall/extracellular space. The cell is considered to be an isolated system, so the outer boundary is fully reflective ($P_{out} = 0 \text{ m s}^{-1}$). As a starting-point a set of intrinsic parameters has been used which is reasonable for a true plant cell (Fig. 4.5A).⁶ The relaxation time $T_{2,vac}$ is expected to be close to that of water (ca. 2 s) and data on tissue with cells lacking large vacuoles suggest a $T_{2,cyt}$ value of about 0.2 s or shorter. The $T_{2,cw}$ value ranges from 5 to 30 ms or even larger, depending on the degree of hydration of the cell wall.^{5,41} Because of the cell wall obstruction, the diffusion coefficient D_{cw} is expected to be quite low, in the order of $10^{-10} \text{ m}^2 \text{ s}^{-1}$. The membrane permeabilities were varied over a large range, but the ratio P_{ton}/P_{pl} was kept constant at a value of 10, which is considered reasonable for a plant cell.⁴²

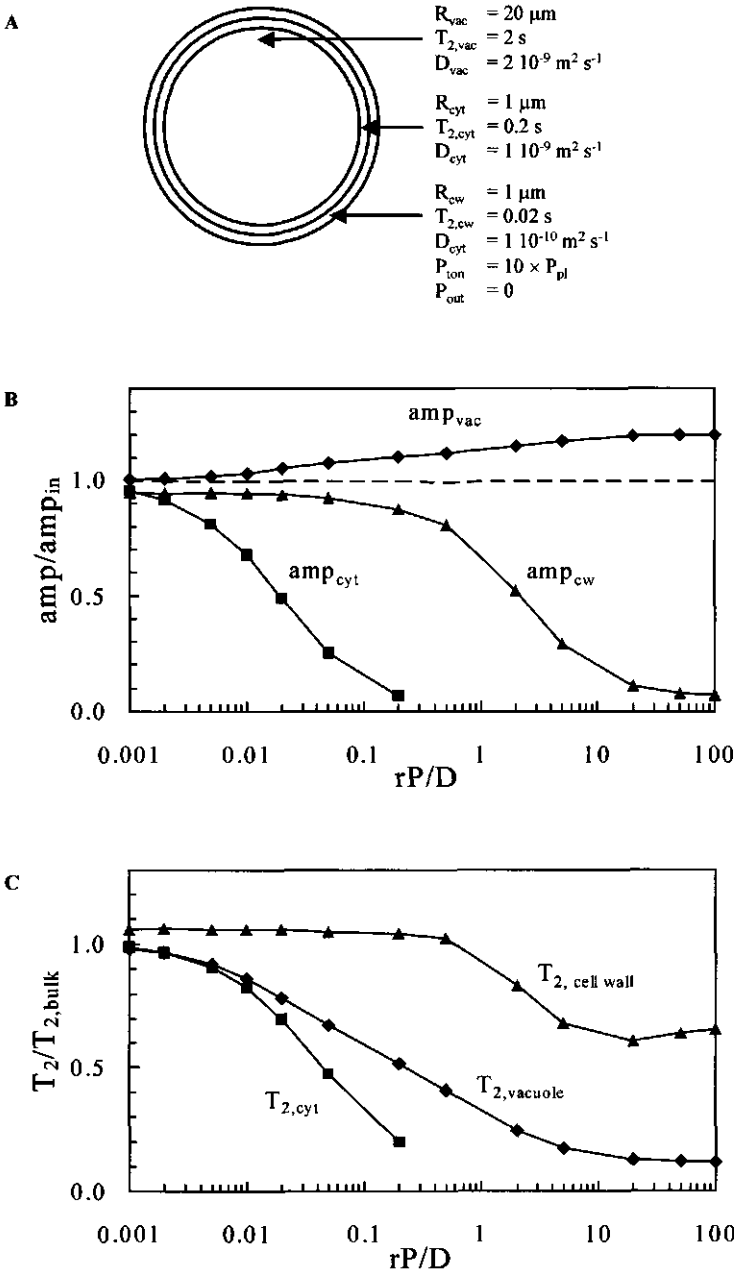


Figure 4.5. A. Schematic representation of the modelled cylindrical geometry. The inner compartment is the vacuole, surrounded by the cytoplasm and cell wall, respectively. For the meaning of the symbols, see text. B. Dependence of the calculated relative signal amplitudes $\text{amp}_{vac}/\text{amp}_{in}$, $\text{amp}_{cyt}/\text{amp}_{in}$, and $\text{amp}_{cw}/\text{amp}_{in}$ of the vacuole, the cytoplasm, and the cell wall, respectively, on the tonoplast and plasmalemma permeabilities ($H_{ion} = 10 \cdot H_{pl}$). amp_{in} is the input signal amplitude for the different compartments. The parameter rP/D contains the vacuolar radius r , the diffusion coefficient D and the tonoplast permeability P . C. The calculated relaxation times corresponding to the three fractions in B. The standard deviation of the fits was less than 0.1% for the longest component, and 1-2% for the shorter component.

Typical permeabilities of plant cells vary over several orders of magnitude, from $\sim 1 \times 10^{-6}$ to $1 \times 10^{-4} \text{ m s}^{-1}$ for the plasmalemma.^{42,43}

Fig. 4.5 shows the effect of the membrane permeability on the observed amplitudes (B) and relaxation times (C) of the observed water fractions as a function of P_{ton} . For low permeabilities ($rP_{ton}/D < 0.001$) the relaxation times and fractions approach the input values of the three compartments. For very high permeabilities ($rP_{ton}/D > 10$) complete exchange between the different fractions is found. In principle, this should result in mono-exponential relaxation behaviour; in fact, the small remaining fraction that is attributed to the cell wall mainly consists of the higher order relaxation components of the vacuolar fraction in the B-T theory. For intermediate values of rP_{ton}/D , the cytoplasmic component disappears due to exchange, whereas the extracellular component still remains constant because P_{pl} is a factor 10 lower than P_{ton} . The longest T_2 value is used to calculate H_{BT} (Eqn. 4.3) resulting in an almost linear relationship between $1/T_2$ and the membrane permeability (Fig. 4.6). However, H_{BT} is not equal to the tonoplast permeability P_{ton} , since the cytoplasm and cell wall are imperfect volume sinks. The actual relation between $T_{2,obs}$ and the calculated permeability depends on the permeabilities of the tonoplast as well as of the plasmalemma and on the effectiveness of the sink, *i.e.* on the relaxation times and dimensions of the cytoplasm and cell wall/extracellular space. $T_{2,obs}$ becomes independent of the permeability in the 'diffusion limited' regime ($rP/D > 10$) and is then determined by the vacuolar radius, the intrinsic relaxation times and the diffusion coefficients of the different compartments.

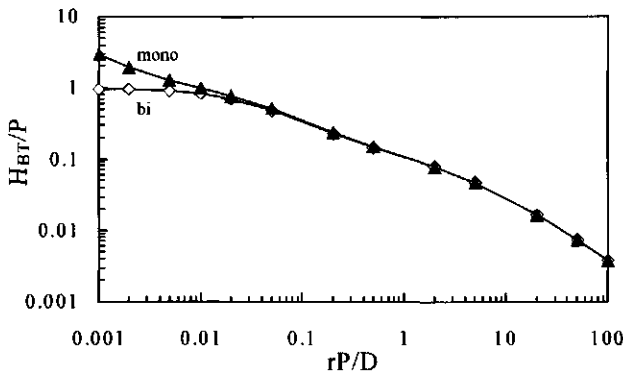


Figure 4.6. The calculated membrane permeability using the B-T model (H_{BT} , Eqn. 4.3) for the model system presented in Fig. 4.5A derived from a mono-exponential fit or the largest T_2 fraction in a bi-exponential fit. The standard deviation of the simulations was less than 0.01% for the mono-exponential fits, and less than 0.1% for the bi-exponential fits.

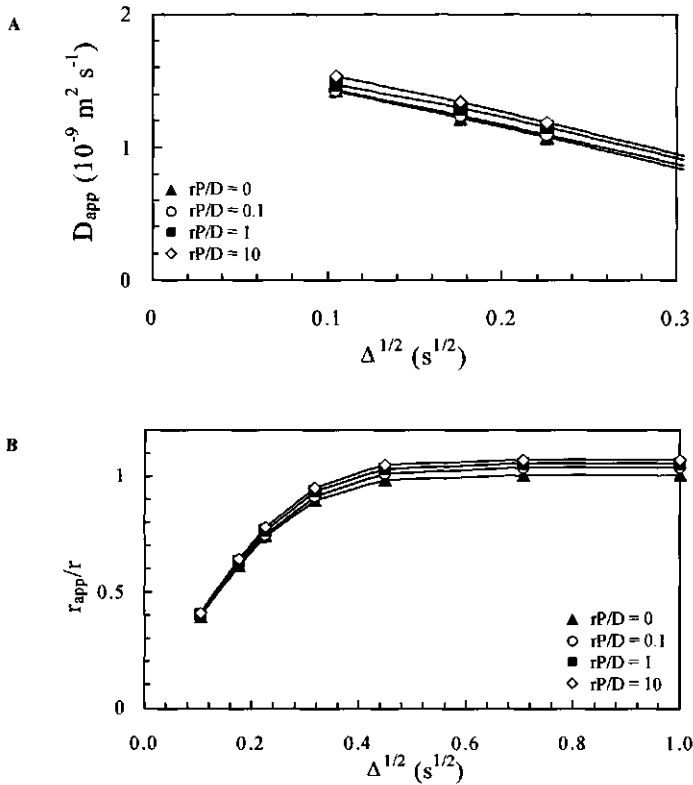


Figure 4.7. A. The apparent diffusion coefficient (D_{app}) for the model system in Fig. 4.5A vs. the observation time for different membrane permeabilities. B. The apparent compartment radius (r_{app}) calculated from D_{app} . The standard deviation of the simulations was less than 0.1%.

Both the short-time and long-time diffusion behaviour show very little effect of increasing the membrane permeabilities (Fig. 4.7). We ascribe this to the small thickness of the cytoplasmic and cell wall layer, in contrast to Figs. 4.2 and 4.4, where the extracellular space is infinitely large. D_{bulk} can be obtained by linearly extrapolating the curves in Fig. 4.7A to $\Delta = 0$, and reflects the average bulk diffusion coefficient for all compartments ($1.74 \times 10^{-9} \text{ m}^2 \text{ s}^{-1}$). Because the cell is considered a closed system, the maximum diffusion distance is 22 μm , and this distance is indeed obtained for large values of rP/D (Fig. 4.7B).

In an experimental situation, the error of the measurements is often too large to be able to distinguish the curves in Fig. 4.7, and the obtained parameters D_{bulk} and r can be considered reliable within the experimental error. The calculated membrane permeability is a superposition of all factors composing the relaxation sink, but it is linearly correlated with the actual membrane permeability and can thus be used to monitor this parameter.

CELL-TO-CELL TRANSPORT (iv)

Biological tissue does not consist of isolated cells; cell-to-cell transport significantly contributes to the water movement in tissues. Therefore, we considered the effect of this transport on diffusion and relaxation. A cylindrical model is not suited to model multiple cells; we therefore used a planar model consisting of four planar cells with a thin cell wall layer on each side of the large vacuolar compartment (Fig. 4.8A).¹⁵ The vacuole cross-section was 30 μm , which is the average diffusion distance in one direction for the previously used cylindrical cell with a diameter of 40 μm . All intrinsic parameters were the same as for the isolated plant cell; only the cytoplasmic layer was omitted. The tonoplast permeability was $1 \times 10^{-4} \text{ m}^2 \text{ s}^{-1}$, so $rP_{\text{ton}}/D = 1$. The cell-to-cell permeability, P_{cc} , was varied between zero and infinite, to cover the entire range from four isolated cells to maximum contact between all cells.

The apparent cell radius was calculated from the long-term diffusion coefficient (Fig. 4.8B). When the cell-to-cell exchange increases, the apparent radius is no longer constant in time, but is again linearly related to $\sqrt{\Delta}$, because molecules that cross the membrane to the next cell continue to contribute to the maximum displacement. The slope however is not the same as for free diffusion, as the tonoplast membrane still imposes a barrier. The low T_2 of the cell wall causes relaxation of most of the molecules that pass the cell wall to the next cell. To illustrate this effect, $T_{2,\text{cw}}$ was increased to 0.2 s (Fig. 4.8B), and obviously now the effect of cell-to-cell connections becomes more pronounced.

In practice this means that the cell radius can safely be calculated from the r_{app} plot when the curve levels off to a steady state. If this is not the case, one has to realise that the calculated radius is influenced by cell-to-cell transport. This is however a trade-off, since those transport processes are also of great interest, *e.g.* for overall tissue hydraulics.

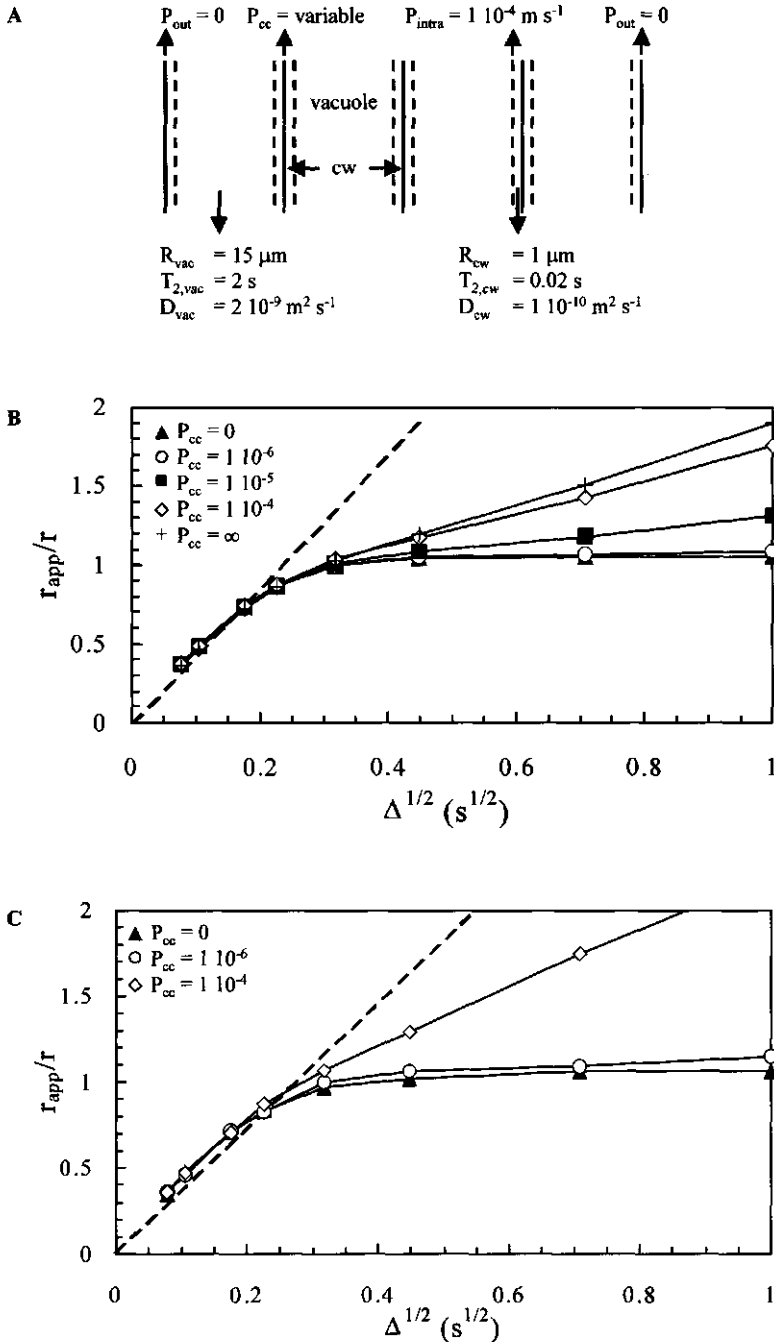


Figure 4.8. A. Schematic representation of the modelled geometry. The tissue is considered as an array of planar compartments. The "permeability" of the boundary layer between the cell walls of adjacent cells regulates the cell-to-cell transport. B. The apparent compartment radius (r_{app}) calculated from D_{app} for a cell wall with $T_2 = 20 \text{ ms}$. C. The apparent compartment radius calculated from D_{app} for a cell wall with $T_2 = 0.2 \text{ s}$. The standard deviation of the simulations was less than 0.1%.

CONCLUSIONS

The results of simulations of different biological systems of increasing complexity show that the sink strength parameter H can best be calculated by the B-T theory, especially in the slow diffusion regime ($rP/D > 1$). For multi-compartment systems, the calculated H reflects the combined effect of all permeability coefficients and the effectiveness of the sinks in the different compartments.

The short-term diffusion coefficient is governed by the amount of spins near the surface, which is determined by the surface to volume ratio of the compartments, and can be used to extract the bulk diffusion coefficient. The calculated value of D_{bulk} for a complex multi-compartmental cell reflects the average bulk diffusion coefficient of all compartments. When this value is used to calculate H_{BT} according to the B-T model, the membrane permeability is underestimated, but still linearly correlated to the actual membrane permeability. In practice this means that changes in membrane permeability can be observed and quantified, though the obtained values do not necessarily correspond to the permeability of a single membrane.

The cell radius can be calculated from the long-term diffusion coefficient. However, exchange effects can obscure the results. Since the shape of the r_{app} plot (see Figs. 4.7 and 4.8) reflects the influence of cell-to-cell transport, the results of measurements over a large range of diffusion observation times can be used to estimate whether this kind of transport has to be taken into account.

ACKNOWLEDGEMENTS

This Chapter has been submitted as:

Van der Weerd L., Snaar J.E.M., Vergeldt F.J. & Van As H. (2002) Simulation of relaxation, diffusion and exchange in multi-compartment systems as observed by NMR. To *Biophysical Journal*.

The authors wish to thank Prof. T.J. Schaafsma for useful comments.

REFERENCES

1. Ratcliffe R.G. (1994) In vivo NMR studies of higher plants and algae. Oxford, Academic Press Limited.
2. MacFall J.S. & Van As H. (1996) Magnetic resonance imaging of plants. In: Nuclear magnetic resonance in plant biology (eds Shachar-Hill Y. & Pfeffer P.E.), 33-76. The American Society of Plant Physiologists.
3. Le Bihan D. (1991) Molecular diffusion nuclear magnetic resonance imaging. *Magnetic Resonance Quarterly* 7, 1-30.
4. Lynch L.J. (1983) Water relaxation in heterogeneous and biological systems. *Magnetic Resonance in Biology* 2, 248-304.
5. Hills B.P. & Duce S.L. (1990) The influence of chemical and diffusive exchange on water proton transverse relaxation in plant tissues. *Magnetic Resonance Imaging* 8, 321-332.
6. Snaar J.E.M. & Van As H. (1992) Probing water compartment and membrane permeability in plant cells by proton NMR relaxation measurements. *Biophysical Journal* 63, 1654-1658.
7. Conlon T. & Outhred R. (1972) Water diffusion permeability of erythrocytes using an NMR technique. *Biochimica et Biophysica Acta* 288, 354-361.
8. Brownstein K.R. & Tarr C.E. (1979) Importance of classical diffusion in NMR studies of water in biological cells. *Physical Review A* 19, 2446-2453.
9. Van der Weerd L., Claessens M.M.A.E., Ruttink T., Vergeldt F.J., Schaafsma T.J. & Van As H. (2001) Quantitative NMR microscopy of osmotic stress responses in maize and pearl millet. *Journal of Experimental Botany* 52, 2333-2343.
10. Scheenen T.W.J., Heemskerk A.M., de Jager P.A., Vergeldt F.J. & Van As H. (2002) Functional imaging of plants: A nuclear magnetic resonance study of a cucumber plant. *Biophysical Journal* 82, 481-492.
11. Van Dusschoten D., Moonen C.T., De Jager P.A. & Van As H. (1996) Unraveling diffusion constants in biological tissue by combining Carr-Purcell-Meiboom-Gill imaging and pulsed field gradient NMR. *Magnetic Resonance in Medicine* 36, 907-913.
12. Hills B.P. & Snaar J.E.M. (1992) Dynamic q space microscopy of cellular tissue. *Molecular Physics* 76, 979-994.
13. Pfeuffer J., Floegel U., Dreher W. & Leibfritz D. (1998) Restricted diffusion and exchange of intracellular water: Theoretical modelling and diffusion time dependence of H-1 NMR measurements on perfused glial cells. *NMR in Biomedicine* 11, 19-31.
14. Wycoff W., Pickup S., Cutter B., Miller W. & Wong T.C. (2000) The determination of the cell size in wood by nuclear magnetic resonance diffusion techniques. *Wood and Fiber Science* 32, 72-80.
15. Novikov E.G., van Dusschoten D. & Van As H. (1998) Modeling of self-diffusion and relaxation time NMR in multi-compartment systems. *Journal of Magnetic Resonance* 135, 522-528.
16. Kuchel P.W. & Durrant C.J. (1999) Permeability coefficients from NMR q-space data: Models with unevenly spaced semi-permeable parallel membranes. *Journal Of Magnetic Resonance* 139, 258-272.
17. Van Dusschoten D., De Jager P.A. & Van As H. (1995) Extracting diffusion constants from echo-time-dependent PFG NMR data using relaxation-time information. *Journal of Magnetic Resonance A* 116, 22-28.

18. Li J.G., Stanisz G.J. & Henkelman R.M. (1998) Integrated analysis of diffusion and relaxation of water in blood. *Magnetic Resonance in Medicine* **40**, 79-88.
19. Stanisz G.J., Li J.G., Wright G.A. & Henkelman R.M. (1998) Water dynamics in human blood via combined measurements of T-2 relaxation and diffusion in the presence of gadolinium. *Magnetic Resonance in Medicine* **39**, 223-233.
20. Does M. & Gore J. (2000) Compartmental study of diffusion and relaxation measured in vivo in normal and ischemic rat brain and trigeminal nerve. *Magnetic Resonance in Medicine* **43**, 837 - 844.
21. Schobert S., Bar N., Kramer R. & Karger J. (2000) Pulsed high-field gradient in vivo NMR spectroscopy to measure diffusional water permeability in *Corynebacterium glutamicum*. *Analytical Biochemistry* **279**, 100-105.
22. Smouha E. & Neeman M. (2001) Compartmentation of intracellular water in multicellular tumor spheroids: Diffusion and relaxation NMR. *Magnetic Resonance in Medicine* **46**, 68-77.
23. Norris D.G. (2001) The effects of microscopic tissue parameters on the diffusion weighted magnetic resonance imaging experiment. *NMR in Biomedicine* **14**, 77-93.
24. Stanisz G.J., Szafer A., Wright G.A. & Henkelman R.M. (1997) An analytical model of restricted diffusion in bovine optic nerve. *Magnetic Resonance in Medicine* **37**, 103-111.
25. Beaulieu C., Fenrich F.R. & Allen P.S. (1998) Multicomponent water proton transverse relaxation and T-2-discriminated water diffusion in myelinated and nonmyelinated nerve. *Magnetic Resonance Imaging* **16**, 1201-1210.
26. Karczmar G. (1994) Imaging, diffusion, perfusion, and flow. In: *NMR in physiology and biomedicine* (eds Gillies R.J.), 25-42. San Diego, Academic Press Inc.
27. Fenrich F.R.E., Beaulieu C. & Allen P.S. (2001) Relaxation times and microstructures. *NMR in Biomedicine* **14**, 133-139.
28. Bauer W.R. & Schulten K. (1992) Theory of contrast agents in magnetic resonance imaging: Coupling of spin relaxation and transport. *Magnetic Resonance in Medicine* **26**, 16-39.
29. Barsky D., Putz B. & Schulten K. (1997) Theory of heterogeneous relaxation in compartmentalized tissues. *Magnetic Resonance in Medicine* **37**, 666-675.
30. Belton R.S. & Ratcliffe R.G. (1985) NMR and compartmentation in biological tissues. *Progress in NMR spectroscopy* **17**, 241-279.
31. Van der Weerd L., Melnikov S.M., Vergeldt F.J., Novikov E.G. & Van As H. (2001) Modelling of self-diffusion and relaxation time NMR in multi-compartment systems with cylindrical geometry. *Journal of Magnetic Resonance* submitted.
32. Zhang W.H. & Jones G.P. (1996) Water permeability in wheat root protoplasts determined from nuclear magnetic resonance relaxation times. *Plant Science* **118**, 97-106.
33. Snaar J.E.M. & Van As H. (1993) NMR self-diffusion measurements in a bounded system with loss of magnetization at the walls. *Journal of Magnetic Resonance A* **102**, 318-326.
34. Hills B.P., Wright K.M. & Belton P.S. (1990) The effects of restricted diffusion in nuclear magnetic resonance microscopy. *Magnetic Resonance Imaging* **8**, 755-765.

35. Soderman O. & Jonsson B. (1995) Restricted diffusion in cylindrical geometry. *Journal of Magnetic Resonance A* **117**, 94-97.
36. Callaghan P.T. (1993) Principles of nuclear magnetic resonance microscopy. Oxford, Clarendon Press.
37. Mitra P.P., Sen P.N. & Schwartz L.M. (1993) Short-time behavior of the diffusion coefficient as a geometrical probe of porous media. *Physical Review B* **47**, 8565-8574.
38. Latour L.L., Mitra P.P., Kleinberg R.L. & Sotak C.H. (1993) Time-dependent diffusion coefficient of fluids in porous media as a probe of surface-to-volume ratio. *Journal of Magnetic Resonance A* **101**, 342-346.
39. Valiullin R. & Skirda V. (2001) Time dependent self-diffusion coefficient of molecules in porous media. *Journal of Chemical Physics* **114**, 452-458.
40. Provencher S.W. & Vogel R.H. (1983) Regularization techniques for inverse problems in molecular biology. In: Numerical treatment of inverse problems in differential and integral equations (eds Deuffhard P. & Hairer E.), 304-319. Boston, Birkhauser.
41. Stout D.G., Steponkus P.L. & Cotts R.M. (1978) Nuclear magnetic resonance relaxation times and plasmalemma water exchange in ivy bark. *Plant Physiology* **62**, 636-641.
42. Tyerman S.D., Bohnert H.J., Maurel C., Steudle E. & Smith J.A.C. (1999) Plant aquaporins: Their molecular biology, biophysics and significance for plant water relations. *Journal of Experimental Botany*, 1055-1071.
43. Maurel C. (1997) Aquaporins and water permeability of plant membranes. *Annual Review of Plant Physiology and Plant Molecular Biology* **48**, 399-429.

5

QUANTITATIVE NMR MICROSCOPY OF OSMOTIC STRESS RESPONSES IN MAIZE AND PEARL MILLET

*The effect of osmotic stress (-0.35 MPa) on the cell water balance and apical growth was studied non-invasively for maize (*Zea mays* L., cv LG 11) and pearl millet (*Pennisetum americanum* L., cv MH 179) by ^1H NMR microscopy in combination with water uptake measurements. Single parameter images of the water content and the transverse relaxation time (T_2) were used to discriminate between the different tissues and to follow the water status of the apical region during osmotic stress. The T_2 values of non-stressed stem tissue turned out to be correlated to the cell dimensions as determined by optical microscopy. Growth was found to be strongly inhibited by mild stress in both species, whereas the water uptake was far less affected. During the experiment hardly any changes in water content or T_2 in the stem region of maize were observed. In contrast, the apical tissue of pearl millet showed a decrease in T_2 within 48 hours of stress. This decrease in T_2 is interpreted as an increase in the membrane permeability for water.*

INTRODUCTION

Drought stress considerably reduces crop yields world wide compared to the maximum attainable yields.^{1,2} Therefore, plant responses to water deficits are of great interest in plant research, from the cellular up to the whole plant level.

One of the processes in plants the most sensitive to water deficits is growth,³ making this process an excellent parameter for studies of drought tolerance mechanisms in plants and the differences between species. Though many groups reported on the stress response of growth for roots,⁴ leaves^{5,6} and stems,^{7,8} monitoring the growth of the shoot apex has always been complicated by the use of invasive methods, which impede the measurement of the apex response to processes as drought stress at a physiologically relevant time scale.

Other drought stress responses on all organisational levels have been widely studied.^{2,9,10} However, up to now little attention has been paid to the integration of drought stress responses at the cell, organ, and whole plant level. This is scarcely surprising since non-invasive methods for studying whole plants on the organ or even cell level have only recently become available by means of Nuclear Magnetic Resonance imaging (NMR or MRI).

During the past few decades NMR has been applied in a number of plant studies.¹¹⁻¹⁴ Different from light microscopy, NMR images of plants display the physical status and the

spatial distribution of water within plant tissues in addition to anatomical information. Examples are flow images, representing quantitative flow velocities of xylem and phloem water¹⁵⁻¹⁸ and T_2 , diffusion and amplitude images.^{12,19-21} The amplitude, or the initial NMR signal intensity, is directly related to the number of protons in the observed part of the system. Since in plant tissue the proton signal is dominated by water protons, the NMR signal amplitude is proportional to the tissue density \times tissue water content per voxel.²⁰

According to Brownstein and Tarr,^{22,23} the observed T_2 of water in a confined compartment can be described as a function of the bulk T_2 ($T_{2,bulk}$), the radii of the compartment along the x, y and z direction ($R_{x,y,z}$) and the rate of wall relaxation or surface sink strength density (H):

$$1/T_{2,obs} = H(1/R_x + 1/R_y + 1/R_z) + 1/T_{2,bulk} \quad [5.1]$$

This model can in principle be applied to plant cells, with the vacuole as the main (largest) compartment with a relatively long bulk relaxation time. The cytoplasm and apoplast have a much shorter relaxation time and act therefore as a sink for the vacuole, whereas the tonoplast and plasmalemma membranes determine the exchange rates between these compartments. This relation between T_2 and permeability was also demonstrated in the diffusion simulations of Hills and Snaar.²⁴ The sink strength density (H) is defined as the rate of net loss of magnetisation at the compartment surface, and will thus reflect the membrane permeabilities for water and the relaxation parameters of the cytoplasm. This model has been applied previously to spherical and cylindrical cell volumes,^{20,25} and here it is expanded to an ellipsoid volume, where all three radii R_x , R_y and R_z can be different.

In this paper the spin-spin relaxation time T_2 and the signal amplitude are used to monitor changes in the water balance of the plant stem, which should reflect adaptation processes between tissues during osmotic stress, such as membrane permeability changes and redistribution of water. Maize and pearl millet are compared, of which the latter is more drought tolerant. The results of our study demonstrate that many aspects of plant responses to drought stress can be revealed non-invasively by applying NMR imaging to the shoot apical growth and water balance in maize and pearl millet as they respond to osmotic stress. The NMR results are combined with those of water uptake measurements, thus correlating the stress response of the apex and its surrounding tissues with the water intake and possible dehydration of the whole plant.

MATERIALS AND METHODS

PLANT MATERIAL

Maize (*Zea mays L.*, cv LG 11) and pearl millet (*Pennisetum americanum L.*, cv MH 179) seeds were germinated in wet sand in the dark. After one week the seedlings were transferred to water culture with half Hoagland nutrient solution,²⁶ which was refreshed every week. All plants were grown in separate vessels, which were designed to fit in the NMR imager directly, to prevent root damage when the plants were transferred. The plants were grown in a phytotron at 25 °C and 70% relative humidity with a photoperiod of 16 hours and a light intensity of 40 W m⁻² (mercury vapour lamp). When used, the plants were 4 or 6 weeks old, with 6 or 9 fully emerged leaves respectively.

EXPERIMENTAL SET-UP

Fig. 5.1 shows the experimental set-up for the water uptake measurements and NMR imaging. The roots of the plant were grown in a glass vessel, containing continuously aerated nutrient solution. The medium was pumped into the vessel from below while excess medium was removed at the top to maintain a constant medium volume in the vessel. The stem was fixed in the vessel to prevent plant movement during the measurements. The weight of the root medium vessel was measured using a balance (Ohaus GT 8000, Germany or Sartorius LP3200D, Germany). Osmotic stress was applied by replacing the normal root medium by a -0.35 MPa solution of Polyethylene Glycol (PEG 6000, 162.3 g kg⁻¹) in nutrient medium. The shoot of the plant was housed in a climate chamber with an air temperature of 26 ± 1 °C and a relative humidity of 50 ± 2% with a photoperiod of 16 hours and a light intensity of 70 W m⁻².

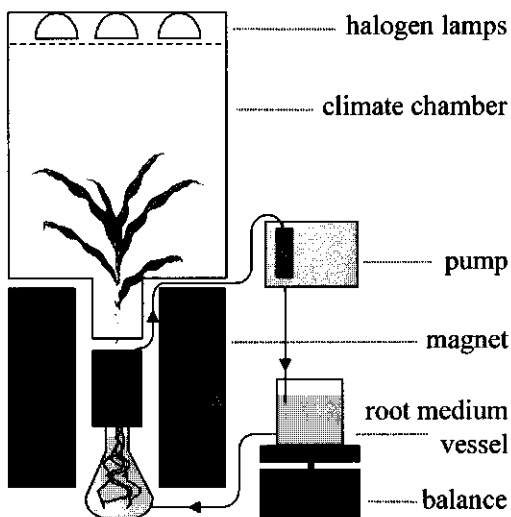


Figure 5.1. Schematic representation of the experimental set-up.

MRI EXPERIMENTS

Three types of experiments were carried out:

(i) Non-stress conditions. The shoot apical region of maize was imaged using NMR microscopy under non-stress conditions (N=2). Water uptake was recorded to monitor the recovery or adaptation of the plant to the new environment after insertion into the NMR imager.

(ii) T_2 and cell size. The stems of maize (N=4) and pearl millet (N=5) were imaged from the shoot apex down over a length of about 20 cm under normal non-stress conditions. The same plants were used for light microscopy in order to determine the parenchyma cell dimensions in the different internodes.

(iii) Stress conditions. NMR microscopy of the shoot apical region of maize (N=2) and pearl millet (N=2) was combined with water uptake measurements. The plants were followed for six days: the first two days under normal conditions, the second two days during osmotic stress and the third two days during recovery. For pearl millet the experiment was partially repeated (N=2), recording NMR imaging data under the initial, normal conditions and after 48 hours of osmotic stress.

The NMR spectrometer was a 20.35 MHz imager consisting of a 0.47 T Bruker electromagnet (Karlsruhe, Germany) controlled by a S.M.I.S. console (S.M.I.S., Guildford, England). In contrast to most NMR imagers, this machine has an open access in two directions, and plants can be measured in the normal, vertical, position. A shielded gradient probe with an open cylindrical access of 45 mm was used (Doty Scientific Inc., Columbia, South Carolina, USA). T_2 values were measured using a multi-spin-echo imaging pulse sequence with slice selection,^{20,27} a repetition time (TR) of 1800 ms, a spin-echo time (TE) of 4.3 ms and a spectral bandwidth of 50 kHz. A 128 × 128 matrix of complex data points was acquired per echo, and typically 48 or 64 echoes were acquired per echo train. For each image four acquisitions were averaged to improve the image quality, resulting in a total scan time of 15 minutes per image. For experiment (i) transverse images and for experiment (ii) longitudinal images were obtained, whereas for experiment (iii) both transverse and longitudinal images were acquired. The in-plane resolution was 235 μm for the transverse images and 390 μm for the longitudinal images, both with a slice thickness of 3.0 mm.

The acquired NMR data sets were analysed by home-written calculation routines in IDL (Research Systems Inc., Boulder, Colorado, USA). The multi-echo images were fitted on a pixel-by-pixel base using a mono-exponential decay function, yielding quantitative amplitude and $1/T_2$ images.^{20,27,28} After phase correction, the real part of the signal was used for analysis.²⁹

LIGHT MICROSCOPY AND CRYO-SEM MICROSCOPY

The same plants as used for MRI (ii) were also used to determine the cell dimensions. Fresh longitudinal sections of the internodes were prepared using a hand microtome and fixed on a microscope slide using Kayser's glycerol gelatine (Merck 9242, Darmstadt, Germany). The slices were several cell layers thick; average cell sizes for the individual plants were determined by focussing the microscope on a central cell layer and measuring 60 randomly selected cells in two dimensions for every internode by hand. The length and position of each section was measured to correlate the results to the NMR images.

Fresh longitudinal and transverse slices of the middle part of a 1-cm-length stem internode of both plants were cut with a sledge microtome and embedded in Kayser's glycerol gelatine. Digital images (768 × 592 pixels) were made with a Sony 3CCD camera mounted on a light microscope.

For the Cryo Scanning Electron Microscopy, internodes of 1 cm length of both plants were cut into longitudinal slices with a razor blade and plunged in liquid propane and stored in liquid nitrogen. The slices were fractured at -88 °C and freeze-etched for three minutes in an Oxford CT 1500 HF cryo transfer unit and sputter coated with 10 nm platinum. The cut surface was studied with a JEOL 6300F field emission scanning electron microscope at -194 °C at 2.5 kV.

RESULTS

NON-STRESS CONDITIONS (i)

The water uptake was measured for a six-week-old maize plant after transfer to the imager (Fig. 5.2). During the first hours after transfer, the uptake rate was clearly reduced with respect to the stabilised uptake rate after a few days of adaptation. These measurements showed that the recovery of a plant after transfer took about one day. The adaptation of the plant following the transfer was also observable in the growth rate of the plants, which was almost zero during the first hours of the experiment and gradually increased during the first day (see Fig. 5.11).

Comparison of the uptake data after adaptation (Fig. 5.2) with similar data acquired on plants outside the apparatus shows no effect of the NMR measurements on water uptake (data not shown). Apical growth cannot be measured non-invasively on such a short time scale outside the NMR system, but the stabilisation of the growth rate after adaptation in the NMR system and the agreement with the rates for internodial growth measured by monitoring the displacement of externally visible nodes every day³⁰ indicate that the plants are not noticeably influenced by the experiments. Though long-term effects of placing the plants in the apparatus seem to be minimal, inhibition of water uptake and growth does occur as a result of the

transfer for about one day (Figs. 5.2 and 5.11). This indicates that the results of these kinds of MRI studies on intact plants during the first day after setting up the experiment should be interpreted with great care.

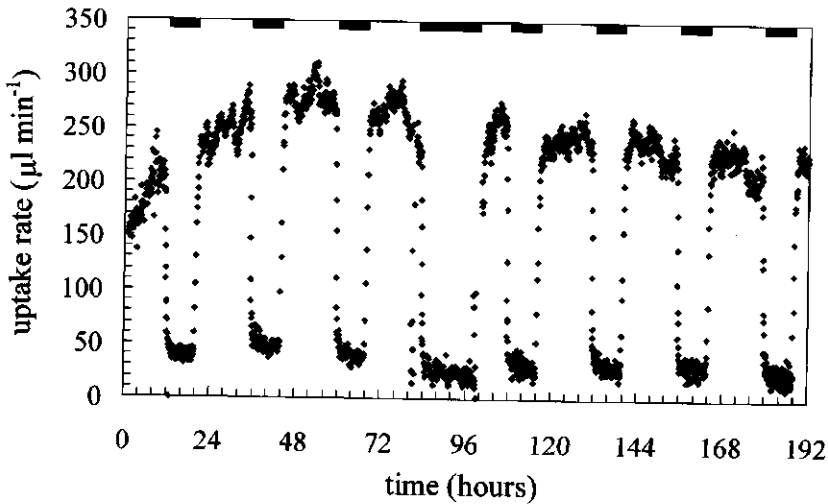


Figure 5.2. Water uptake rate of a six-week-old maize plant after transfer to the NMR apparatus. The black bars mark the dark periods.

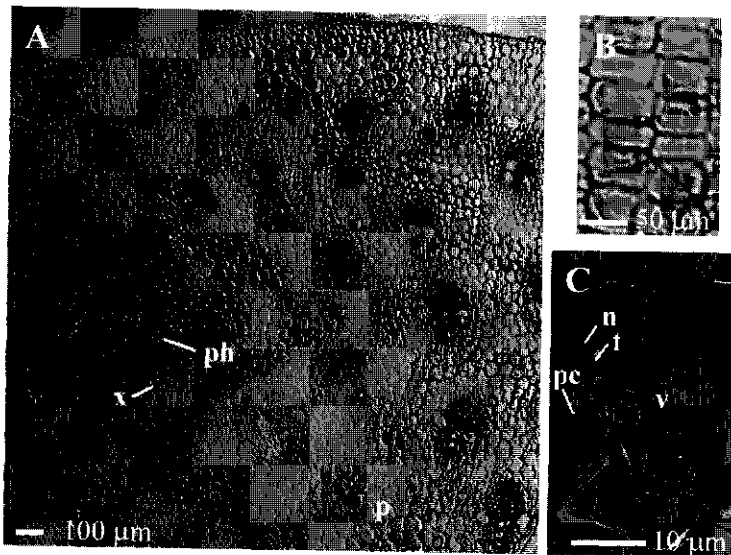


Figure 5.3. Optical and scanning electron micrographs of a maize stem. A. transverse section of an internode of about 10 mm length. B. Longitudinal section of the same internode. C. Cryo-SEM section of a single parenchyma cell. p = parenchyma, ph = phloem, x = xylem, v = vacuole, t = tonoplast membrane, pc = plasmalemma and cell wall, n = nucleus.

ANATOMY

Maize. The size of the parenchyma cells in the inner part of a stem internode is fairly homogeneous (Fig. 5.3A), as can be observed in the longitudinal section as well (Fig. 5.3B). The vascular bundles are scattered throughout the ground tissue and consist for this internode mainly of protoxylem and primary phloem. The SEM picture clearly shows that the parenchyma cells are completely vacuolised (Fig. 5.3C).

Longitudinal and transverse NMR images for one of the plants are shown in the Figs. 5.4 and 5.5. In the longitudinal $1/T_2$ images (Figs. 5.4 and 5.5A) the apex is clearly visible (a). Below the shoot apex the youngest internodes can be seen (b), separated by the nodes, which appear as bright regions (c). Within the immature internodes, the T_2 gradually increases from the bottom to the top. On either side of the apex, the leaves that surround the stem are visible (d). The young ear is situated directly above the apex (e), and can be seen as a grainy, brighter region (Fig. 5.4, e). The transverse images (Fig. 5.5B) clearly show the leaves (d), vascular bundles (f) and the onset of a cob (g). Note that the amplitude images show far less contrast, as expected because of a fairly uniform water content and tissue density for different plant tissues as expected on basis of difference in water content and tissue density.

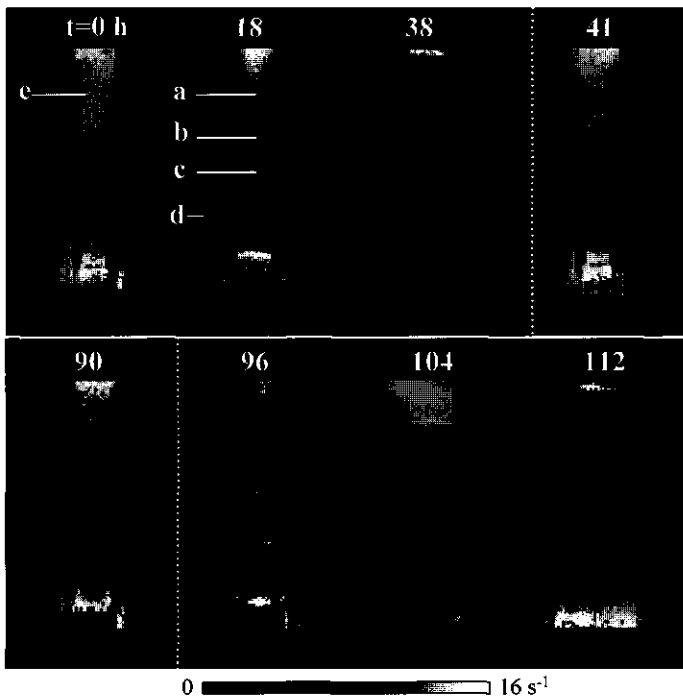


Figure 5.4. Selection of $1/T_2$ images acquired of a maize plant before osmotic stress ($t=0$ to $t=38$), during -0.35 MPa osmotic stress ($t=41$ to $t=90$) and during recovery ($t=96$ to $t=112$). The light was on for 16 hours daily (70 W m^{-2}). After $t=38$ the stem position was altered in order to position the apex in the middle of the image plane. The dotted lines mark the beginning and the end of the stress period.

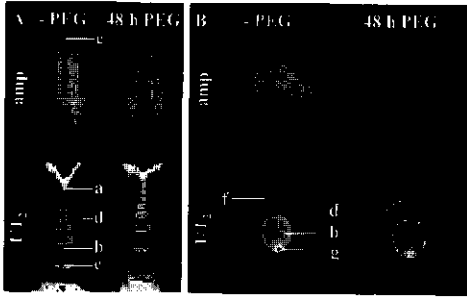


Figure 5.5. Longitudinal and transverse amplitude and $1/T_2$ images acquired of a maize plant before and after 48 hours of -0.35 MPa osmotic stress.

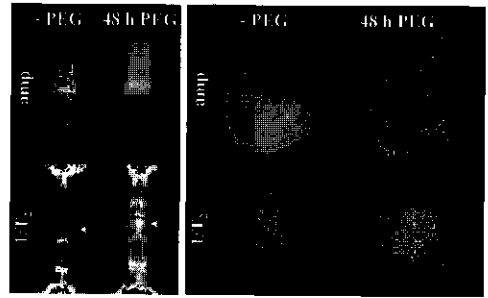


Figure 5.7. Longitudinal and transverse amplitude and $1/T_2$ images acquired of a millet plant before and after 48 hours of -0.35 MPa osmotic stress.

Pearl millet. As in maize, the parenchyma cells in the inner part of a stem internode are fairly homogeneous (Figs. 5.6A, 5.6B) and are completely vacuolised (Fig. 5.6C). Towards the edge of the stem, the cells become smaller. The vascular bundles are scattered throughout the ground tissue.

Though the millet stem has a similar nodular structure as maize, the anatomy as seen by NMR differs (Figs. 5.7 and 5.8). Most of the nodes consist of two sections (a, see Fig. 5.8), which have a higher T_2 value than the internodes. Furthermore, the larger nodes are not as homogeneous as in maize and there appears to be some variety in T_2 over the length of the nodes.

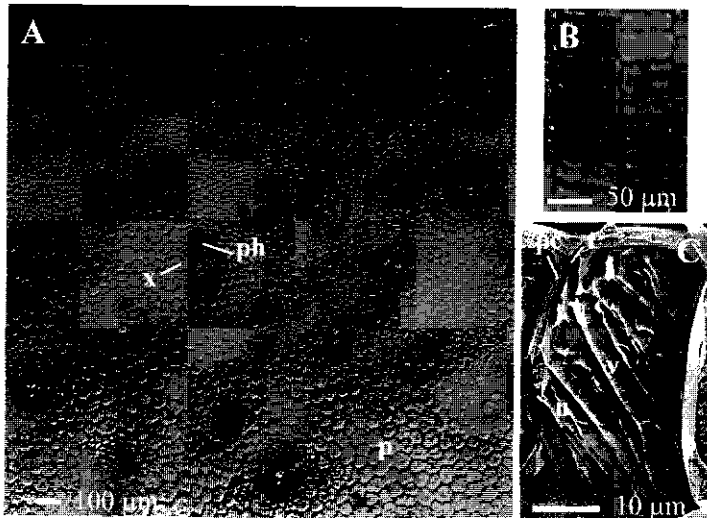


Figure 5.6. Optical and scanning electron micrographs of a millet stem. A. transverse section of an internode of about 10 mm length. B. Longitudinal section of the same internode. C. Cryo-SEM section of a single parenchyma cell. p = parenchyma, ph = phloem, x = xylem, v = vacuole, t = tonoplast membrane, pc = plasmalemma and cell wall, n = nucleus.

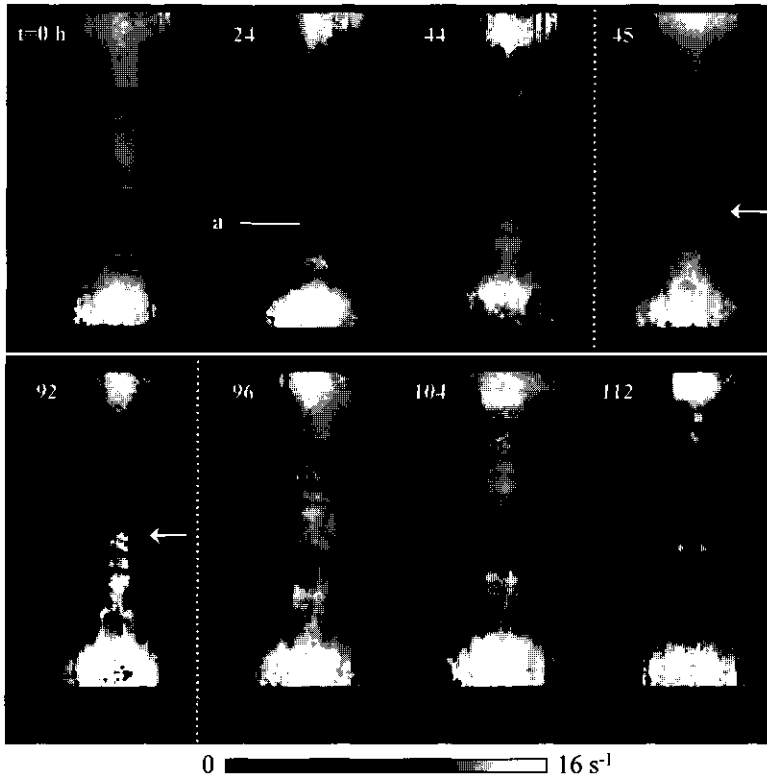


Figure 5.8. Selection of a number of longitudinal $1/T_2$ images acquired of a pearl millet plant before osmotic stress ($t=0$ to $t=44$), during -0.35 MPa osmotic stress ($t=45$ to $t=92$) and during recovery ($t=96$ to $t=112$). The light was on for 16 hours daily (70 W m^{-2}). After $t=44$ the stem position was altered in order to position the apex in the middle of the image plane. The dotted lines mark the beginning and the end of the stress period.

T_2 AND CELL SIZE (ii)

According to Eqn. 5.1, the observed relaxation rate $1/T_{2,obs}$ is expected to depend on the dimensions of the vacuole. The Figs. 5.4 and 5.5 indeed show a large variation in T_2 between the various internodes, which could be contributed to the different cell dimensions in these tissues. To verify whether this theoretical relation also holds for intact plants, maize and pearl millet plants were imaged from the shoot apex down to the roots. In Fig. 5.9, the $1/T_2$ values of the various internodes of a number of non-stressed plants (obtained from NMR images as shown in Fig. 5.5) are presented as a function of the cell size, which was determined afterwards by optical microscopy of the same plants. Clearly a linear correlation between cell dimensions and $1/T_2$ is demonstrated, that holds for a large range of cell sizes. The intercept of the fitted line in Fig. 5.9 corresponds to the $T_{2,bulk}$ of the vacuole, which is in this case around 2 s, as expected close to the T_2 of free water.²⁵ According to Eqn. 5.1, the slope of the line corresponds to the sink strength parameter H , yielding $H = (2.8 \pm 0.52) \times 10^{-5} \text{ m s}^{-1}$ for maize and $H = (4.0 \pm 0.44) \times 10^{-5} \text{ m s}^{-1}$ for millet.

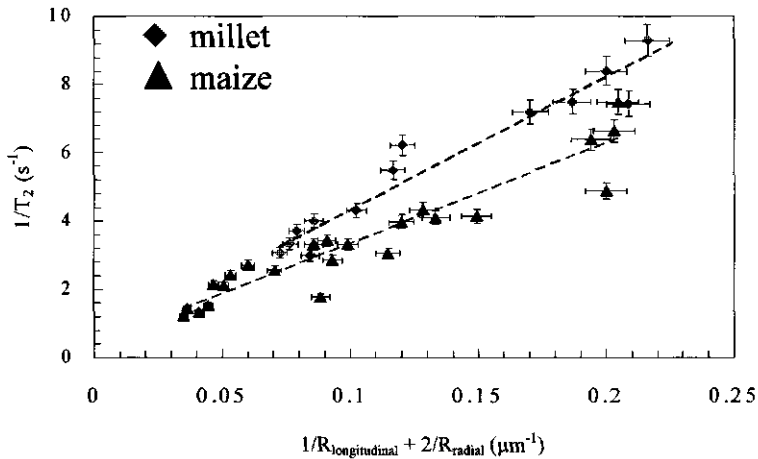


Figure 5.9. Relation between relaxation time and cell dimensions for maize ($n=4$) and pearl millet ($n=5$). The data points are taken from different internodes in the NMR images. After the NMR measurements, the same plants were used for microscopic sections to determine the cell dimensions.

MAIZE AND PEARL MILLET DURING STRESS (iii)

The stem apical region of approximately six-week-old maize plants was imaged to measure the growth rate of the shoot apex. $1/T_2$ images were obtained in both the longitudinal and transverse direction (Figs. 5.4 and 5.5). Simultaneously with the NMR experiments, the water uptake by the roots was monitored.

Water uptake. After osmotic stress was applied, the uptake rate during the day decreased to about 75% of the normal rate (Fig. 5.10). Besides, the uptake kinetics show a remarkable difference with those before and after osmotic stress. After the PEG solution had been replaced by normal root medium, the uptake rate increased, especially during the second day to 119% of the rate before stress was applied.

Growth. Elongation growth is presented in Fig. 5.11 by plotting the displacement of one particular internode versus time. Because the measured plants are not of exactly the same age, the node displacement is given in arbitrary units; the curves were scaled to have the same slope during 24 hours before stress. Though the water uptake during PEG stress was only reduced by 25%, growth was almost completely inhibited during the light periods, while during the dark periods growth occurred at a very reduced rate (5-8% of the normal rate during dark). During recovery the growth rate increased to 150% of the normal growth rate. These high rates remained unchanged for at least 24 hours.

Amplitude and T_2 . Before and after stress, the T_2 values for the various internodes increased in time because the cell size increased due to growth. During osmotic stress neither the T_2 values nor the water density in the stem noticeably changed (Figs. 5.4 and 5.5, Table 5.1). The T_2 values and the water density of the leaves (see amplitude images) showed a small decrease in time, caused by desiccation of the leaves.

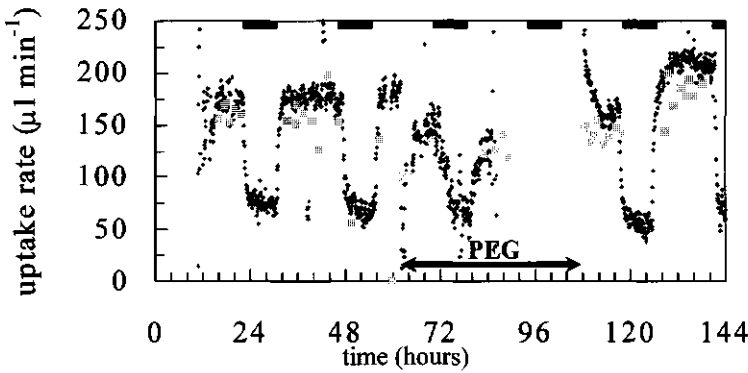


Figure 5.10. Water uptake rate of two maize plants, represented in black and grey, during -0.35 MPa osmotic stress. The dark periods are presented as black bars in the figure.

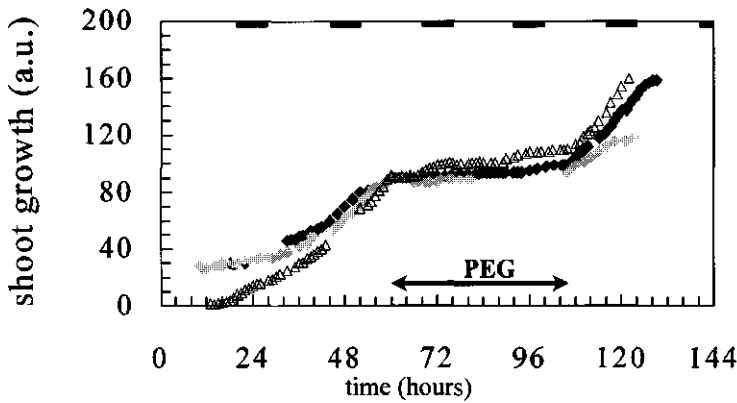


Figure 5.11. Relative growth of maize (\blacklozenge), represented in black and grey for two different plants, and pearl millet (\blacktriangle), during -0.35 MPa osmotic stress. The dark periods are presented as black bars in the figure.

PEG	Maize			Pearl Millet		
	Amplitude (a.u.)	$1/T_2$ (s^{-1})	H ($10^{-5} m s^{-1}$)	Amplitude (a.u.)	$1/T_2$ (s^{-1})	H ($10^{-5} m s^{-1}$)
0	1	5.72 ± 0.28	2.8	1	4.29 ± 0.13	4.0
24	0.99 ± 0.03	5.57 ± 0.24	2.7 ± 0.09	0.98 ± 0.02	4.93 ± 0.19	4.7 ± 0.18
48	0.97 ± 0.04	5.43 ± 0.18	2.7 ± 0.08	1.02 ± 0.03	5.32 ± 0.28	5.1 ± 0.26

Table 5.1. Changes in amplitude and T_2 of the central part of the 1-cm internode before stress, and after 24 and 48 hours of -0.35 MPa osmotic stress. The presented values are the mean of nine voxels taken from the longitudinal images as shown in Figure 5.5 and 5.7.

Identical experiments were done with pearl millet.

Water uptake. During PEG stress the rate decreased to about 86% of the normal rate, which is a less severe decline than in the case of maize (Fig. 5.12). No differences in uptake kinetics were observed either. During recovery the uptake rate slowly increased to the normal rate, but no increased uptake compared to normal was found.

Growth. During stress, growth was strongly inhibited, but not as much as in the maize plants (Fig. 5.11). During the day, the rate dropped to 2-3% of the normal value, whereas during the nights the rate was 12% of the normal rate. During recovery, the growth rate returned slowly to the normal rate in about 14 hours, but no increased rates as compared to those before stress were observed, as were found for maize.

T_2 . Just as for maize, the T_2 values for a particular internode increased before stress due to growth. During PEG stress however, the T_2 decreased significantly in all nodes of the stem apical region to 77% of its initial value (Figs. 5.7 and 5.8, Table 5.1). Despite this decline during stress, the water density images neither showed any decrease in water density nor in stem diameter, indicating that the stem tissue did not dehydrate or shrink noticeably. The initial sink strength parameter H and the corresponding cell dimensions can be estimated from Fig. 5.9, using the T_2 values from Table 5.1, yielding $H = 4.0 \times 10^{-5} \text{ m s}^{-1}$ and $(1/R_{\text{longitudinal}} + 2/R_{\text{radial}}) = 0.095 \text{ } \mu\text{m}^{-1}$ respectively for pearl millet. For maize these values are $H = 2.8 \times 10^{-5} \text{ m s}^{-1}$ and $(1/R_{\text{longitudinal}} + 2/R_{\text{radial}}) = 0.186 \text{ } \mu\text{m}^{-1}$. Assuming that the cell dimensions are constant since the water density and stem diameter did not change, the calculated radii can be used to estimate the corresponding increase in H during osmotic stress (Table 5.1).

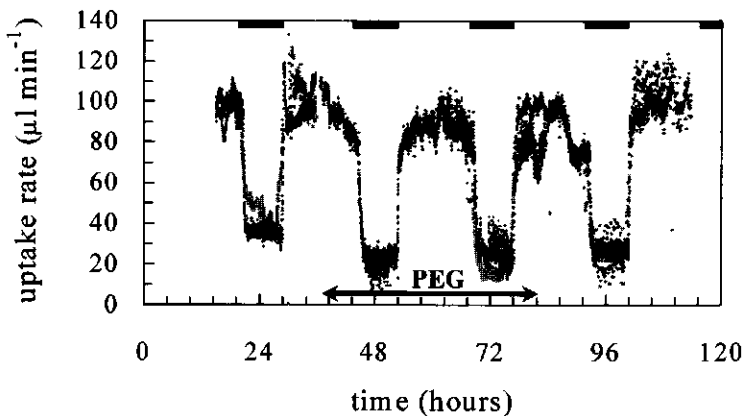


Figure 5.12. Water uptake rate of two millet plants, represented in black and grey, during -0.35 MPa osmotic stress. The dark periods are presented as black bars in the figure.

DISCUSSION

NMR MICROSCOPY

The experimental results clearly demonstrate that low field NMR imaging is an attractive tool to study stress responses in the different tissues of intact plants. By combining NMR imaging with water uptake measurements, the effects of drought stress can be monitored from the tissue up to the whole plant level. The results of the non-stress experiments indicate that as long as plants are allowed to recover from transfer to the imager, the technique itself does not influence the plant response.

The reported NMR experiments took 15 minutes per measurement. Though this is slow compared to growth measurements with for example an electronic transducer,³¹ this time scale is sufficient to monitor the changes in relaxation times that occur during stress. When necessary, the time resolution can be further improved by decreasing the number of averages and the repetition time at the expense of the signal-to-noise ratio. Presently, the time resolution of an imaging experiment is limited to a few minutes for relaxation measurements and to less than a minute for a single-shot image. The considerations that apply for the time resolution are also valid for the spatial resolution, *i.e.* improvement of the resolution can be achieved at the expense of the signal-to-noise ratio and/or temporal resolution.

In our case we do not obtain resolution at the cellular level, but because the tissue is very homogeneous in the internodes, we can assume that in these tissues the signal within one pixel originates mainly from cells of similar dimensions, justifying an interpretation of the obtained information in terms of cell water balance. This is especially true for the transversal images, where an optimal resolution is obtained in the axial direction ($235 \times 235 \mu\text{m}$). The slice thickness is 3 mm, but since the longitudinal structure is very well preserved over the entire internode, every pixel consists mainly of the same tissue. The resolution of the longitudinal images is $390 \times 390 \mu\text{m}$, and here the slice thickness does result in sampling a mix of tissues per pixel (*e.g.* parenchyma and vascular tissue). However, all conclusions drawn in this paper apply for both transverse and longitudinal images, *i.e.* observed changes in NMR parameter occur in both types of measurements.

GROWTH AND WATER UPTAKE

The response of maize shoot growth to osmotic stress as observed by NMR is consistent with the inhibition of maize leaf and root elongation by water deficits as was observed previously.^{4,6,32} It has been suggested that the duration of the period of increased growth after stress is dependent on the duration of the preceding stress period, as has been observed for stress periods of 1 hour and 4 hours.³ This could account for the high growth rates for at least 48 hours after recovery started.

The applied osmotic solute (-0.35 MPa PEG solution) causes only mild osmotic stress considering the relatively small change in water uptake and the constant water density in the shoot for both maize and millet. However, for both species the expansion of the shoot apical cells is strongly inhibited (Figs. 5.11).

T_2 AND AMPLITUDE

Though the ability to measure stem growth is valuable in itself, the major advantage of NMR lies in the additional information that can be obtained from the images. The signal amplitude is in principle equal to the amount of protons per voxel. However, the relaxation time of proteins and water in the cell wall matrix is too short to be observed by conventional MRI experiments, which implies that usually only intracellular water is observed.²¹ Thus, the signal amplitude corresponds to the tissue water content times the tissue density.²⁰ The tissue water content is fairly homogeneous for the various organs, but appears to be the lowest in the leaves. The amplitude of the selected parenchyma tissue was constant during stress for both maize and pearl millet (Table 5.1), as well as the stem diameter, indicating that no noticeable dehydration nor cell shrinkage occurred under these conditions.

The relation between T_2 and compartment size (vacuole), based on the theory of Brownstein and Tarr, can indeed be observed in intact plants as well. Since there is a large variation in cell and vacuole size, this explains the large contrast in T_2 between the different plant tissues. When the relation between T_2 and cell size is known, the obtained T_2 values can be normalised on cell dimensions, thus revealing the role of the magnetisation sink, which is determined by the permeability of the tonoplast and plasmalemma, and the cytoplasm. On the other hand, knowing that T_2 increases with increasing cell size, allows to distinguish growth due to cell elongation from growth by cell division.

In the case of pearl millet, the observed increase in $1/T_2$ in vacuolised cells during stress is related to such a change in magnetisation sink, since the cell dimensions are constant. The sink strength density H could be calculated from Fig. 5.9 and corresponds to the transport of protons over the tonoplast, i.e. the tonoplast permeability for protons (free or in various molecules, mostly water), assuming a perfect relaxation sink outside the tonoplast membrane. In this *in vivo* situation, the relaxation sink outside the vacuole is clearly not infinite, since the relaxation rate in the cytoplasm is indeed much higher than in the vacuole, but not infinitely high. In practice this means that H will not only reflect the tonoplast permeability (for water and protons both), but also the relaxation properties of the cytoplasm and the plasmalemma permeability. The found increase in the relaxation sink for the vacuole of pearl millet can therefore be explained by either an increase in the tonoplast and/or plasmalemma permeability for water, or by changes in the cytoplasm as a decreased T_2 value in the cytoplasm due to accumulation of sugars or a thinner cytoplasmatic layer. However, we deem a change in

membrane permeability more likely than the other explanations, because most likely a decrease in cytoplasmatic T_2 for our low-field NMR measurements would require unrealistically large changes in solute concentrations.³³ At a magnetic field strength of 2 T, they measured the T_2 of kiwifruits in different stages of ripening. The observed relaxation remained unaltered, though the soluble solids content and the free sugar content increased by 68% and 200% respectively. At the lower magnetic field strength we used (0.5 T), the possible effect of solute concentrations will be even smaller.

A relation between T_2 and membrane permeability was found earlier in a heat stress study.³⁴ During drought stress, an increase in membrane permeability, especially in the plasmalemma, of the elongating internodes could be advantageous, because a higher hydraulic conductivity of the internodal tissue would facilitate water transport from other plant tissues to these young, growing parts, as was suggested in an earlier report.³⁵ One can wonder if aquaporins play an important role in this change in membrane transport properties, as they are thought to contribute to drought tolerance by facilitating water mobilisation towards critical cells and organs.^{36,37} Recently mRNA expression of a tonoplast aquaporin was found to increase during osmotic stress in cauliflower cells.³⁸

If so, a combination of different NMR approaches, would be useful to unravel the role of membrane transport properties in the hydraulics of the system at a higher scale (tissues and organs). By relating the parameters T_2 and amplitude, which provide information on the cellular level, with xylem and phloem flow measurements and with diffusion tensor imaging, to dissolve diffusion rates in all directions, *in vivo* information on water transport on different organisational levels is at hand.

In conclusion, maize and pearl millet differ significantly in the response to osmotic stress. Though the PEG stress the growth rate and water uptake of pearl millet are less affected than those of maize, the effect of stress on the cell water balance of millet is more pronounced. For the interpretation of the relaxation times, a model was used, which describes the relation between relaxation, compartment size and the relaxation sink. In this whole plant approach, the T_2 is indeed linearly related to compartment size. Since for this mild stress no changes in cell dimensions are observed, the observed decreases in T_2 in this plant point to an increase of the membrane permeability.

ACKNOWLEDGEMENTS

This Chapter has been published as:

Van der Weerd L., Claessens M.M.A.E., Ruttink T., Vergeldt F.J., Schaafsma T.J. & Van As H. (2001) Quantitative NMR microscopy of osmotic stress responses in maize and pearl millet. *Journal of Experimental Botany* **52**, 2333-2343.

The authors wish to thank W.H.L. van Veenendaal, J. Nijssse and A.C. van Aelst (Laboratory of Plant Cytology and Morphology) for help with the microscopical pictures.

REFERENCES

1. Boyer J.S. (1982) Plant productivity and environment. *Science* **218**, 443-448.
2. Turner (1997) Further progress in crop water relations. *Advances in Agronomy* **58**, 293-338.
3. Hsiao T. (1973) Plant responses to water stress. *Annual Reviews on Plant Physiology* **24**, 519-570.
4. Ribaut J.M. & Pilet P.E. (1991) Effects of water stress on growth, osmotic potential and abscisic acid content of maize roots. *Physiologia Plantarum* **81**, 156-162.
5. Acevedo E., Hsiao T.C. & Henderson D.W. (1971) Immediate and subsequent growth response of maize leaves to changes in water status. *Plant Physiology* **48**, 631-636.
6. Volkenburgh E.v. & Boyer J.S. (1985) Inhibitory effects of water deficit on maize leaf elongation. *Plant Physiology* **77**, 190-194.
7. Nonami H. & Boyer J.S. (1990) Primary events regulating stem growth at low water potentials. *Plant Physiology* **93**, 1601-1609.
8. Nonami H. & Boyer J.S. (1990) Wall extensibility and cell hydraulic conductivity decrease in enlarging stem tissues at low water potentials. *Plant Physiology* **93**, 1610-1619.
9. Premachandra G.S., Saneoka H., Kanaya M. & Ogata S. (1989) Responses of relative growth rate, water relations and solute accumulation to increasing water deficits in maize. *Journal of Plant Physiology* **135**, 257-260.
10. French J. (1997) Primary responses of root and leaf elongation to water deficits in the atmosphere and soil solution. *Journal of Experimental Botany* **48**, 985-999.
11. Ratcliffe R.G. (1994) *In vivo* NMR studies of higher plants and algae. Oxford, UK, Academic Press Limited.
12. MacFall J.S. & Van As H. (1996) Magnetic resonance imaging of plants. In: Nuclear magnetic resonance in plant biology (eds Shachar-Hill Y. & Pfeffer P.E.), 33-76. The American Society of Plant Physiologists.
13. Chudek J.A. & Hunter G. (1997) Magnetic resonance imaging of plants. *Progress In Nuclear Magnetic Resonance Spectroscopy* **1**, 43-62.
14. Ishida N., Koizumi M. & Kano H. (2000) The NMR microscope: A unique and promising tool for plant science. *Annals of Botany* **86**, 259-278.

15. Xia Y. & Callaghan P.T. (1992) "One-shot" velocity microscopy: NMR imaging of motion using a single phase-encoding step. *Magnetic Resonance In Medicine* **23**, 138-153.
16. Kuchenbrod E., Haase A., Benkert R., Schneider H. & Zimmermann U. (1995) Quantitative NMR microscopy on intact plants. *Magnetic Resonance Imaging* **13**, 447-55.
17. Kockenberger W., Pope J.M., Xia Y., Jeffrey K.R., Komor E. & Callaghan P.T. (1997) A non-invasive measurement of phloem and xylem water flow in castor bean seedlings by nuclear magnetic resonance microimaging. *Planta* **201**, 53-63.
18. Scheenen T.W.J., Van Dusschoten D., De Jager P.A. & Van As H. (2000) Microscopic displacement imaging with pulsed field gradient turbo spin-echo NMR. *Journal Of Magnetic Resonance* **142**, 207-215.
19. Ishikawa M., Price W.S., Ide H. & Arata Y. (1997) Visualization of freezing behaviors in leaf and flower buds of full-moon maple by nuclear magnetic resonance microscopy. *Plant Physiology* **115**, 1515-1524.
20. Donker H.C.W., Van As H., Snijder H.J. & Edzes H.T. (1997) Quantitative ¹H-NMR imaging of water in white button mushrooms (*agaricus bisporus*). *Magnetic Resonance Imaging* **15**, 113-121.
21. Van der Toorn A., Zemah H., Van As H., Bendel P. & Kamenetsky R. (2000) Morphological structure and water status in tulip bulbs from dormancy to active growth: Visualization by NMR imaging. *Journal of Experimental Botany* **51**, 1277-1287.
22. Brownstein K.R. & Tarr C.E. (1977) Spin-lattice relaxation in a system governed by diffusion. *Journal of Magnetic Resonance* **26**, 17-24.
23. Brownstein K.R. & Tarr C.E. (1979) Importance of classical diffusion in NMR studies of water in biological cells. *Physical Reviews A* **19**, 2446-2453.
24. Hills B.P. (1992) Dynamic q space microscopy of cellular tissue. *Molecular Physics* **76**, 979-994.
25. Snaar J.E.M. & Van As H. (1992) Probing water compartment and membrane permeability in plant cells by proton NMR relaxation measurements. *Biophysical Journal* **63**, 1654-8.
26. Hoagland D.R. & Arnon D.I. (1950) The water-culture method for growing plants without soil. *California Agriculture Experimental Station Circular* **347**.
27. Edzes H.T., Van Dusschoten D. & Van As H. (1998) Quantitative T₂ imaging of plant tissues by means of multi-echo MRI microscopy. *Magnetic Resonance Imaging* **16**, 185-196.
28. Donker H.C.W., Van As H., Edzes H.T. & Jans A.W.H. (1996) NMR imaging of white button mushroom (*agaricus bisporus*) at various magnetic fields. *Magnetic Resonance Imaging* **14**, 1205-1215.
29. Van der Weerd L., Vergeldt F.J., De Jager P.A. & Van As H. (2000) Evaluation of algorithms for analysis of NMR relaxation decay curves. *Magnetic Resonance Imaging* **18**, 1151-1157.
30. Whaley W.G. (1961) Growth as a general process. In: *Handbuch der pflanzenphysiologie* 14 (eds Ruhland W.), 71-112. Springer Verlag, Berlin.
31. Lu Z.J. & Neumann P.M. (1999) Water stress inhibits hydraulic conductance and leaf growth in rice seedlings but not the transport of water via mercury-sensitive water channels in the root. *Plant Physiology* **120**, 143-151.

32. Chazen O., Hartung W. & Neumann P.M. (1995) The different effects of peg 6000 and nacl on leaf development are associated with differential inhibition of root water transport. *Plant, Cell and Environment* **18**, 727-735.
33. Clark C.J., Drummond L.N. & MacFall J.S. (1998) Quantitative nmr imaging of kiwifruit (*actinidia deliciosa*) during growth and ripening. *Journal of the Science of Food and Agriculture* **78**, 349-358.
34. Maheswari M., Joshi D.K., Saha R., Nagarajan S. & Gambhir P.N. (1999) Transverse relaxation time of leaf water protons and membrane injury in wheat (*triticum aestivum* L.) in response to high temperature. *Annals of Botany* **84**, 741-745.
35. Van As H., Nagarajan S., Van Dusschoten D. & Vergeldt F. (1995) Functional NMR imaging of osmotic stress in pearl millet and maize. *Plant Physiology* **108**, 40.
36. Maurel C. (1997) Aquaporins and water permeability of plant membranes. *Annual Review Of Plant Physiology And Plant Molecular Biology* **48**, 399-429.
37. Tyerman S.D., Bohnert H.J., Maurel C., Steudle E. & Smith J.A.C. (1999) Plant aquaporins: Their molecular biology, biophysics and significance for plant water relations. *Journal of Experimental Botany* **50 Special Issue**, 1055-1071.
38. Barrieu F., Marty M.-D., Thomas D., Chaumont F., Charbonnier M. & Marty F. (1999) Desiccation and osmotic stress increase the abundance of mRNA of the tonoplast aquaporin BOBTIP26-1 in cauliflower cells. *Planta* **209**, 77-86.

6

NMR IMAGING OF MEMBRANE PERMEABILITY CHANGES IN PLANTS DURING OSMOTIC STRESS

*The cell water balance of maize (*Zea mays* L., cv LG 11) and pearl millet (*Pennisetum americanum* L., cv MH 179) during osmotic stress has been studied non-invasively using ^1H NMR microscopy. Single NMR parameter images of (i) the water content, (ii) the transverse relaxation time (T_2) and (iii) the apparent diffusion coefficient (D_{app}) were used to follow the water status of the stem apical region during osmotic stress. During stress there are hardly any changes in water content or T_2 of the stem region of maize. In contrast, the apical tissue of pearl millet showed a ~30% decrease of T_2 within 48 hours of stress, whereas the water content and D_{app} did not change. These changes can be explained by an increase of the membrane permeability for water. This conclusion is supported by results from scanning electron microscopy, relaxation measurements of sugar solutions and numerical simulations of a plant cell.*

INTRODUCTION

One of the intriguing questions in agricultural research is how plants handle drought stress. Plants show numerous adaptive responses to water deficits: inhibited growth, stomatal closure, osmotic adjustment and changes in hydraulic tissue conductance.¹⁻⁵ All these processes are connected to water transport across cellular barriers. Water permeability of cellular membranes is therefore of fundamental importance to understand the physiological response of plants to drought.

There are currently two opposite views on the role of membrane permeability during drought stress. The first predicts a higher membrane permeability and facilitated water transport *e.g.* to maintain expansion growth during stress or to facilitate rehydration of tissues.^{6,7} The second is exactly the opposite, *i.e.* drought stress induces a decreased membrane permeability to preserve cellular water within the tissues.^{8,9}

Most research on membrane permeability is focused on the role of aquaporins, or membrane water channels. During drought stress both upregulation and downregulation of aquaporin gene expression seem to occur, depending on which kind of plant and organ is involved.⁵ Some reports claim to have found an even more complicated regulation mechanism in which some aquaporin genes show enhanced expression whereas others are downregulated in the

same organ.⁵ However, the effect of those gene regulations on the actual membrane permeability and the hydraulic tissue conductance is not known in detail.

The recent discovery of aquaporin and non-aquaporin water channels has triggered the development of instrumental methods to measure water permeability, *e.g.* light scattering, fluorescence and gravimetric methods (for a review see Verkman¹⁰). These techniques are limited to a few cell layers at the periphery of the tissue. The frequently used cell pressure probe does not have this drawback, but its application is limited to a single cell and to a limited time span.¹¹ In contrast, Nuclear Magnetic Resonance (NMR) imaging uniquely depicts the internal anatomical details for the entire tissue of interest. In addition, the spatial distribution of water, and physical properties such as mobility within the plant tissue are obtained.

Membrane permeability is frequently determined using the NMR relaxation times of intracellular water protons.¹²⁻¹⁶ According to the Brownstein and Tarr (B-T) model,^{12,17} the observed transverse relaxation time T_2 of water in a confined compartment can be described as a function of the bulk T_2 ($T_{2,bulk}$), the radii of the compartment along the x , y and z directions ($R_{x,y,z}$) and the rate of wall relaxation or surface sink strength density (H):

$$1/T_{2,obs} = H(1/R_x + 1/R_y + 1/R_z) + 1/T_{2,bulk} \quad [6.1]$$

In principle, the B-T model can be applied to vacuolised plant cells, with the vacuole as the main (largest) compartment with a relatively long bulk relaxation time. The cytoplasm and apoplast have a much shorter relaxation time and act therefore as a magnetisation sink for the vacuole. The water permeabilities of the tonoplast (P_{ton}) and the plasmalemma (P_{pl}) membranes determine the exchange rates of water between these compartments. The combination of the extra-vacuolar magnetisation sink and the membrane permeabilities determine the final sink strength density H in Eqn. 6.1.

This paper reports the application of NMR imaging to maize and pearl millet plants during drought stress. Maize and pearl millet were chosen because of their different physiological response to drought stress.^{18,19} In our experiments the transverse relaxation time T_2 was combined with the apparent diffusion coefficient (D_{app}) in stem parenchyma tissue to elucidate the influence of drought stress on the membrane permeability as described in Chapter 5.

MATERIALS AND METHODS

PLANT MATERIAL

Maize (*Zea mays L.*, cv LG 11) and pearl millet (*Pennisetum americanum L.*, cv MH 179) seeds were germinated in wet sand in the dark. After one week the seedlings were transferred to water culture with half Hoagland nutrient solution,²⁰ which was refreshed every week. All plants were grown in separate vessels, designed to fit in the NMR imager to prevent root damage when the plants were transferred. The plants were grown in a phytotron at 25 °C and 70% relative humidity with a photoperiod of 16 hours and a light intensity of 40 W m⁻² (mercury vapour lamp). When used, the plants were 4 or 6 weeks old, with 6 or 9 fully emerged leaves, respectively.

NMR IMAGING EXPERIMENTS

(i) T_2 and cell size. The stems of maize (N=4) and pearl millet (N=5) were imaged from the shoot apex down over a length of about 20 cm under normal, non-stress conditions. The same plants were used for light microscopy to determine the parenchyma cell dimensions in the different internodes.

(ii) Stress conditions. NMR imaging of the shoot apical region of maize (N=2) and pearl millet (N=3) was combined with water uptake measurements. The plants were followed for six days: the first two days under normal conditions, the second two days during osmotic stress and the third two days during recovery. For pearl millet part of the experiment was repeated (N=2), recording NMR imaging data under the initial, normal conditions and after 48 hours of osmotic stress. Osmotic stress was applied by replacing the normal root medium by a -0.35 MPa solution of Polyethylene Glycol (PEG 6000, 162.3 g kg⁻¹) in nutrient medium. The shoot of the plant was housed in a climate chamber with an air temperature of 26 ± 1 °C and a relative humidity of 50 ± 2% with a photoperiod of 16 hours and a light intensity of 70 W m⁻².

The NMR spectrometer was a 20.35 MHz imager consisting of a 0.47 T Bruker electromagnet (Karlsruhe, Germany) controlled by a S.M.I.S. console (S.M.I.S., Guildford, England). A shielded gradient probe with a vertical open cylindrical access of 45 mm was used (Doty Scientific Inc., Columbia, South Carolina, USA). T_2 values were measured every hour using a multi-spin-echo imaging pulse sequence with slice selection,^{21,22} a repetition time (TR) of 1800 ms, a spin-echo time (TE) of 4.3 ms and a spectral bandwidth of 50 kHz. A 128 × 128 matrix of complex data points was acquired per echo, and typically 64 echoes were acquired per echo train. For each image four acquisitions were averaged to improve the image quality, resulting in a total scan time of 15 minutes per image. The field-of-view was 50 mm, and the slice thickness 3.0 mm. A PFG TSE sequence was used to obtain the apparent

diffusion coefficient (D_{app}).²³ The displacement encoding parameters were $\delta = 3$ ms, $\Delta = 24$ ms, and a maximum gradient strength of 0.38 T m^{-1} .

The NMR data sets were analysed by home-written calculation routines in IDL (Research Systems Inc., Boulder, Colorado, USA). The multi-echo images were fitted on a pixel-by-pixel base using a mono-exponential decay function, yielding quantitative amplitude and $1/T_2$ images.^{21,22} After phase correction, the real part of the signal was used for analysis.²⁴ Mean tissue parameters were obtained by averaging 9 adjacent pixels in the centre of an internode.

LIGHT MICROSCOPY AND CRYO -SEM MICROSCOPY

The same plants as used for NMR imaging (i) were also used to determine the cell dimensions. Fresh longitudinal sections of the internodes were prepared using a hand microtome and fixed on a microscope slide using Kayser's glycerol gelatine (Merck 9242, Darmstadt, Germany). The slices were several cell layers thick; average cell sizes for the individual plants were determined by focussing the microscope on a central cell layer and measuring 60 randomly selected cells in two dimensions for every internode by hand. The length and position of each section was measured to correlate the results to the NMR images. In addition, longitudinal sections were made of three other millet plants, which had been under stress conditions for two days. Cell dimensions were determined of internodes of 1-cm length and compared with comparable internodes of non-stressed plants.

For Cryo Scanning Electron Microscopy, internodes of 1-cm length of both plants were cut into longitudinal slices with a razor blade, subsequently plunged in liquid propane and then stored in liquid nitrogen. The slices were fractured at -88°C and freeze-etched for three minutes in an Oxford CT 1500 HF cryo transfer unit and sputter coated with 10 nm platinum. The cut surface was studied with a JEOL 6300F field emission scanning electron microscope at -194°C at 2.5 kV.

OSMOTIC POTENTIAL

Frozen-thawed samples of 3 millet internodes before and 3 internodes after 48 hours osmotic stress were squeezed. The fluid was collected and analysed with an osmometer (Vogel Roebling).

SUGAR SOLUTIONS

To evaluate the effect of increasing solute concentrations on the observed T_2 , solutions containing sugars typically found in plants were prepared in distilled water. The following solutions were prepared: glucose 5% and 10% (w/v) at pH 6; sucrose 5% and 10% (w/v) at pH 6; sucrose 10% (w/v) at pH 4; 100mM NaCl + 1% (w/v) sucrose at pH 6; 200mM NaCl + 2% (w/v) sucrose at pH 6. The transversal relaxation was measured using a CPMG pulse

sequence on a MARAN system (Resonance Instruments), with an interecho time of 4 ms. The T_2 for each sample was determined using SPLMOD software.²⁵

NUMERICAL SIMULATIONS

A finite difference numerical model of multi-compartment systems with cylindrical geometry was used that was based on the evaluation of Fick's second diffusion law.²⁶ Using this model, the signal amplitude and phase can be calculated for any combination of intrinsic compartment parameters at any time point during the gradient pulses and diffusion time, and during the decay time following the PFG part of a PFG-CPMG experiment. Random noise (S/N 10000) was generated to avoid fitting problems.

A typical PFG-CPMG experiment was simulated, with 16 gradient steps, 200 echoes and 5 ms interecho time. The resulting two-dimensional data sets were fitted with a coupled fitting routine; first a mono-exponential fit was applied to the relaxation part using SPLMOD,²⁵ and subsequently the fitted intensity was used to fit the corresponding diffusion fraction.²⁷

RESULTS

Maize and pearl millet plants are well known to have different drought stress responses. The maize variety used in our experiments is not very drought tolerant, but we observe almost no response to osmotic stress. The only visible reactions to osmotic stress all occur in the leaves, which start to roll and become necrotic. A more severe osmotic stress (-0.9 MPa PEG 6000) causes the leaves to become necrotic and irreversibly damaged after two days (Chapter 7). Pearl millet, an important African and Asian food crop, shows wilting leaves and stem shrinkage after severe stress, but recovers completely when normal conditions are restored.²⁸ In our experiments the application of low osmotic stress (-0.35 MPa) does not result in such obvious visible changes, but is severe enough to stop stem elongation almost completely during the stress period.¹⁶

NMR IMAGING OF THE STEM APICAL REGION

Maize and pearl millet plants were continuously imaged during the cycle: 2 days under normal conditions - 2 days under osmotic stress - 2 days under normal conditions. A selection of the amplitude and $1/T_2$ images of the results of these measurements is shown in Figs. 6.1 and 6.2. For both plants the apex is clearly visible (a) as are the youngest internodes below the shoot apex (b), separated by the nodes (c). The leaves that surround the stem are visible on both sides of the shoot (d). The amplitude images show far less contrast, because of a fairly uniform water content and tissue density for different plant tissues. More details on the anatomy and growth of the apical region can be found in a previous paper.¹⁶

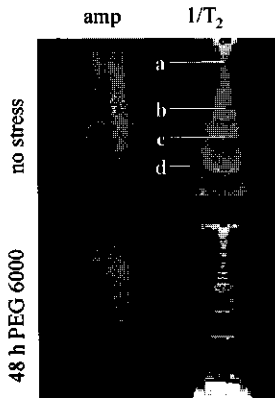


Figure 6.1. Amplitude and $1/T_2$ images of a maize plant recorded before and after 48 hours of -0.35 MPa osmotic stress; a-d mark different internode regions, discussed in the text.

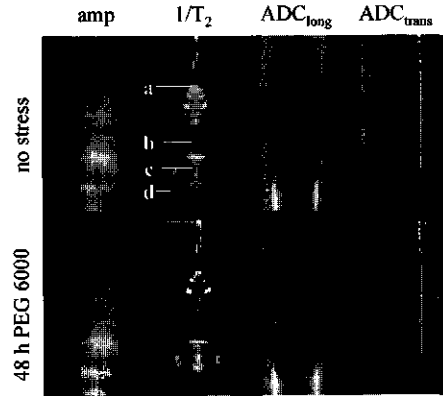


Figure 6.2. Amplitude, D_{app} and $1/T_2$ images of a millet plant recorded before and after 48 hours of -0.35 MPa osmotic stress; a-d mark different internode regions, discussed in the text.

The parenchyma cells within the central part of the internodes are fairly homogeneous in cell size and completely vacuolised; the cell dimensions increase per internode from top to bottom.¹⁶ D_{app} is dependent on both the bulk diffusion coefficients and the compartment dimensions, which explains the different values obtained for the different internodes: the larger the cells, the higher D_{app} will be. The two different D_{app} images reflect the diffusion coefficients in the longitudinal and transversal plane, respectively. Since the plant cells can often approximately cylindrical, the cell radius depends on the direction, and so does the diffusion coefficient as observed by the NMR method. This can be seen most clearly in the long, thin fibrous cells at the edge of the internodes, which have a very high diffusion coefficient along the long axis of the cells, and a very short D_{app} in the transversal plane. According to Eqn. 6.1, the observed transverse relaxation rate $1/T_{2,obs}$ is expected to depend on the dimensions of the vacuole. Figs. 6.1 and 6.2 indeed show a large variation in T_2 between the various internodes, which could be contributed to the different cell dimensions in these tissues. To verify whether this theoretical relation also holds for intact plants, maize and pearl millet plants were imaged from the shoot apex down to the roots. In Fig. 6.3, the $1/T_2$ values of the various internodes of a number of non-stressed plants (obtained from NMR images as shown in Figs. 6.1 and 6.2) are presented as they vary with the cell size, determined afterwards by optical microscopy of the same plants. Clearly a linear correlation between cell dimensions and $1/T_2$ is demonstrated, that holds for a large range of cell sizes. The intercept of the fitted line in Figure 6.3 corresponds to the $T_{2,bulk}$ of the vacuole, which is in this case

around 2 s, as expected close to the T_2 of free water.¹⁴ According to Eqn. 6.1, the slope of the line corresponds to the sink strength parameter H , yielding $H = (2.8 \pm 0.52) \times 10^{-5} \text{ m s}^{-1}$ for maize and $(4.0 \pm 0.44) \times 10^{-5} \text{ m s}^{-1}$ for millet.

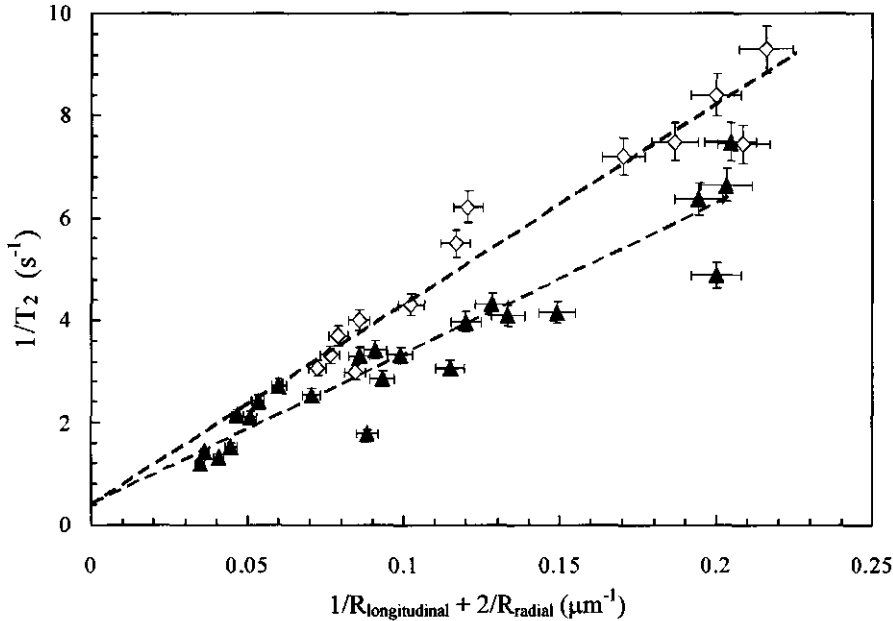


Figure 6.3. Relation between relaxation time T_2 and the cell dimensions for maize ($n=4$, \blacktriangle) and pearl millet ($n=5$, \diamond). The data points are taken from different internodes in the NMR images. Following the NMR measurements, the same plants were used for microscopic sections to determine the cell dimensions.

NMR IMAGING DURING OSMOTIC STRESS

The stem apical region was measured continuously during the six-day experiment, and average tissue parameters were calculated for the central part of the 1-cm length internode of each of the plants. The $1/T_2$ values for one maize and one pearl millet plant are shown in Fig. 6.4; the other plants showed similar trends. Clearly, the internodal stem tissue of the maize plant does not show any changes in relaxation rate. Moreover, the signal amplitude and apparent diffusion coefficient remain constant during the entire stress period (Table 6.1). Pearl millet on the other hand shows a response within hours of the onset of stress. After about 10 hours of stress the transverse relaxation rate starts to increase, up to 130% of the initial value after two days of osmotic stress (Fig. 6.4). Despite this increase of $1/T_2$, the amplitude images did not show any decrease in water density or in stem diameter (Table 6.1), indicating that the stem tissue did not noticeably dehydrate.

According to Eqn. 6.1, the relaxation rate depends on several parameters, *i.e.* the cell dimensions, the tonoplast and plasmalemma permeability, and the bulk relaxation properties

in the different compartments. The initial cell dimensions in the selected tissue can be calculated from Fig. 6.3; using $H = 4.0 \times 10^{-5} \text{ m s}^{-1}$ for pearl millet, the inverse of the cell size R for the millet plant in Fig. 6.4 is found to be $0.22 \mu\text{m}^{-1}$, using $1/R = (1/R_{\text{longitudinal}} + 2/R_{\text{radial}})$. The cell dimensions of the other plants varied depending on the length of the used internode. Assuming that the cell dimensions did not change during stress (see next section), the calculated dimensions were used to determine the sink strength parameter H during the stress period for all maize and millet plants (Fig. 6.5). During the two-day stress period all pearl millet plants showed the same pattern: a constant or slightly decreasing H value during the first hours of stress, after which it starts to increase to about $130\% \pm 9\%$ of the original value after two days.

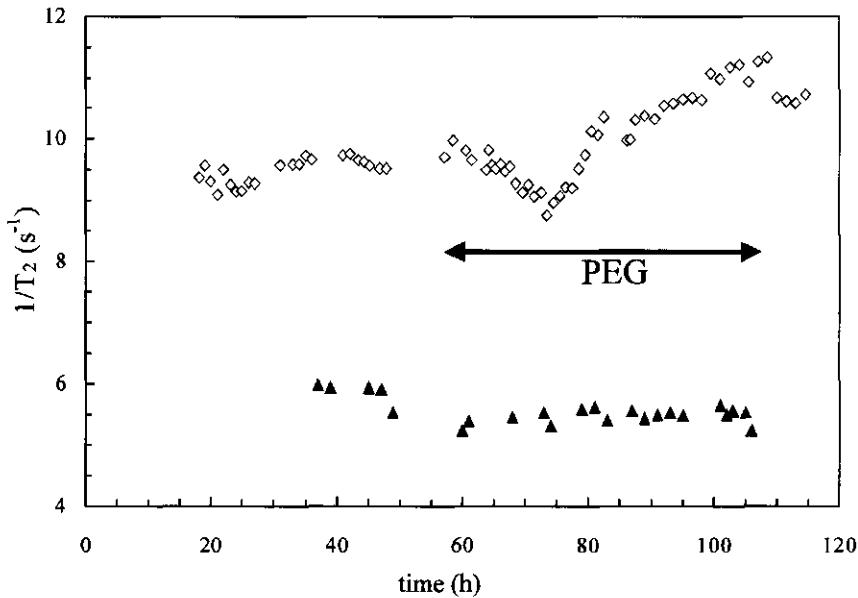


Figure 6.4. Relaxation rates for maize (\blacktriangle) and pearl millet (\diamond) of stem parenchyma tissue before and during -0.35 Mpa osmotic stress. The data shown are the mean of nine voxels taken from longitudinal images shown in Figs. 6.1 and 6.2.

PEG (h)	Maize		Pearl Millet			
	Amplitude (a.u.)	$1/T_2$ (s^{-1})	Amplitude (a.u.)	$1/T_2$ (s^{-1})	$D_{\text{app,long}}$ ($10^{-9} \text{ m}^2 \text{ s}^{-1}$)	$D_{\text{app,trans}}$ ($10^{-9} \text{ m}^2 \text{ s}^{-1}$)
0	1	5.72 ± 0.28	1	4.29 ± 0.13	1.18 ± 0.12	0.994 ± 0.10
48	0.97 ± 0.04	5.43 ± 0.18	1.02 ± 0.03	5.32 ± 0.28	1.09 ± 0.09	1.08 ± 0.013

Table 6.1. NMR amplitude, $1/T_2$ and D_{app} before and after 48 hours of -0.35 Mpa osmotic stress. The presented values are the mean of nine voxels taken from the longitudinal images as shown in Figs. 6.1 and 6.2.

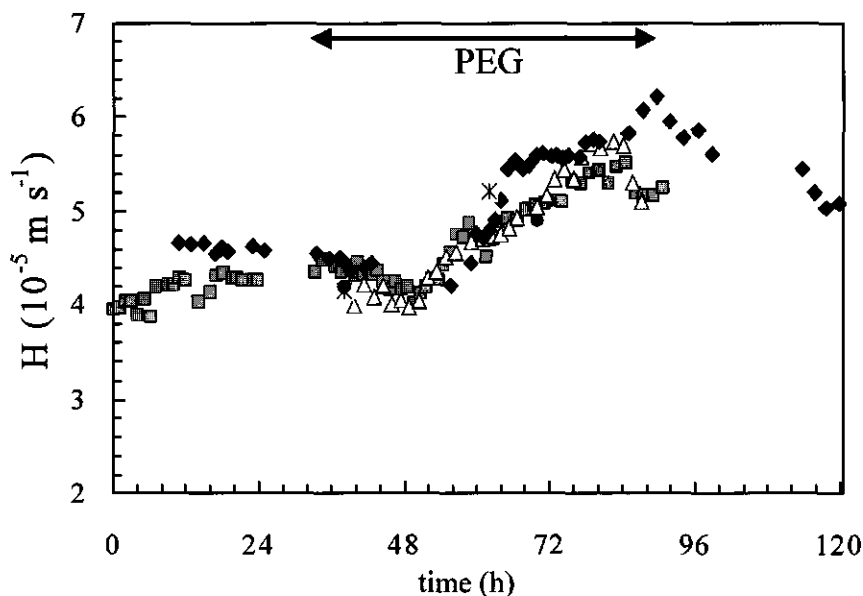


Figure 6.5. The sink strength parameter H for five different millet plants during osmotic stress. The various symbols (■, ×, ◆, △, ●) depict different individual plants. H is calculated using Eqn. 6.1. $1/T_2$ was used as shown in Fig. 6.4, and the cell dimensions were determined from the data in Fig. 6.3.

SEM

Several assumptions were made for the calculation of H from Eqn. 6.1. The first is that the cell dimensions remain constant during the entire stress period. From the amplitude images we already concluded that the amount of water and the diameter of the stem do not change. Some additional experiments were done to look at the cell size in millet plants in greater detail. Longitudinal slices of the 1-cm-length internode of three millet plants were used for Scanning Electron Microscopy (SEM) to determine the volume fraction of the vacuole within the cell (Fig. 6.6, Table 6.2). From this Figure it is clear that the cells are completely vacuolised, and the vacuole comprises by far the largest volume in the cell. Furthermore, the parenchyma tissue appears to be very homogeneous. Since the slices are cut through different planes of the approximately cylindrical cells, the cell cross-sectional area cannot be determined quantitatively. However if cell shrinkage occurs a change in the vacuole/cytoplasm volume ratio is expected, since the vacuole acts as a buffer compartment to compensate water losses from the cytosol. Plants that were subjected to two days of -0.35 MPa PEG stress before freezing the internodial tissue showed no differences in appearance or in vacuole volume fractions. Optical microscopy of stressed plants showed no significant difference in cell dimensions with respect to non-stressed plants (Table 6.2).

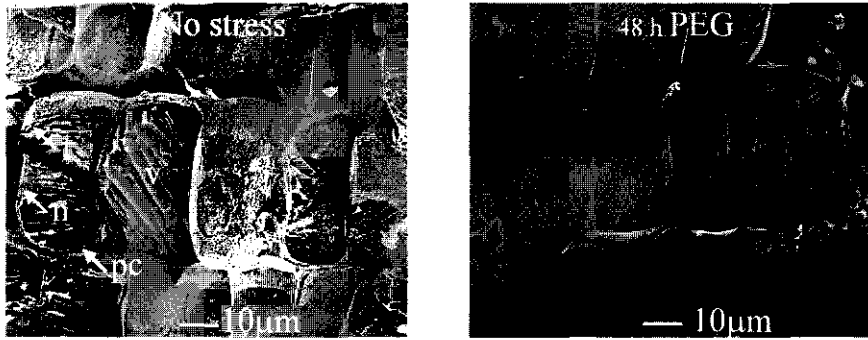


Figure 6.6. Cryo-SEM section of millet parenchyma cells before and after 48 hours of -0.35 MPa osmotic stress. *v* = vacuole, *t* = tonoplast membrane, *pc* = plasmalemma and cell wall, *n* = nucleus.

PEG (h)	Vacuole area (%)	Cross-sectional cell area (μm^2)	Osmotic potential (mOsm kg^{-1})
0	93 ± 2.8	917 ± 138	290 ± 4
48	92 ± 2.8	869 ± 123	323 ± 2

Table 6.2. Vacuolar area relative to the total cell area, cross-sectional cell area and osmotic potential of pearl millet before and after 48 hours of -0.35 MPa osmotic stress.

BULK RELAXATION

Apart from the cell dimensions, the observed transverse relaxation time is also influenced by the bulk T_2 of the different compartments, which determines $T_{2,bulk}$ of the vacuole (Eqn. 6.1), and the efficiency of the cytoplasmatic and extracellular relaxation sinks. The bulk relaxation rate within the different compartments is determined by the presence of paramagnetic ions and by the proximity of solid surfaces or slowly moving macromolecules.^{30,31} In plant tissue the vacuole mainly accumulates sugars and ions, but contains no macromolecules and usually only very limited amounts of paramagnetic ions, such as Fe^{2+} , Cu^{2+} , Mn^{2+} .³² Therefore, the bulk T_2 of this compartment will be close to that of free water, around 2 s.^{14,16} This can also be seen in Fig. 6.3, where the axis intercept corresponds to $1/T_{2,bulk}$, i.e. 0.5 s^{-1} .

We determined the osmotic potential of stressed and non-stressed parenchyma tissue of millet to see if solute concentrations changed during stress, thereby possibly causing a change in bulk relaxation properties (Table 6.2). During stress the osmotic potential of millet parenchyma tissue increased by 11%, a significant osmotic adjustment, which corresponds to a 0.1 ± 0.002 MPa increase in osmotic pressure.

Clark and MacFall already showed that increases of 200% in free sugar concentrations in kiwi fruit did not result in any changes in the observed relaxation times in ripening kiwifruit at a 2 T imaging system. At the lower magnetic field strength of 0.5 T in our experiments, the influence of sugars on relaxation times due to proton exchange is expected to be even less than at high magnetic field strengths; therefore a possible osmotic solute accumulation during stress will not cause a significant change in the bulk relaxation properties. To verify this, transverse relaxation times were determined for 5% and 10% glucose and sucrose solutions at pH 6. In plants grown on nutrient medium, sugars account for about 28% of the total osmolality of the vacuole (around 300 mOsm kg⁻¹), which is much lower than for a 10% solution.²⁹ A 10% sucrose solution was also measured at pH 4, to observe the effect of fast proton exchange.³⁰ Furthermore, more realistic solutions of (100 mM NaCl + 1% sucrose) and (200 mM NaCl + 2% sucrose) were measured at pH 6 to determine the effects of non-paramagnetic ions on T_2 . The resulting relaxation times only show a very weak dependence on concentration and pH (Fig. 6.7), indicating that changes in T_2 due to osmotic adjustment can be safely ruled out.

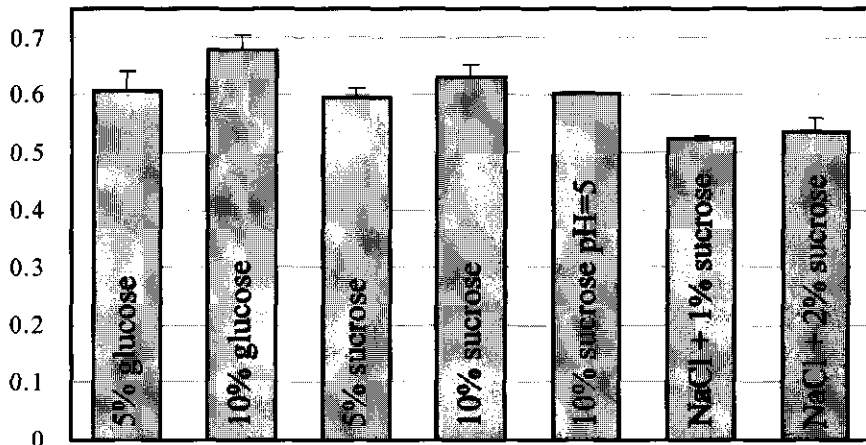


Figure 6.7. $1/T_2$ values for different sugar solutions. Unless stated otherwise all measurements were done at pH 6.

FREEZING

To demonstrate that the membranes indeed control the exchange of water between compartments and therefore the relaxation rate, we excised small pieces of internodal tissue and measured both T_2 and the apparent diffusion coefficient D_{app} for the entire sample. Next, the samples were frozen in liquid nitrogen, thawed and measured again. The results were analysed with two exponentials reflecting different compartments or tissue inhomogeneity.

	$1/T_{2,1}$	$1/T_{2,2}$	$D_{trans,1}$	$D_{trans,2}$
Fresh	2.76 ± 0.017	7.17 ± 0.093	1.13 ± 0.024	0.575 ± 0.016
Frozen	4.86 ± 0.031	9.68 ± 0.123	1.70 ± 0.031	1.56 ± 0.022

Table 6.3. Relaxation rates and D_{app} of excised millet internodal tissue, fresh and after freeze thawing. The decay curve of the sample was fitted bi-exponentially.

Both relaxation rates ($1/T_2$) increased after freeze thawing, due to membrane damage (Table 6.3), as was expected from the theory described above. D_{app} increased as well, because the maximum diffusion distance increased when the membranes separating the compartments were damaged.

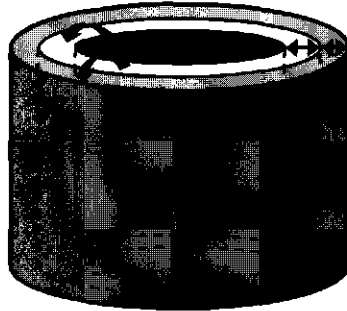
NUMERICAL SIMULATIONS

A numerical model of a cylindrical plant cell was used to simulate the experimental results (Fig. 6.8). The vacuole diameter was chosen in accordance with the results from optical microscopy and SEM. The thickness of the cytoplasmatic and cell wall layers is much smaller than that of the vacuoles. $T_{2,bulk}$ and D_{bulk} for every compartment were chosen in accordance with literature.^{14,27} The tonoplast permeability (P_{ton}) was set at a ten times higher value than the plasmalemma permeability (P_{pl}), as is reasonable for a plant cell.^{11,33}

We considered an individual cell in the simulations, so the outer boundary was closed. It should be noted that though the quantitative values for the output T_2 and D_{app} depend on the chosen variables, the qualitative trends we present here are found to be insensitive to the chosen set of parameters. Using the set of input parameters as in Fig. 6.8, a typical two-dimensional PFG-CPMG data set was generated and analysed using a mono-exponential coupled fit to extract the relaxation time and D_{app} values (Table 6.4, Start). D_{app} corresponds well to the experimentally found value (Table 6.1). The relaxation rate calculated using our model system is lower than in the experiment, which can be explained by the cylindrical shape of the cells in the model system, as compared to the ellipsoid-like shape of the parenchyma cells. This discrepancy does not invalidate the interpretation of the observed trends of the model calculations, however.

During osmotic stress, several events may occur at the cellular level. First, the vacuolar radius may decrease due to dehydration. This results indeed in an increase in $1/T_2$ as experimentally observed, but the simulation shows that the decreased cell dimensions also causes a lower D_{app} due to increased restriction and a large decrease in the signal amplitude, since the amount of water in the cell diminished (Table 6.4). Therefore, the predicted effects of cell shrinkage do not correspond to the actual experimental results. Alternatively, there may be an increase of either the tonoplast or the plasmalemma membrane permeability.^{6,7}

The simulated relaxation rate is indeed sensitive for both permeabilities, but the effect of increased plasmalemma permeability is much larger. The apparent diffusion coefficient D_{app} and the NMR signal amplitude however are predicted to remain approximately constant (Table 6.4), which is exactly what is observed experimentally (Table 6.1).



	vacuole	cytoplasm	cell wall
R (μm)	$R_{vac} = 15$	$R_{cyt} = 1.0$	$R_{cw} = 1.0$
T_2 (s)	$T_{2,vac} = 2.0$	$T_{2,cyt} = 0.1$	$T_{2,cw} = 0.01$
D ($10^{-9} \text{ m}^2 \text{ s}^{-1}$)	$D_{vac} = 2.0$	$D_{cyt} = 1.0$	$D_{cw} = 0.1$
P (10^{-4} m s^{-1})	$P_{ton} = 1.5$	$P_{pl} = 0.3$	$P_{out} = 0$

Figure 6.8. Schematic representation of the numerical model of a plant cell. All bulk parameters for the different compartments are shown below. R_{cyt} and R_{cw} are defined as the intermembrane distance.

	$1/T_2$ (s^{-1})	D_{app} ($10^{-9} \text{ m}^2 \text{ s}^{-1}$)	Amplitude (% of input)
Start	3.61	1.08	90.5
$P_{ton} \times 3.3$	3.95	1.10	91.1
$P_{pl} \times 2.2$	4.63	1.09	91.6
$P_{vac} \times 0.8$	4.51	0.966	62.0

Table 6.4. Amplitude, relaxation rates and apparent diffusion coefficients (D_{app}) of numerically simulated data sets. An isolated plant cell was modelled as in Fig. 6.8 and the different parameters were varied to evaluate the effect of osmotic stress.

DISCUSSION

IMAGING

The experimental results clearly show that NMR imaging is an attractive tool for *in vivo* plant studies. The resolution of the NMR images here is not high enough to distinguish individual cells, but the internodal tissue is very homogeneous. Therefore we can assume that the signal within a single pixel originates from cells of similar dimensions, which allows us to interpret the changes in terms of cell water balance.¹⁶ Previous experiments already showed that during osmotic stress no dehydration of apical stem tissue occurred for moderate osmotic stress, though stem elongation growth stopped almost completely.¹⁶ Therefore the cell dimensions do not increase due to growth during the stress period, which simplifies the interpretation of the results.

In principle, the signal amplitude equals the amount of protons present per voxel. Because the protons in plant tissue originate mainly from water molecules, the amplitude represents the tissue density multiplied by its water content, which is approximately equal to the amount of intracellular water.²¹ Since the amplitude images of maize and millet (Figs. 6.1 and 6.2) did not show any changes in intensity or in the stem diameter during the stress period we may safely conclude that the cell volume did not decrease by more than 3-4% (or 1.5% radius), which is the accuracy of the amplitude measurements. The SEM pictures of millet, which did not show any changes in vacuolar volume during stress, support this conclusion. In principle this means that very small volume changes may occur, which we are not able to resolve with the current techniques. However, to explain the found increase in $1/T_2$ in terms of a decrease in vacuole dimensions, the cell radius would need to change by about 25% (Eqn. 6.1), implying a volume change of a factor 2, which is clearly not the case.

Furthermore, the results of the measured sugar solutions imply that osmotic adjustment does not result in large changes in $T_{2,bulk}$. From Fig. 6.7 we conclude from the results of the NaCl + sucrose solutions (which is the closest to the *in vivo* vacuole solution) that $T_{2,bulk}$ should not be expected to reduce to values lower than 1.8 s. In the actual situation $T_{2,bulk}$ only contributes for 5 - 10% to the observed T_2 (Fig. 6.4). Therefore, according to Eqn. 6.1, the observed increase in $1/T_2$ should be caused by an increase in H . Numerical simulations of a plant cell confirm this conclusion.

MEMBRANE PERMEABILITY

The linear relation between T_2 , permeability and compartment size is in agreement with common relaxation theories^{12,13} and should hold for $rP/D_{bulk} < 10$. For cells of the 1-cm-length internode, with a radius of approximately 15 μm and a bulk diffusion coefficient of $2 \times 10^{-9} \text{ m}^2 \text{ s}^{-1}$, $rP/D < 10$ for a tonoplast permeability $< 1.3 \times 10^{-3} \text{ m s}^{-1}$, which generally applies to such tissue.³³ The general B-T theory assumes an infinite volume outside the main

compartment, acting as a sink, *i.e.* the $T_{2,bulk}$ of the cytoplasm should be infinitely short. Of course this is not correct for plant tissue. Therefore, H reflects the net magnetisation loss at the tonoplast, including the membrane permeability for water, the effective relaxation within the cytoplasm and the partial backflux of magnetisation from the cytoplasm into the vacuole. Consequently, the apparent magnitude of H (H_{app}) underestimates the tonoplast permeability; however, H_{app} is still linearly related to the actual membrane permeability (Chapter 4). The effective cytoplasmic relaxation also includes the probability for (water)proton spins to reach the plasmalemma, spin-exchange over the plasmalemma, and spin-relaxation within the cell wall. The probability to reach the plasmalemma is given by the ratio between the diffusion time to cross the cytoplasmic layer ($t_{diff} = R^2/2D$) and the bulk transverse relaxation time in the cytoplasm: $(R_{cyt}^2/2D_{cyt}) / T_{2,cyt}$. Using the same values as in the numerical simulations this ratio approximately equals 200. This means that the majority of the spin bearing molecules that cross the tonoplast also reach the plasmalemma before losing their magnetisation. Therefore, the quantitative value of the sink strength parameter H reflects both the tonoplast and plasmalemma permeabilities. This leads to two important conclusions. Firstly, it implies that relative changes in the membrane permeability can indeed be determined from changes in T_2 . Secondly the linear relation shown in Fig. 6.3 can be used to compare different plants of a particular variety, irrespective of the exact cell dimensions, since the known H value for non-stressed plants can be used to calculate the cell dimensions.

Measurement of the diffusional membrane permeability with most conventional techniques is based on the determination of concentration gradients and therefore is usually complicated by the presence of unstirred layers.^{10,11} This is indeed true if molecules as those of heavy water or ions are used as a tracer, because the concentrations of those molecules on either side of the membrane greatly depend on the diffusional characteristics of the water layers close to the membrane surface (for a review, see Barry & Diamond³⁴). For intact plants, pure Brownian motion determines diffusion, since both intra- and extracellular water act as an unstirred region. In this respect NMR has the distinct advantage that the motion of water molecules bearing nuclear spins is followed directly and not *via* the motion of a tracer molecule. Since the concentration of water on both sides of the membrane is always approximately equal, the movement of water over the membrane is only determined by the permeability of that membrane to water molecules, if the tissue shows no net de- or rehydration.

Because no changes in tissue hydration are observed over two days of stress, the plant water balance can be considered to be in a semi-steady state condition. Therefore unstirred layers do not affect the membrane permeability observed in our NMR measurements.

In conclusion, the transverse relaxation rate $1/T_2$ shows a decrease during osmotic stress in pearl millet, which can be interpreted as due to a change of either the tonoplast or plasmalemma permeability, or both. We speculate that aquaporins play a crucial role in this change of the membrane transport properties, as these membrane proteins are thought to contribute to drought tolerance by facilitating water mobilisation towards critical cells. This is in accordance with the observed up- or downregulation of mRNA expression in several other plant species.^{11,33,35} The plasmalemma permeability may play an important role in tissue hydraulics, thereby facilitating the relocation of water to tissues with a relatively high osmotic water potential. The tonoplast permeability, on the other hand, is likely to control the water balance between the vacuole and the cytoplasm.¹¹ The combination of spin relaxation and diffusion as in our NMR experiments is useful to unravel the role of membrane transport in the hydraulics of a plant. The interpretation of the experimental NMR results is greatly facilitated by multi-compartment numerical modelling of such systems.

ACKNOWLEDGEMENTS

This Chapter will be published as:

Van der Weerd L., Claessens M.M.A.E., Efdé C. & Van As H. (2002) NMR imaging of membrane permeability changes in plants during osmotic stress. *Plant, Cell and Environment*, in press.

The authors wish to thank W.H.L. van Veenendaal, J. Nijssse and A.C. van Aelst (laboratory of Plant Cytology and Morphology) for help with the microscopical pictures. We thank Prof. T.J. Schaafsma for useful comments.

REFERENCES

1. Davies W.J. & Zhang J. (1991) Root signals and the regulation of growth and development of plants in drying soil. *Annual Review of Plant Physiology and Plant Molecular Biology* **42**, 55-76.
2. Nonami H., Wu Y. & Boyer J.S. (1997) Decreased growth-induced water potential. *Plant Physiology* **114**, 501-509.
3. Volkenburgh E.v. & Boyer J.S. (1985) Inhibitory effects of water deficit on maize leaf elongation. *Plant Physiology* **77**, 190-194.
4. Neumann P.M. (1995) The role of cell wall adjustment in plant resistance to water deficits. *Crop Science* **35**, 1258-1266.

5. Sarda X., Tousch D., Ferrare K., Cellier F., Alcon C., Dupuis J.M., Casse F. & Lamaze T. (1999) Characterization of closely related delta-tip genes encoding aquaporins which are differentially expressed in sunflower roots upon water deprivation through exposure to air. *Plant Molecular Biology* **40**, 179-191.
6. Yamada S., Komori T., Myers P.N., Kuwata S., Kubo T. & Imaseki H. (1997) Expression of plasma membrane water channel genes under water stress in *Nicotiana glauca*. *Plant and Cell Physiology* **38**, 1226-1231.
7. Barriau F., Marty M.D., Thomas D., Chaumont F., Charbonnier M. & Marty F. (1999) Desiccation and osmotic stress increase the abundance of mRNA of the tonoplast aquaporin BobTIP-1 in cauliflower cells. *Planta* **209**, 77-86.
8. Johansson I., Karlsson M., Shukla V.K., Chrispeels M.J., Larsson C. & Kjellbom P. (1998) Water transport activity of the plasma membrane aquaporin PM28a is regulated by phosphorylation. *Plant Cell* **10**, 451-459.
9. Smart L.B., Moskal W.A., Cameron K.D. & Bennett A.B. (2001) MIP genes are down-regulated under drought stress in *Nicotiana glauca*. *Plant and Cell Physiology* **42**, 686-693.
10. Verkman A.S. (2000) Water permeability measurement in living cells and complex tissues. *Journal Of Membrane Biology* **173**, 73-87.
11. Maurel C. (1997) Aquaporins and water permeability of plant membranes. *Annual Review of Plant Physiology and Plant Molecular Biology* **48**, 399-429.
12. Brownstein K.R. & Tarr C.E. (1979) Importance of classical diffusion in NMR studies of water in biological cells. *Physical Review A* **19**, 2446-2453.
13. Conlon T. & Outhred R. (1972) Water diffusion permeability of erythrocytes using an NMR technique. *Biochimica et Biophysica Acta* **288**, 354-361.
14. Snaar J.E.M. & Van As H. (1992) Probing water compartment and membrane permeability in plant cells by proton NMR relaxation measurements. *Biophysical Journal* **63**, 1654-1658.
15. Zhang W.H. & Jones G.P. (1996) Water permeability in wheat root protoplasts determined from nuclear magnetic resonance relaxation times. *Plant Science* **118**, 97-106.
16. Van der Weerd L., Claessens M.M.A.E., Ruttink T., Vergeldt F.J., Schaafsma T.J. & Van As H. (2001) Quantitative NMR microscopy of osmotic stress responses in maize and pearl millet. *Journal of Experimental Botany* **52**, 2333-2343.
17. Brownstein K.R. & Tarr C.E. (1977) Spin-lattice relaxation in a system governed by diffusion. *Journal of Magnetic Resonance* **26**, 17-24.
18. Aldrich S.R. & Leng E.R. (1966) Modern crop production. Cincinnati, Ohio, F & W Publishing Corporation.
19. Mahalakshmi V., Subramanian V., Bidinger F.R. & Jambunathan R. (1985) Effect of water deficit on yield and protein content in pearl millet grains. *Journal of the Science of Food and Agriculture* **36**, 1237-1242.
20. Hoagland D.R. & Arnon D.I. (1950) The water-culture method for growing plants without soil. *California Agriculture Experimental Station Circular* **347**.
21. Donker H.C.W., Van As H., Snijder H.J. & Edzes H.T. (1997) Quantitative ¹H-NMR imaging of water in white button mushrooms (*agaricus bisporus*). *Magnetic Resonance Imaging* **15**, 113-121.

22. Edzes H.T., Van Dusschoten D. & Van As H. (1998) Quantitative T2 imaging of plant tissues by means of multi-echo MRI microscopy. *Magnetic Resonance Imaging* **16**, 185-96.
23. Scheenen T.W.J., Van Dusschoten D., De Jager P.A. & Van As H. (2000) Microscopic displacement imaging with pulsed field gradient turbo spin-echo NMR. *Journal of Magnetic Resonance* **142**, 207-215.
24. Van der Weerd L., Vergeldt F.J., De Jager P.A. & Van As H. (2000) Evaluation of algorithms for analysis of NMR relaxation decay curves. *Magnetic Resonance Imaging* **18**, 1151-1157.
25. Provencher S.W. & Vogel R.H. (1983) Regularization techniques for for inverse problems in molecular biology. In: Numerical treatment of inverse problems in differential and integral equations (eds Deuffhard P. & Hairer E.), 304-319. Boston, Birkhauser.
26. Van der Weerd L., Melnikov S.M., Vergeldt F.J., Novikov E.G. & Van As H. (2001) Modelling of self-diffusion and relaxation time NMR in multi-compartment systems with cylindrical geometry. *Journal of Magnetic Resonance* **Submitted**.
27. Van Dusschoten D., Moonen C.T., De Jager P.A. & Van As H. (1996) Unraveling diffusion constants in biological tissue by combining Carr-Purcell-Meiboom-Gill imaging and pulsed field gradient NMR. *Magnetic Resonance in Medicine* **36**, 907-13.
28. Van As H., Nagarajan S., Van Dusschoten D. & Vergeldt F.J. (1995) Functional NMR imaging of osmotic stress in pearl millet and maize. *Plant Physiology* **108 supplement**, 40.
29. Mott R.L. & Steward F.C. (1972) Solute accumulation in plant cells. I. Reciprocal relations between electrolytes and non-electrolytes. *Annals of Botany* **36**, 621-639.
30. Hills B.P. & Duce S.L. (1990) The influence of chemical and diffusive exchange on water proton transverse relaxation in plant tissues. *Magnetic Resonance Imaging* **8**, 321-332.
31. Callaghan P.T. (1993) Principles of nuclear magnetic resonance microscopy. Oxford, Clarendon Press.
32. Leigh R.A. (1997) Solute composition of vacuoles. In: The plant vacuole (eds Leigh R.A. & Sanders D.), 171-194. London, Academic Press Limited.
33. Tyerman S.D., Bohnert H.J., Maurel C., Stuedle E. & Smith J.A.C. (1999) Plant aquaporins: Their molecular biology, biophysics and significance for plant water relations. *Journal of Experimental Botany* **50 (SI)**, 1055-1071.
34. Barry P.H. & Diamond J.M. (1984) Effects of unstirred layers on membrane phenomena. *Physiological reviews* **64**, 763-872.
35. Chrispeels M.J. & Maurel C. (1994) Aquaporins: The molecular basis of facilitated water movement through living plant cells? *Plant Physiology* **105**, 9-13.

7

NMR MICROSCOPY OF THE WATER STATUS IN MAIZE AND PEARL MILLET DURING OSMOTIC STRESS

*The stem water balance of maize (*Zea mays L.*) and pearl millet (*Pennisetum americanum L.*) was studied during -0.9 MPa osmotic stress by NMR imaging. The water content, stem area and transverse relaxation time (T_2) were used to monitor the stem and secondary shoots. During stress, no significant changes occurred in the maize stem, though the leaves wilted, and the plant died after 2 days of stress. Pearl millet showed shrinking stem tissue and large changes in T_2 , especially in the secondary shoots. These plants recovered once stress was relieved. The decreasing T_2 is interpreted within a plant cell model as caused by a combination of decreasing cell size and increasing membrane permeability. The latter could be useful to increase tissue conductance, thereby facilitating water re-allocation to young, expanding tissues.*

INTRODUCTION

Water transport and water content are important parameters regulating growth and reproduction in plants. The plant stem acts both as a water throughput to the leaves via the conducting vessels, and as a water reservoir to supply growing tissues during water deficit. Water stress is the most important cause of reduced crop yields and crop failure worldwide.^{1,2} Therefore, an understanding of the plant water balance and of possible drought tolerance mechanisms is vital to improve plant production.

In this paper, we present a study of two important plant species, which differ in drought tolerance. The first is pearl millet (*Pennisetum americanum L.*), a crop growing in shallow soil regions of Asia and Africa with a mean annual rainfall of 200-800 mm and high temperatures. This crop is able to grow and mature at a very low water level, and can survive prolonged periods of drought.³ The second crop, maize (*Zea mays L.*), grows ideally in climates with moderate temperatures and 400-600 mm of rain, and is much more sensitive to water deficits than millet.⁴

To study the cell water status in the stem, we used Nuclear Magnetic Resonance (NMR) imaging, which is a non-invasive technique to depict water in tissues. This technique can be used to obtain information on the physical properties of water in the tissue, as for example the measurement of cell dimensions,⁵ membrane damage due to freezing,^{6,7} or water flow and

cavitation in xylem vessels.^{8,9} A recent review about NMR imaging in plant science has been written by Ishida *et al.*¹⁰

In this paper, details about the stem water content during drought stress are presented for both maize and pearl millet. Furthermore, differences in the NMR relaxation time T_2 for the two plants are shown, and these parameters are interpreted within a model of cellular compartmentation and exchange between these compartments.^{11,12} Other studies already showed that this model can be applied to a plant cell, with the vacuole, the cytoplasm, and the cell wall as the main compartments; the exchange between these compartments is determined by the tonoplast and plasmalemma membranes. Thus the water status of the plant stem is evaluated, both at the organ and at the cellular level.

MATERIALS AND METHODS

PLANT MATERIAL

Maize (*Zea mays L.*, cv LG 11) and pearl millet (*Pennisetum americanum L.*, cv MH 179) seeds were germinated in wet sand in the dark. After one week the seedlings were transferred to a tank with half Hoagland nutrient solution,¹³ which was refreshed every week. The plants were grown in a phytotron at 25 °C and 70% relative humidity with a photoperiod of 16 hours and a light intensity of 40 W m⁻² (mercury vapour lamp). Before the measurements the plants were transferred to separate vessels, which were designed to fit in the NMR imager. The plants were 4 weeks old, with 6 fully emerged leaves, at the time of the measurements.

The maize and pearl millet plants (N=2 for both species) were placed in the NMR machine and control measurements were obtained for several hours. Next the nutrient medium was replaced by a -0.9 MPa PEG 6000 solution in nutrient medium without disturbing the position of the plant in the magnet.

MRI EXPERIMENTS

The NMR spectrometer was a 20.35 MHz imager consisting of a 0.47 T Bruker electromagnet (Karlsruhe, Germany) controlled by a S.M.I.S. console (S.M.I.S., Guildford, England). A shielded gradient probe with a vertical open cylindrical access of 30 mm diameter was used (Doty Scientific Inc., Columbia, South Carolina, USA). T_2 values were measured using a multi-spin-echo imaging pulse sequence with slice selection,^{14,15} a repetition time (TR) of 1800 ms, a spin-echo time (TE) of 4.6 ms and a spectral bandwidth of 50 kHz. A 128 × 128 matrix of complex data points was acquired per echo, and 48 echoes were acquired per echo train. For each image four acquisitions were averaged to improve the image quality, resulting in a total scan time of 15 minutes per image. The field-of-view was 30 mm, and the slice thickness 2.5 mm.

The acquired NMR data sets were analysed by home-written calculation routines in IDL (Research Systems Inc., Boulder, Colorado, USA). The multi-echo images were fitted on a pixel-by-pixel base using a mono-exponential decay function, yielding quantitative amplitude and $1/T_2$ images.^{14,15} After phase correction, the real part of the signal was used for analysis.¹⁶

To determine the stem area, all pixels containing signal above the noise level were summated. The total water content in the slice was calculated by summation of all amplitude values within this selected stem area.

RESULTS AND DISCUSSION

ANATOMY

The stem images were taken 2 cm above the roots, where the stem consists of mature, fully elongated tissue. In this tissue the vascular bundles are scattered in the stem tissue, with the smaller bundles arranged near the periphery and the larger bundles situated in the middle. The tissue between the vascular bundles is called the pith or parenchyma, and consists of large vacuolised cells.¹² Cross-sectional images of one of the maize and pearl millet plants are shown in Figs. 7.1 and 7.2 respectively. The vascular bundles can clearly be seen in the millet tissue (a). Around the stem, the leaves are visible (b). Millet is a species that forms multiple shoots. Two of those are visible in this specific plant (c). The amplitude images do not show much contrast, which means that the amount of water per pixel is fairly homogeneous. Earlier reports already showed that the relaxation rate ($1/T_2$) is linearly related to the cell dimensions in vacuolised cells.¹² The contrast in the $1/T_2$ images in Figs. 7.1 and 7.2 can mostly be explained by differences in cell size, e.g. the cells of the stem periphery and the secondary shoots are smaller than those of the central parenchyma tissue.

OSMOTIC STRESS

Osmotic stress was applied by replacing the normal root medium by a -0.9 MPa PEG 6000 solution. The maize plants were wilted after 20 hours of stress and after 2 days the leaves became necrotic. When a normal root medium was supplied again the plants failed to recover. During the stress period, slight changes occurred in the relaxation rate of the stem tissue (Fig. 7.1). The amplitude images did not show any differences in water content or stem area during the stress period (Figs. 7.1, 7.3 and 7.4).

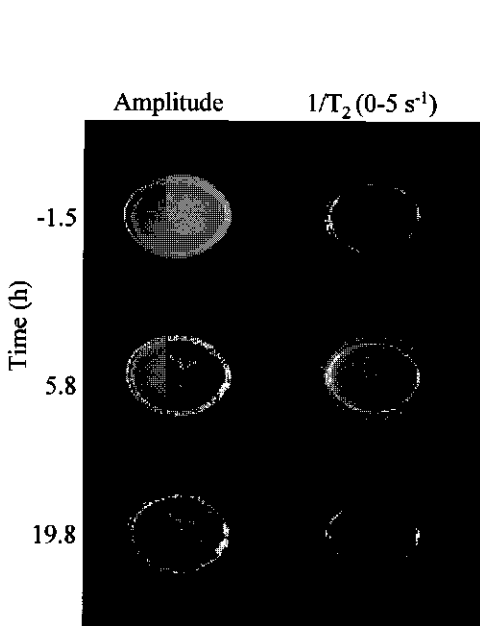


Figure 7.1. Amplitude and $1/T_2$ images of a maize plant during -0.9 MPa PEG 6000 stress. The amplitude images reflect the proton density of the tissue; $1/T_2$ ($0-5\text{ s}^{-1}$) indicates the minimum and maximum values of $1/T_2$ depicted in the image. The marks a-b denote different tissues discussed in the text.

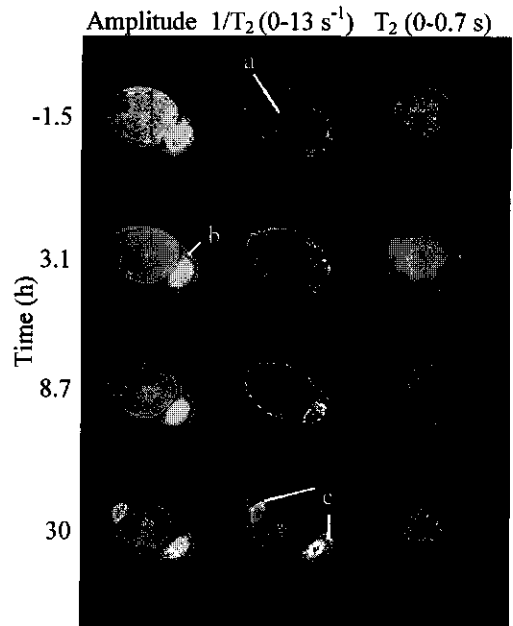


Figure 7.2. Amplitude, $1/T_2$ and T_2 images of a pearl millet plant during -0.9 MPa PEG 6000 stress. The marks a-c denote different tissues discussed in the text. For further explanation see Fig. 7.1.

Pearl millet on the other hand did not show wilting symptoms until 70 hours of stress. Even then, the plants survived once the stress was relieved. The stem images show several remarkable affects, which are summarised in Table 7.1. Firstly, the stem tissue shrinks significantly (Figs. 7.2 and 7.3), about 16% after 36 hours of stress. The total amount of water in the stem slice decreases even more (Fig. 7.4). A closer look at the amplitude images reveals that this decrease with water content is not uniform over the plant stem; the secondary shoots shrink less than the mature stem, and the amount of water per pixel in these shoots even increases (Fig. 7.2).

The relaxation images show even more effects. The relaxation time T_2 in the central part of the stem, around the large xylem vessels, decreases during the stress period. The effect of stress on the secondary shoots is much larger; the T_2 decreases by as much as 50% within 30 hours of stress (Table 7.1).

PEG (h)	Main shoot			Secondary shoot		
	Area (a.u.)	Water content (a.u.)	1/T ₂ (s ⁻¹)	Area (a.u.)	Water content (a.u.)	1/T ₂ (s ⁻¹)
0	1	1	4.9 ± 0.1	1	1	5.8 ± 0.2
30	0.84 ± 0.01	0.79 ± 0.01	5.3 ± 0.2	0.88 ± 0.02	0.89 ± 0.02	12.0 ± 0.3

Table 7.1. Relative shoot area, water content and 1/T₂ for main shoot and secondary shoot of pearl millet.

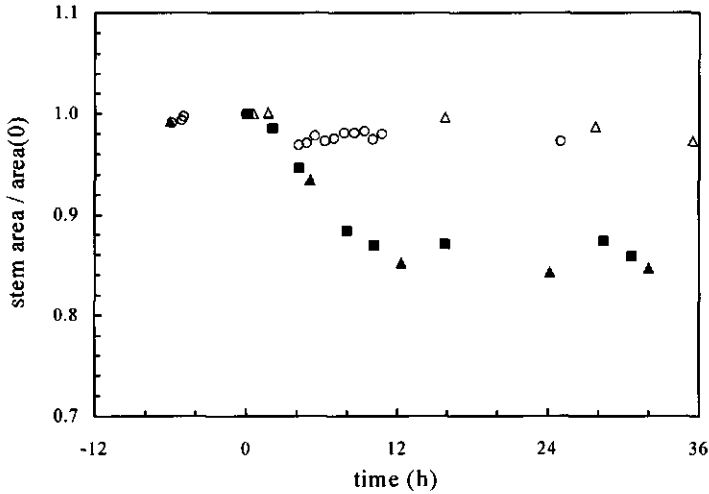


Figure 7.3. Relative stem area (stem area / stem area at t = 0) of maize (Δ, ○) and pearl millet (▲, ●) during stress. The different symbols mark different plants. -0.9 MPa PEG 6000 was applied at time = 0 hours.

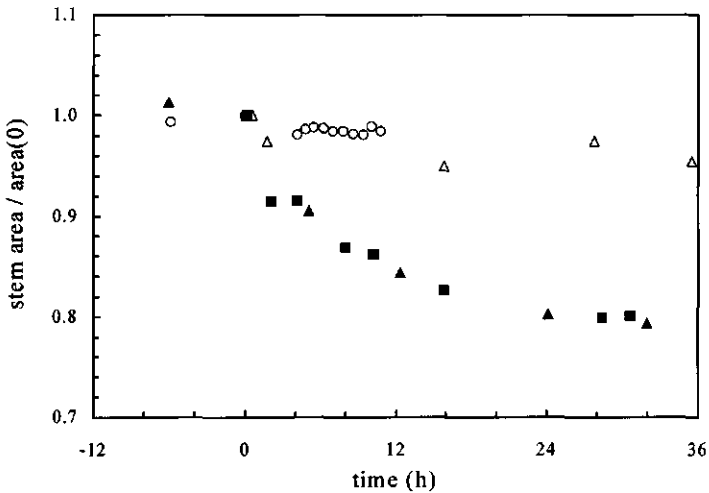


Figure 7.4. Relative water content (water content / water content at t = 0) within the image slice of maize (Δ, ○) and pearl millet (▲, ●) during stress. The different symbols mark different plants. -0.9 MPa PEG 6000 was applied at time = 0 hours.

Generally speaking, the maize plant is dehydrating mostly in the leaves, where the water level becomes so low that the cells are damaged. At that moment, the stem tissue is still intact, but because the leaves are essential for energy production, the whole plant does not survive the stress period.

Pearl millet showed a completely different response. Both the leaves and the stem shrink and loose water, but the water level in the cells remains high enough to ensure survival. The amount of water in secondary shoots decreases less than in the mature parts of the plant, which may indicate that these young tissues are favoured above the mature tissue. The T_2 decreases slightly in the parenchyma of the main stem, especially around the vascular bundles. The secondary shoots show a much larger T_2 decrease, which can be explained with a model that describes the relation between the observed T_2 of the cell water, the dimensions of the cells and the magnetisation sink strength density H (m s^{-1}):

$$1/T_{2,obs} = H(1/R_x + 1/R_y + 1/R_z) + 1/T_{2,bulk} \quad [7.1]$$

where $R_{x,y,z}$ are the average radii in three directions of the vacuole.¹² H indicates the rate of magnetisation loss at the vacuolar membrane due to exchange with the water in the cytoplasm and the extracellular space, which have a much shorter intrinsic relaxation time.¹⁸ The exchange rate is determined by the permeability of the tonoplast and plasmalemma membranes for water. The decrease in stem diameter probably results in a decrease in cell size, which in turn causes a decrease in the relaxation time T_2 (Eqn. 7.1). However, cell shrinkage cannot completely explain the found T_2 shortening; the observed volume decrease of 20% results in a 7% change of the vacuolar radius for a spherical cell, which would affect the T_2 for about the same amount. This corresponds nicely to the found decrease in T_2 for the mature stem. The secondary shoot however shows much larger changes in T_2 . Therefore, an additional effect must be present. Changes in the $T_{2,bulk}$ are not likely (see Chapter 6). The only variable that can be responsible for the large T_2 decrease is H .

The increase in H indicates an increase in exchange rate of water between the vacuole and the cytoplasm / cell wall. Most likely, this means that the tonoplast and plasmalemma permeabilities for water increase. This would result in a higher tissue conductance, which facilitates water transport between tissues, in this case from the main shoot to the young tissue, providing that the necessary water potential gradient is present due to osmotic adjustment of the young shoot. This water redistribution is a well-known process in several species to secure reproduction during stress.^{2,17}

REFERENCES

1. Boyer J.S. (1985) Water transport. *Annu Rev Plant Physiol* **36**, 473-516.
2. Hsiao T. (1973) Plant responses to water stress. *Ann. Rev. Plant Physiol.* **24**, 519-570.
3. Mahalakshmi V., Subramanian V., Bidinger F.R. & Jambunathan R. (1985) Effect of water deficit on yield and protein content in pearl millet grains. *Journal of the Science of Food and Agriculture* **36**, 1237-1242.
4. Aldrich S.R. & Leng E.R. (1966) Modern crop production. Cincinnati, Ohio, F&W Publishing Corporation.
5. Wycoff W., Pickup S., Cutter B., Miller W. & Wong T.C. (2000) The determination of the cell size in wood by nuclear magnetic resonance diffusion techniques. *Wood and Fiber Science* **32**, 72-80.
6. Chen P.M., Gusta L.V. & Stout D.G. (1978) Changes in membrane permeability of winter wheat cells following freeze-thaw injury as determined by nuclear magnetic resonance. *Plant Physiology* **61**, 878-882.
7. Millard M.M., Veisz O.B., Krizek D.T. & Line M. (1996) Thermodynamic analysis of the physical state of water during freezing in plant tissue, based on the temperature dependence of proton spin-spin relaxation. *Plant, Cell and Environment* **19**, 33-42.
8. Scheenen T.W.J., Heemskerck A.M., De Jager P.A., Vergeldt F.J. & Van As H. (2002) Functional imaging of plants: A nuclear magnetic resonance study of a cucumber plant. *Biophysical Journal* **82**, 481-492.
9. Kuchenbrod E., Kahler E., Thurmer F., Deichmann R., Zimmermann U. & Haase A. (1998) Functional magnetic resonance imaging in intact plants - Quantitative observation of flow in plant vessels. *Magnetic Resonance Imaging* **16**, 331-338.
10. Ishida N., Koizumi M. & Kano H. (2000) The NMR microscope: a unique and promising tool for plant science. *Annals of Botany* **86**, 259-278.
11. Snaar J.E.M. & Van As H. (1992) Probing water compartment and membrane permeability in plant cells by proton NMR relaxation measurements. *Biophysical Journal* **63**, 1654-8.
12. Van der Weerd L., Claessens M.M.A.E., Ruttink T., Vergeldt F.J., Schaafsma T.J. & Van As H. (2001) Quantitative NMR microscopy of osmotic stress responses in maize and pearl millet. *Journal of Experimental Botany* **52**, 2333-2343.
13. Hoagland D.R. & Arnon D.I. (1950) The water-culture method for growing plants without soil. *California Agriculture Experimental Station Circular* **347**.
14. Donker H.C.W., Van As H., Snijder H.J. & Edzes H.T. (1997) Quantitative ¹H-nmr imaging of water in white button mushrooms (agaricus bisporus). *Magnetic Resonance Imaging* **15**, 113-121.
15. Edzes H.T., Van Dusschoten D. & Van As H. (1998) Quantitative ¹²C imaging of plant tissues by means of multi-echo mri microscopy. *Magnetic Resonance Imaging* **16**, 185-96.
16. Van der Weerd L., Vergeldt F.J., De Jager P.A. & Van As H. (2000) Evaluation of algorithms for analysis of NMR relaxation decay curves. *Magnetic Resonance Imaging* **18**, 1151-1157.
17. Boyer J.S. (1982) Plant productivity and environment. *Science* **218**, 443-448.

8

GENERAL DISCUSSION

Food production for the earth's fast growing population increasingly has to make use of (semi)arid regions. Agriculture in these regions demands suitable drought-tolerant crops. A better understanding of drought tolerance in plants is of crucial importance to set up efficient breeding programs for such crops.

New *in vivo* methods to study individual plants and crops are essential to monitor the temporal effects of drought stress. NMR is a non-invasive technique to study the plant water status down to the cellular level. The relaxation time T_2 of water in cells is known to decrease by the presence of extracellular magnetisation sinks.¹ Therefore, changes in the cell water balance due to drought stress are expected to be reflected in T_2 , D_{app} and signal amplitude (research question 2, Chapter 1). Secondly, since the theory of relaxation and diffusion in model systems such as cylinders and spheres is fairly well established, these NMR parameters conceivably would be quantitatively related to physiologically relevant information. This information concerns the cellular water balance, and its relation with the cell dimensions and the membrane permeability for water (research question 3, Chapter 1). In particular the membrane permeability is of great importance to understand drought tolerance, because permeability is one of the factors that regulate tissue hydraulics.

The focus of our research was to understand the relation between the cell water balance and the NMR parameters T_2 , D_{app} and the signal amplitude during drought.

This research lead to the following results:

- (i) Drought stress indeed affects T_2 , D_{app} and the NMR signal amplitude in pearl millet. A distinctive difference in the changes of the above-mentioned NMR parameters was observed for maize and pearl millet during drought stress.
- (ii) A numerical model has been developed to interpret the experimental data.
- (iii) A qualitative relation has been established by numerical modelling between T_2 and the membrane permeability.
- (iv) A linear experimental relation has been found between T_2 and cell size.
- (v) A T_2 decrease in pearl millet during stress has been found. This decrease can be interpreted as an increase in membrane permeability for water.

In the remaining part of this Chapter, these results will be discussed and a concept for the water balance in pearl millet is proposed.

SINK STRENGTH AND PERMEABILITY

One of the most important research questions at the start of this project was: is it possible to measure membrane permeabilities in intact plants? Earlier studies already have shown that magnetisation loss in compartmentalised systems due to relaxing boundaries could be treated analogously to heat dissipation from solid bodies. From these existing theories, equations were derived for the relaxation rate and the surface sink strength H .¹ For biological cells, the most important relaxation sink is not the membrane itself, but the extracellular fluid, which acts as a volume sink. If the relaxation time of this fluid is short compared to the exchange time over the membrane, the relaxation rate is solely determined by the membrane permeability for water (P); the sink strength H is then equal to the permeability P .

Most research in this area concerned special situations where this prerequisite was indeed met, e.g. red blood cells, protoplasts in Mn^{2+} -doped water, or Mn^{2+} -infiltrated plant tissue.²⁻⁵ In many cases, however, the extracellular fluid acts as a partial sink, but not a perfect one. Decreasing the extracellular relaxation time by infiltration with paramagnetic ions greatly disturbs the plant. Therefore infiltration was not used in this project, but a numerical model was developed to simulate the effects of partial relaxation sinks on the NMR parameters (Chapter 4).

To a great extent, a simple common sense approach is sufficient to explain the effect of compartment properties on relaxation and diffusion. In isolated plant cells for example, the intermembrane distances (r) and the bulk diffusion coefficients (D) determine the average diffusion time of a water molecule to cross a compartment ($t_{diff} = 2Dr^2$). The relaxation rate in that compartment determines the chance that the molecule still bears magnetisation once it reaches the membrane. If that is the case ($2Dr^2 < 1/T_2$), the membrane permeability determines the exchange rate to the next compartment, and thereby influences the relaxation rate; if the above condition does not apply, the membrane permeability is of no consequence for the NMR signal. This means that the effective sink strength depends on the intermembrane distances, the bulk T_2 and D values for every compartment, the membrane permeability and even on transcellular transport. Clearly, this is a far too complicated situation to justify a quantitative determination of the tonoplast and plasmalemma permeabilities. Fortunately, the sink strength H and the membrane permeability P are often linearly related, which means that changes in P can be observed as equally large changes in H , and thus changes in membrane permeability can be quantified (Chapter 4).

Though other methods are available to determine the membrane permeability quantitatively, these methods are limited to single cells and a time span of about one hour.^{6,7} Furthermore, some experiments suggest that the membrane permeability can vary greatly (as much as a factor 1000) between individual cells, which means that numerous replications are needed for a statistically justified interpretation. (Chrispeels, personal communication). Therefore NMR

imaging is of interest because of its non-invasive nature, overview of the entire tissue and the possibility to follow a single plant during long time spans.

CELL-TO-CELL TRANSPORT

Most theoretical cases in this Thesis consider a single plant cell with a reflecting outer boundary. Of course this is not a complete picture of the water balance in plant tissues; cell-to-cell connections play an important role in the overall tissue hydraulics. Three different pathways exist for this cell-to-cell transport (see Chapter 1): the apoplastic pathway and the symplastic one, which can be divided into transmembrane transport and transport via the plasmodesmata. Each of these pathways has different effects on the NMR results. From an NMR point of view, the apoplast pathway is the simplest. This transport takes place via the extracellular space, which has a very short relaxation time. Therefore, water molecules in this space mostly lose magnetisation before moving over long distances and thus the effect of this transport on D_{app} and T_2 is negligible.

Transmembrane transport is somewhat different. The relative importance of this pathway depends on the tonoplast and plasmalemma permeabilities for water. These permeabilities also influence T_2 , as was established in Chapter 4. However, here only magnetisation loss due to *intracellular* volume sinks was considered. In the case of cell-to-cell transport, water molecules move through the membranes from one cell to the next via the extracellular space, a situation comparable to that in Fig. 4.8A. The loss of magnetisation then depends on the time spent in this extracellular volume. If this time is reasonably short, molecules that move into the next cell still bear magnetisation. This does not affect the relaxation times, if we assume that there is no fundamental difference between the properties of the different cells; theoretically there is no difference in relaxation between spins that are reflected at the outer boundary and diffuse back into the cell, or spins that cross the outer boundary and diffuse into the next cell. The diffusion attenuation, however, is affected, since the maximum diffusion distance becomes larger (Fig. 4.8B).

The third pathway is that of cell-to-cell transport via the plasmodesmata. Now there are no membranes present between adjacent cells. Assuming that the relaxation rate within the plasmodesmata is comparable to that of the cytoplasm, the magnetisation loss during transport from one cell to another will be much less than in the two previous cases. Therefore the diffusion attenuation will be most sensitive for this pathway (Fig. 4.8C). Using long-time diffusion measurements for intact plant studies may therefore provide useful additional information on tissue hydraulics.

RESOLUTION

The information present in a pixel within an NMR image depends on several parameters. Firstly, the accuracy of the NMR signal depends on the signal-to-noise ratio (SNR), which depends on the amount of spins in that pixel. The larger the pixel, the higher the SNR will be. Signal averaging also increases the SNR, but also the total measuring time. Therefore one always compromises between the spatial resolution and the SNR within the available measurement time. In the case of the growth experiments (Chapter 5), the measurement time was limited to about 20 minutes, because the plant movements through the image plane would cause blurring for longer experiments.

The resolution of the images presented here is not large enough to provide (sub-)cellular details. However, this does not hamper the extraction of sub-cellular information. For one, the parenchyma tissue of both maize and pearl millet is very homogeneous, with a narrow cell size distribution (Figs. 5.3 and 5.6); therefore, cellular changes within a pixel will still be visible in the overall NMR parameters. Secondly, the tissue is completely vacuolised, and the vacuole comprises about 95 % of the total volume, which means that the relaxation decay can be approximated by a mono-exponential fit. To provide even more detail, one can summate the signal from pixels within the same tissue to increase the SNR so that a multi-exponential fit is possible. This results in two or more fractions, which can be assigned to subcellular compartments such as the vacuole and the cytoplasm, thus yielding a sub-cellular resolution in a pixel larger than a single cell.^{3,8}

Quantitative T_2 measurements can even be severely distorted by a high spatial resolution. At pixel sizes smaller than $\sim 100 \mu\text{m}$ for relaxation rates of about a second, signal attenuation due to self-diffusion of molecules in the read gradient is obscuring the relaxation decay. Ultimately, at very small pixel sizes, uniform short T_2 values result because the decays are no longer governed by T_2 relaxation, but by the diffusion of the water molecules.^{9,10}

PLANT WATER BALANCE

At first sight, it is rather strange that the drought-sensitive maize does not show any changes in the NMR images during stress, whereas the drought-tolerant pearl millet does. To understand this, the whole plant stress response has to be considered. Maize shows leaf rolling and, after two days of severe osmotic stress (-0.9 MPa), the leaves become necrotic. When the stress is relieved, the plant does not recover again (Chapter 7). So, though the plant stem does not dehydrate noticeably, the leaves are irreversibly damaged, whereby the plant loses its ability to bind CO_2 and generate energy.

Pearl millet on the other hand shows wilting leaves but the leaves do not become necrotic and the plant recovers, even after four days of severe osmotic stress (Chapter 7). The leaf parenchyma cells are not the only ones to dehydrate; the stem tissue is also shrinking during stress (Fig. 7.3). Secondary shoots and the growing apical tissue however, loose significantly less water (Figs. 6.2, 6.6, 7.2, Table 7.1). In general, it may be that the older stem parenchyma is loosing water in favour of younger shoots and growing tissue, in order to secure reproduction. This is a well-known process in several plants.^{11,12} Though most tissues are loosing water during stress, the organs do not dehydrate enough to cause cell damage.

The observed increase in membrane permeability (Fig. 6.5) may result in increased tissue conductance for water. This promotes a rapid water movement between tissues; osmotic adjustment of the young tissues would provide the necessary potential gradient (Table 6.2). During the first 8-10 hours of osmotic stress, the permeability remained constant, or even declined slightly (Fig. 6.5). Possibly, this period is used to build up an osmotic potential gradient from older to younger tissues. If aquaporins are indeed involved in the permeability increase, the time scale of this first period would be right for the necessary mRNA transcription and protein synthesis.

FUTURE

This study clearly shows that NMR can be used to visualise membrane permeability changes. The next step is correlating these changes to tissue hydraulics, which is actually determining the rate of water flow between different parts of the plant. Therefore, it would be interesting to combine these NMR measurements with hydraulic conductivity measurements, e.g. with a high-pressure flow meter.¹³

On the other hand, changes in membrane permeability are regulated on the molecular and/or the genetic level. Recent reports already showed that mRNA levels for aquaporins vary enormously during stress. However, very little is known about the actual protein levels or functionality. Therefore, the gap between gene expression and their effect on plant function still remains. Overexpression plants, knock-out plants or anti-sense plants show different aquaporin gene expression patterns compared to wildtype plants and may be of great help to understand the relation between aquaporin gene expression and function. NMR imaging can elucidate *in vivo* gene functionality and thereby bridge the gap between gene expression and function.

REFERENCES

1. Brownstein K.R. & Tarr C.E. (1979) Importance of classical diffusion in NMR studies of water in biological cells. *Physical Review A* **19**, 2446-2453.
2. Conlon T. & Outhred R. (1972) Water diffusion permeability of erythrocytes using an NMR technique. *Biochimica et Biophysica Acta* **288**, 354-361.
3. Snaar J.E.M. & Van As H. (1992) Probing water compartment and membrane permeability in plant cells by proton NMR relaxation measurements. *Biophysical Journal* **63**, 1654-8.
4. Zhang W.H. & Jones G.P. (1996) Water permeability in wheat root protoplasts determined from nuclear magnetic resonance relaxation times. *Plant Science* **118**, 97-106.
5. Stout D.G., Steponkus P.L. & Cotts R.M. (1978) Nuclear magnetic resonance relaxation times and plasmalemma water exchange in ivy bark. *Plant Physiology* **62**, 636-641.
6. Tomos A.D. & Leigh R.A. (1999) The pressure probe: A versatile tool in plant cell physiology. *Annual Review of Plant Physiology and Plant Molecular Biology* **50**, 447-472.
7. Verkman A.S. (2000) Water permeability measurement in living cells and complex tissues. *Journal of Membrane Biology* **173**, 73-87.
8. Scheenen T.W.J., Heemskerk A.M., De Jager P.A., Vergeldt F.J. & Van As H. (2002) Functional imaging of plants: A nuclear magnetic resonance study of a cucumber plant. *Biophysical Journal* **82**, 481-492.
9. Edzes H.T., Van Dusschoten D. & Van As H. (1998) Quantitative T2 imaging of plant tissues by means of multi-echo MRI microscopy. *Magnetic Resonance Imaging* **16**, 185-96.
10. Callaghan P.T. (1993) Principles of nuclear magnetic resonance microscopy. Oxford, Clarendon Press.
11. Boyer J.S. (1985) Water transport. *Annual Review of Plant Physiology* **36**, 473-516.
12. Hsiao T. (1973) Plant responses to water stress. *Annual Review of Plant Physiology* **24**, 519-570.
13. Tyree M.T., Patino S., Bennink J. & Alexander J. (1995) Dynamic measurements of root hydraulic conductance using a high-pressure flowmeter in the laboratory and field. *Journal of Experimental Botany* **46**, 83-94.

SUMMARY

This Thesis presents an approach for the study of plant water balance during drought stress, using a combination of *in vivo* NMR experiments and computer simulations. The ultimate aim is the interpretation of the NMR parameters in terms of physiologically relevant characteristics, such as cell dimensions and membrane permeability. Especially the latter has raised a growing interest in plant science, and up to now the measurement of this parameter *in vivo* was limited to single cells and short experiment time spans.

NMR microscopy of plants yields information on various levels of organisation. The NMR images provide clear anatomical details, which have been used to monitor the response of stem growth rates to osmotic stress. On the tissue and cell levels, the NMR parameters T_2 (transverse spin relaxation time) and D_{app} (apparent diffusion coefficient) provide information on the physical and chemical properties. Correct quantitative values for T_2 and D_{app} are crucial for a useful interpretation. Therefore, Chapter 2 evaluates the accuracy of different fitting procedures.

The physical and chemical properties can vary considerably between and within different tissues, cells, and intracellular compartments, resulting in distinctly different relaxation and diffusion characteristics for these compartments. The interpretation of these parameters is not straightforward. A numerical model of restricted diffusion and relaxation behaviour was therefore developed, based on Fick's second law of diffusion (Chapter 3). This model expands previous one-dimensional models to a two-dimensional space, consisting of multiple concentric cylindrical compartments, separated by membranes. Numerical simulation experiments using this model demonstrate the importance of modelling two-dimensional diffusion in relation to the effects of spatial restrictions, and spin exchange between the different compartments.

This model has been applied to investigate the effects of diffusive exchange on the transverse spin relaxation times, the apparent diffusion coefficients, and the NMR signal amplitudes of water in plant cells (Chapter 4). For different multi-compartment model systems a Pulsed Field Gradient Multiple Spin Echo (PFG-MSE) experiment was simulated, and intrinsic physiological parameters, i.e. the bulk diffusion constant, the cell radius and the membrane permeability were afterwards extracted using common theoretical models. The results justify the use of these models to interpret the *in vivo* experiments, since meaningful diffusion constants, cell radii and membrane permeabilities can be extracted for a large range of conditions. This is still true if not all conditions of the theory are known or met, e.g. for intact plants.

Chapters 5 and 6 study the effect of mild osmotic stress on maize and pearl millet by *in vivo* ^1H NMR microscopy, and water uptake measurements. Single NMR parameter images of (i) the water content, (ii) the transverse relaxation time (T_2) and (iii) the apparent diffusion

coefficient (D_{app}) were used to follow the water status of the stem apical region during osmotic stress. The results are interpreted using the multi-compartment model (Chapter 4), tailored to suit plant cells. For this particular case, an equation was derived to describe the relation between the observed T_2 , the cell dimensions, the bulk T_2 , and the membrane permeability, based on the Brownstein & Tarr theory. Experimentally determined T_2 values of non-stressed stem tissue are indeed correlated to the cell dimensions, which is in agreement with the derived equation. The T_2 of maize cells is higher than the T_2 of equally sized millet cells, implying that the membrane permeability of the latter is higher.

The growth rate was strongly inhibited by mild stress in both species, even though the water uptake was only mildly affected. During stress, there are hardly any changes in water content or T_2 of the stem region of maize. In contrast, the apical tissue of pearl millet showed a ~30% decrease of T_2 within 48 hours of stress, whereas the water content and D_{app} hardly changed. This decrease in T_2 can be caused by a decreasing cell radius, a decreasing bulk T_2 , and/or an increasing membrane permeability for water. To distinguish between these contributions, additional scanning electron microscopy was used, showing no apparent changes in cell size. Transverse spin relaxation measurements of a wide range of sugar solutions showed only very small effects of osmotic adjustment on the bulk T_2 . Together, these results point to an increase in membrane permeability during stress. This conclusion is confirmed by numerical simulations of the plant cell model, which showed that only an increasing membrane permeability yields a similar combination of water content, T_2 , and D_{app} values during stress.

Under severe osmotic stress, the effects on the plant water balance are naturally larger (Chapter 7). During stress, no significant changes occurred in the maize stem, though the leaves wilted, and the plant died after two days of stress. Pearl millet showed again changes in T_2 , especially in the secondary shoots, which were more pronounced than during mild stress. Furthermore, the stem tissue shrunk, implying that the cell dimensions changed; the secondary shoots showed far less decrease in water content, however. Despite these changes, the plants recovered once stress was relieved. In the framework of the plant cell model, the decreasing T_2 is interpreted as the result of a combination of decreasing cell size and increasing membrane permeability. The latter can result in a higher tissue conductance, thereby facilitating water re-allocation to young, expanding tissues to prevent irreparable damage.

The combination of experimental data and simulations as presented in this Thesis has proven to be an effective tool to link NMR information to physiology (Chapter 8). This approach promises to be of great use to plant science, and to NMR microscopy in general.

SAMENVATTING

Dit proefschrift behandelt een manier om de water balans in planten te bestuderen tijdens droogte, met behulp van een combinatie van *in vivo* NMR-experimenten en computersimulaties. Het uiteindelijke doel is de interpretatie van de NMR-parameters in relatie tot fysiologisch relevante eigenschappen, zoals celgrootte en membraanpermeabiliteit. De laatste eigenschap krijgt steeds meer aandacht van de plantwetenschappen, maar kon tot nu toe *in vivo* alleen bepaald worden in individuele cellen en gedurende korte periodes.

NMR microscopie levert informatie over verschillende organisatorische niveaus in een plant. NMR-afbeeldingen laten duidelijk de anatomische structuur zien, waardoor het mogelijk was de stengelgroei tijdens osmotische stress te volgen. Informatie over de chemische en fysische eigenschappen op weefsel- en celniveau kan verkregen worden vanuit de NMR parameters T_2 (transversale spin relaxatietijd) en D_{app} (schijnbare diffusie coefficient). Een goede interpretatie van deze parameters is afhankelijk van correcte kwantitatieve gegevens. Daarom behandelt Hoofdstuk 2 de kwaliteit van verschillende methodes om de NMR gegevens te analyseren.

De chemische en fysische eigenschappen tussen en zelfs binnen verschillende weefsels, cellen en intracellulaire compartimenten kunnen aanzienlijk variëren, wat resulteert in een duidelijk verschil in relaxatie- en diffusie-eigenschappen. De interpretatie van deze verschillen is echter gecompliceerd en daarom werd een numeriek model voor diffusie en relaxatie ontwikkeld. Dit model is gebaseerd op de tweede diffusiewet van Fick (Hoofdstuk 3). Het model breidt eerdere een-dimensionale modellen uit naar een twee-dimensionale ruimte, bestaande uit meerdere concentrische cilindrische compartimenten, gescheiden door membranen. De numerieke simulaties met dit model tonen het effect van de twee-dimensionale aanpak op ruimtelijke beperkingen, en uitwisseling tussen de verschillende compartimenten.

Dit model is toegepast om het effect van uitwisseling op T_2 , D_{app} en de amplitude van het NMR signaal van water in plantencellen te bestuderen (Hoofdstuk 4). Daartoe zijn Gepulst Veld Gradient Multi Spin Echo (PFG-MSE) experimenten gesimuleerd voor verschillende modelsystemen met meerdere compartimenten. De intrinsieke fysiologische grootheden, zoals de bulk diffusiecoefficient, de straal van de cel en de membraanpermeabiliteit werden achteraf berekend met bekende theoretische modellen. De resultaten rechtvaardigen het gebruik van deze modellen om *in vivo* experimenten te interpreteren, omdat zinvolle waarden voor diffusiecoefficienten, celdiameters en membraanpermeabiliteiten verkregen werden voor een uitgebreid spectrum van verschillende fysiologische condities. Dit geldt zelfs wanneer niet volledig aan alle voorwaarden van de theorie is voldaan, zoals het geval is in plantencellen.

De effecten van milde osmotische stress op mais en gierst worden in de Hoofdstukken 5 en 6 bestudeerd met behulp van *in vivo* ^1H NMR en water opname studies. NMR afbeeldingen

van (i) het watergehalte, (ii) de transversale relaxatietijd, en (iii) de schijnbare diffusiecoëfficiënt (D_{app}) worden gebruikt om water in de stengel te volgen. Het meerdere-compartimenten-model (Hoofdstuk 4) werd toegepast op plantencellen om de resultaten te verklaren. Voor dit specifieke geval is een vergelijking afgeleid om de relatie tussen de waargenomen T_2 , de celdimensies, de bulk T_2 en de membraanpermeabiliteit te beschrijven, gebaseerd is op de theorie van Brownstein & Tarr. De experimenteel bepaalde T_2 -waarden van parenchymcellen zonder stress kunnen worden gecorreleerd aan de celgrootte, wat inderdaad uit de afgeleide vergelijking volgt. De T_2 voor maiscellen is hoger dan de T_2 voor gierstcellen met eenzelfde grootte, wat inhoudt dat de membraanpermeabiliteit van de laatste hoger is.

De milde stress, die de groeisnelheid voor beide soorten sterk reduceert, heeft slechts een geringe invloed op de wateropname. Het watergehalte en de T_2 in de stengel van mais veranderen nauwelijks gedurende de stress. De T_2 in het stengelweefsel van gierst nam echter ~30% af, terwijl het watergehalte en D_{app} nagenoeg gelijk bleven. Deze afname in T_2 kan het resultaat zijn van een verminderde celgrootte, een kortere bulk T_2 , of een hogere membraanpermeabiliteit. Extra SEM (Scanning Electron Microscopie) metingen lieten echter zien dat de celgroottes niet veranderen. Ook een eventuele verhoging van de suikerconcentratie door osmotische aanpassing heeft nauwelijks invloed op de bulk T_2 , zoals werd aangetoond met behulp van relaxatiemetingen aan verschillende suikeroplossingen. De afname van de T_2 lijkt dus te worden veroorzaakt door een toenemende membraanpermeabiliteit. Deze conclusie wordt bevestigd door numerieke simulaties die lieten zien dat gedurende stress alleen een toename in de membraanpermeabiliteit een vergelijkbare combinatie van watergehalte, T_2 en D_{app} oplevert.

Wanneer een zwaardere osmotische stress gebruikt wordt, zijn de gevolgen op the waterbalans van de plant uiteraard ook groter (Hoofdstuk 7). In mais, de stress had nauwelijks zichtbare gevolgen voor de stengel, terwijl de bladeren duidelijk slap hingen; na twee dagen stress herstelde de plant echter niet meer. De T_2 veranderingen in gierst waren nog groter dan gedurende milde stress, vooral in de secundaire scheuten. Het stengelweefsel kromp, wat inhoudt dat de celgroottes veranderden. Het watergehalte van de secundaire scheuten veranderde daarentegen slechts weinig. De plant herstelde zodra de stress werd opgeheven. Vanuit het model kan de vermindering van de T_2 verklaard worden door een combinatie van krimpende cellen en een toenemende membraanpermeabiliteit. Deze laatste kan leiden tot een lagere weerstand voor watertransport in de weefsels en kan zo schade aan jonge, groeiende scheuten voorkomen door een herverdeling van water.

De combinatie van experimentele gegevens en computersimulaties, zoals gepresenteerd in dit proefschrift, is een goed hulpmiddel gebleken om NMR gegevens te interpreteren (Hoofdstuk 8). Deze aanpak is veelbelovend voor zowel de plantenwetenschappen als andere NMR-toepassingen.

CURRICULUM VITAE

Louise van der Weerd-Meulenkamp werd geboren op 21 augustus 1974 in Wageningen. Na het behalen van het VWO-diploma aan het Ichthus College in Veenendaal, begon zij in 1992 met de studie Moleculaire Wetenschappen aan Wageningen Universiteit. Tijdens de afstudeerfase voltooide ze een onderzoeksproject bij de vakgroep Moleculaire Fysica (thans Biofysica) aangaande droogtetolerantie in gierst. Een tweede onderzoeksproject werd verricht bij het Commissariat à l'Energie Atomique te Saclay, Frankrijk, betreffende een ESR studie van fotosysteem I. Na afronding van deze studie in augustus 1996, trad zij als Assistent In Opleiding (AIO) in dienst bij het Laboratorium voor Biofysica (Wageningen Universiteit), waar zij het onderzoek verrichtte dat leidde tot dit proefschrift. Sinds maart 2002 is zij als research fellow verbonden aan het Institute for Child Health te London, om MRI onderzoek te doen aan de invloed van Heat Shock Proteins op de ernst van een herseninfarct.

LIST OF PUBLICATIONS

- MacMillan F., Hanley J., van der Weerd L., Knupling M., Un S. & Rutherford A.W.** (1997) Orientation of the phyloquinone electron acceptor anion radical in photosystem I. *Biochemistry* 36, 9297-9303.
- Van der Weerd L., Ruttink T., Van Dusschoten D., Vergeldt F.J., De Jager P.A. & Van As H.** (1998) Plant growth studies using low field NMR. In: Spatially resolved magnetic resonance: methods, materials, medicine, biology, rheology, geology, ecology, hardware (eds Blümner P., Blümich B., Botto R. & Fukushima E.), 473-479. Wiley-VCH, New York.
- Van der Weerd L., Vergeldt F.J., De Jager P.A. & Van As H.** (2000) Evaluation of algorithms for analysis of NMR relaxation decay curves. *Magnetic Resonance Imaging* 18, 1151-1157.
- Van der Weerd L., Claessens M.M.A.E., Ruttink T., Vergeldt F.J., Schaafsma T.J. & Van As H.** (2001) Quantitative NMR microscopy of osmotic stress responses in maize and pearl millet. *Journal of Experimental Botany* 52, 2333-2343.
- Wolters-Arts M., van der Weerd L., van Aelst A.C., van der Weerd J., Van As H. & Mariani C.** (2002) Water conducting properties of lipids during pollen hydration. *Plant, Cell and Environment* 25, 513-519.
- Van der Weerd L., Melnikov S.M., Vergeldt F.J., Novikov E.G. & Van As H.** (2002) Modelling of self-diffusion and relaxation time NMR in multi-compartment systems with cylindrical geometry. *Journal of Magnetic Resonance* 156, 213-221.
- Van der Weerd L., Claessens M.M.A.E., Efdé C. & Van As H.** (2002) NMR imaging of membrane permeability changes in plants during osmotic stress. *Plant, Cell and Environment* in press.
- Van der Weerd L., Snaar J.E.M., Vergeldt F.J. & Van As H.** (2002) Simulation of relaxation, diffusion and exchange in multi-compartment systems as observed by NMR. Submitted.